E-740

A Search for Self-Interactions of Neutral Electroweak Gauge Bosons

By

Steven M. Glenn

August 1996

DISSERTATION

Submitted in partial satisfaction of the requirements for the degree of

DOCTOR OF PHILOSOPHY

in

Physics

in the

GRADUATE DIVISION

of the

UNIVERSITY OF CALIFORNIA

DAVIS

Approved:

FERMILAB
LIBRARY

.....

.....

.....

AAE 6665 gift

FERMILAB
LIBRARY

Abstract

A search for interactions between the Z and γ neutral electroweak bosons is presented. This was accomplished through the study of the reaction $p\bar{p} \rightarrow e^+e^-\gamma X$ at $\sqrt{s} = 1.8$ TeV using the DØ detector at Fermilab. In a data sample corresponding to an integrated luminosity of 89 pb^{-1}, 14 candidate events were identified, which is consistent with the Standard Model prediction of 13.9 ± 1.3 events, including an estimated background of 1.8 ± 0.6 events. Limits on $ZZ\gamma$ and $Z\gamma\gamma$ couplings are obtained from a maximum likelihood fit to the photon transverse momentum distribution. Assuming a form factor scale of 500 GeV, the 95% CL limits on the CP-even couplings are $|h_{30}^Z| < 4.1$, $|h_{40}^Z| < 0.90$, $|h_{30}^\gamma| < 4.5$, and $|h_{40}^\gamma| < 1.00$ when the CP-odd couplings are constrained to their Standard Model values.

Acknowledgements

This work represents the collective work of hundreds of people, and I am very much indebted to the many DØ collaborators who helped build and operate the detector successfully. Anybody who has ever visited the DØ control room or seen the detector can appreciate the complexity of this endeavor and how much work is required to make it run smoothly. Those in the Fermilab Accelerator Division also deserve credit for the impressive operation of the Tevatron during the 1993-1995 run.

It has been a privilege to work with many knowledgeable colleagues, and I regret that there is insufficient space here to mention them all explicitly. My sincerest apologies to any of you whom I have neglected. I was fortunate to have shared the U.C. Davis cubicle with Paul Bloom for the past couple of years. He helped with many parts of the analysis and proofread this document. This work would not have been possible without Jamal Tarazi, as he was responsible for keeping the data samples organized and intact. Joey Thompson provided many useful discussions

and performed the luminosity calculations. Members of the electron ID group, led by Meenakshi Narain, developed many of the techniques used in this analysis. The Editorial Board - Pushpa Bhat, John Hobbs, Mark Adams, and Brajesh Choudhary - also gave many useful suggestions and took the time to review this work. Members of the Electroweak and Diboson analysis groups also provided valuable input. In no particular order, they are: Greg Landsberg (who performed the 1A analysis), Brajesh Choudhary, Marcel Demarteau, Ulrich Heinz, Darien Wood, Mike Kelly, Tom Fahland, Tom Diehl, and Taka Yasuda. This analysis could not have been completed without help from Ulrich Baur, who provided both advice and the event generator. Jim Ohnemus kindly furnished the NLO calculations.

Sudhindra Mani deserves special thanks for all the guidance and support he has provided over the last few years as my advisor. I have also been fortunate to have worked with professors Richard Lander and Dave Pellett during my graduate career.

I owe a great debt of gratitude to my parents, who have always given me encouragement and allowed me to pursue my curiosities. Last, but definitely not least, is Victoria and her family. Victoria deserves an indescribable amount of thanks for sacrificing so much, putting up with me, and generally enriching my life.

To Victoria

Contents

Abstract ii

Acknowledgements iii

List of Tables ix

List of Figures xi

1 Introduction 1
- 1.1 The Standard Model of Elementary Particle Physics 1
- 1.2 The Standard Model of Electroweak Interactions 2
- 1.3 Beyond the Standard Model 11
- 1.4 New Physics Searches 11
- 1.5 Physics at the Tevatron 14

2 $Z\gamma$ Interactions 18
- 2.1 Probing $Z\gamma$ Interactions at the Tevatron 19
- 2.2 Formalism 22
- 2.3 Self Consistency 24
- 2.4 Manifestations of $Z\gamma$ Interactions 30
- 2.5 NLO Corrections 40
- 2.6 Possible Sources of $Z\gamma$ Interactions 42
- 2.7 Previous Experimental Limits 46

3 Experimental Apparatus 50
- 3.1 The FNAL Collider Complex 50
- 3.2 The DØ Detector 54
  - 3.2.1 Central Detector 56
  - 3.2.2 Calorimetry 58
  - 3.2.3 Muon Tracking 62

3.2.4 Trigger and Data Acquisition 62
3.3 Data Reconstruction 67

4 Event Reconstruction and Particle Identification 69
4.1 Tracking 70
4.2 Vertexing 71
4.3 Jets 73
4.4 Electrons and Photons 74
4.5 Shower Isolation 76
4.6 Shower Shape 77
4.7 Track Matching 79
4.8 Extensions to Standard Techniques 82
4.8.1 Track-Cluster Matching and Vertex Corrections 83
4.8.2 Hit Counting Techniques 87
4.9 Particle ID Summary 88

5 Event Selection 90

6 Detection Efficiencies 96
6.1 Electrons 97
6.2 Photons 104

7 Detector Simulation 109
7.1 Fiducial Acceptance 110
7.2 Kinematic Resolution and Acceptance 111
7.3 Selection Efficiency 112
7.4 Systematic Uncertainties 114

8 Backgrounds 118
8.1 Misidentified Jets 119
8.2 Other Sources of $ee\gamma X$ 124

9 Results 130
9.1 Comparisons with Standard Model Predictions 130
9.2 Coupling Limits from the Counting Experiment 140
9.3 Coupling Limits from the Photon Spectrum 148

10 Conclusions 158
10.1 Summary 158
10.2 Comparison with Previous Results 160
10.3 Future Prospects 162
10.4 Final Remarks 164

A Candidate Summaries **165**

B Measurement of $P_{j\to\gamma}$ and $P_{j\to e}$ **172**
B.1 Introduction 172
B.2 Data Sample and Event Selection 174
B.3 Trigger Bias 175
B.4 Direct Photon Subtraction 177
B.5 Fake Probabilities 182
B.6 Background Prediction for $Z \to ee$ 185

C Combined Likelihood Functions **190**

Bibliography **193**

List of Tables

2.1 Summary of $Z^* \to Z\gamma$ transitions allowed by spin conservation. . . . 24
2.2 Kinematic criteria used to define the phase space of the experimentally "visible" cross section. 31
4.1 Summary of electron/photon selection criteria. Quantities in parenthesis are values used for objects in the forward region. 89
5.1 Selection process for $e_t e_l \gamma$ events. 93
6.1 Summary of background subtraction methods and signal windows used in electron identification efficiency measurements. 99
6.2 Number of electrons in Z mass window for various offline cuts and background subtraction methods. Only central candidates reconstructed with DØRECO versions 12.15 and higher are shown. 100
6.3 Measured efficiencies for electron identification. See text for definitions. 101
6.4 Parameters for low-p_T photon selection efficiency. 106
7.1 Energy resolution parameters for electrons and photons. 111
7.2 Sources of systematic uncertainty for the predicted $ee\gamma$ signal yield. . 117
8.1 Jet misidentification probabilities for electrons and photons. Errors quoted are statistical (fit) errors only. A systematic uncertainty of 30% is assigned to each fake probability. Uncertainties given in this table are statistical only. 121
8.2 Backgrounds to $e_t e_l \gamma$ due to jet misidentification. Errors are purely statistical. 123
9.1 Summary of the $ee\gamma$ counting experiment. 131
9.2 Kinematic criteria used to select $Z\gamma$ production events. 133
9.3 Values of δ for confidence regions with one or two parameter fits. . . . 152
10.1 Summary of coupling limits obtained from a fits to the photon p_T spectrum assuming $n_3 = 3$, $n_3 = 4$, and $\Lambda = 500$ GeV. 159
A.1 Summary of candidate $ee\gamma$ event kinematics. 166
B.1 Summary of E_T thresholds used in measuring fake rates. Units are GeV. 177

B.2 Jet misidentification probabilities for electrons and photons. Errors quoted are statistical (fit) errors only. A systematic uncertainty of 30% is assigned to each fake probability. Uncertainties given in this table are statistical only. 183
C.1 Summary of uncertainties for combined likelihood construction. . . . 192

List of Figures

1.1 A plot of the Higgs potential both as a function of the complex scalars ϕ^+ and ϕ^0 (left) and as a function of ϕ^0 only. 8

1.2 Corrections to the $Z \to b\bar{b}$ vertex involving the top quark. 12

1.3 (a) Parton distributions from the MRSD'_ set evaluated at $\mu = M_Z$. (b) Sensitivity of the up and down quark distributions to the scale μ. Typical x values for gauge boson production are indicated by x_{WZ}. . 15

1.4 Cross sections for various processes at the Tevatron as predicted by the ISAJET Monte Carlo. 17

2.1 $ZZ\gamma$ and $Z\gamma\gamma$ vertices 19

2.2 Diagrams for $q\bar{q} \to \ell^+\ell^-\gamma$ via $ZZ\gamma$ and $Z\gamma\gamma$ couplings. 20

2.3 Diagrams for $q\bar{q} \to \ell^+l^-\gamma$ via Standard Model processes. (a) and (b): Associated $Z\gamma$ production. (c) and (d): Radiative Decays. 21

2.4 The $ZZ\gamma$ vertex function with notation as used in the formalism. . . 22

2.5 Form factor behavior as a function of the parton subprocess center-of-mass energy for different values of the form factor scale Λ. 27

2.6 Exclusion regions for the couplings h_{30}^Z and h_{40}^Z based on unitarity for different values of the form factor scale Λ. 29

2.7 Invariant mass and transverse momentum distributions of the final state products in Standard Model $p\bar{p} \to \ell^+\ell^-\gamma$ at $E_{\rm CM} = 1.8$ TeV. . . 33

2.8 Angular distributions of the final state products in Standard Model $p\bar{p} \to \ell^+\ell^-\gamma$ at $E_{\rm CM} = 1.8$ TeV. 34

2.9 Predicted cross section for $p\bar{p} \to \ell^+\ell^-\gamma$ at $E_{\rm CM} = 1.8$ TeV as a function of h_{30}^Z and h_{40}^Z. 37

2.10 Invariant mass and transverse momentum distributions of the final state products in $p\bar{p} \to \ell^+\ell^-\gamma$ at $E_{\rm CM} = 1.8$ TeV case of $h_{30}^Z = 2$. . . . 38

2.11 Angular distributions of the final state products in $p\bar{p} \to \ell^+\ell^-\gamma$ at $E_{\rm CM} = 1.8$ TeV for the case of $h_{30}^Z = 2$. 39

2.12 Correction to $q\bar{q} \to \ell^+\ell^-\gamma$ due to QCD initial state radiation. 41

2.13 Ratio of NLO to LO predicted cross section for $p\bar{p} \to \ell^+\ell^-\gamma$ at $E_{\rm CM}$ = 1.8 TeV as a function of the photon transverse momentum. 42
2.14 Composite Z Boson Scenario. 43
2.15 Contribution to neutral gauge boson couplings due to loop effects. . . 44
2.16 Contribution to $l^+l^+\gamma$ production due to exited lepton decay. 45
2.17 Contribution of $Z\gamma\gamma$ vertex to the muon anomalous magnetic moment $(g-2)_\mu$. 47
2.18 Limits on the CP-even couplings h_{30}^Z and h_{40}^Z from previous collider experiments at the Tevatron and LEP. 48
3.1 Schematic of the FNAL facility (not to scale). 52
3.2 Isometric cutaway view of the DØ detector. 55
3.3 End view of three CDC modules. Sense wires are indicated by small dots, guard (field shape) wires by large dots, and delay lines by open circles. 56
3.4 Exploded isometric view of one half of the FDC tracking system. . . . 58
3.5 Side view of one quadrant of the calorimeter and central detector. The lines of constant pseudorapidity intervals with respect to $z = 0$. . 60
3.6 Longitudinal tower segmentation of the DØ calorimeter as a function of pseudorapidity. 61
3.7 Schematic of data aquisition at DØ. 67
4.1 Vertex determination by histogram method. Top: projections of tracks to the beamline. (View is integrated over all azimuthal angles ϕ.) Bottom: Resulting distribution of z-intercepts from which vertices are determined. 72
4.2 Isolation and χ^2 distributions for $Z \to ee$ candidates and electrons identified in multijet-triggered data. 77
4.3 Differences in cluster and projected track positions for $Z \to ee$ candidates. Only candidates with $s_{\rm trk} < 30$ are shown. 80
4.4 Definition of the track match significance in terms of the cluster centroid in EM3 and the projection of a track to this radius. 81
4.5 Track match significance distributions for $Z \to ee$ and Multijet-dominated samples for central (CC/CDC) and forward (EC/FDC) angles. 82
4.6 Vertex determination by cluster-track projection method. 84
4.7 (a) Frequency at which the electron vertex is found more than 10 cm from the standard (DØRECO) vertex. Also shown is the rate at which the electron track z intercepts differ by more than 10 cm. (b) Invariant mass distribution for $Z \to ee$ candidate events using the two vertexing schemes. 86

4.8 Number of drift chamber hits for both $Z \to ee$ candidates (solid) for both the central and forward regions. The dashed line indicates the number of random hits in emulated photon roads. 89
5.1 Side and end views of one $p\bar{p} \to ee\gamma$ candidate. 94
5.2 Lego plot for one $p\bar{p} \to ee\gamma$ candidate. 95
6.1 Fractions of sample reconstructed with various DØRECO versions for data collected with the `em2_eis2_hi` L2 filter. 98
6.2 Efficiency of L2 $E_T > 20$ requirement for electron-like objects. Error bars indicate sensitivity to EM energy fraction requirement. 103
6.3 Efficiency of the isolation and shower shape requirements as a function of photon transverse momentum. The error bars are purely statistical. 106
6.4 Inefficiency of the photon track/hit veto requirements as a function of angle as measured from $Z \to ee$ events. The error bars are purely statistical. 108
7.1 Comparison of detector response to $p\bar{p} \to e^+e^-X$ events subjected to kinematic and fiducial requirements on the electrons. Also shown are the E_T and η distributions of electrons directly from the ISAJET generator. 112
7.2 Comparison of predicted event yields for pdf choices. The individual error bars indicate sensitivity to the renormalization scale, and the large error bar on the MRSD'_ case indicates the systematic uncertainty assigned to the pdf choice. 115
8.1 Diagram for background due to $Z + j$ production. 120
8.2 Background distributions in terms of photon transverse momentum, three body ($ee\gamma$) invariant mass, and dielectron invariant mass. The solid line indicates the best fit and the dotted lines indicate the 1σ combined systematic and statistical errors on the background. 124
8.3 (a) Transverse momentum distribution of both prompt and decay electrons in $p\bar{p} \to Z \to \ell^+\ell^l$. (b) The same distributions for $Z\gamma$ production with the restriction that $p_T^\gamma > 50$ Gev/c. 126
8.4 Background distributions in terms of photon transverse momentum for $WZ \to eee\nu$ and jets. 129
9.1 Distribution of photon transverse momenta for $ee\gamma$ candidates. 135
9.2 Dielectron invariant mass distribution for $ee\gamma$ candidates. 136
9.3 Dielectron-photon invariant mass distribution for $ee\gamma$ candidates. . . 137
9.4 Correlations of p_T^γ, m_{ee}, and $m_{ee\gamma}$ for the $ee\gamma$ candidates. The dotted lines indicate regions where $m_{ee} \approx M_Z$, which is characteristic of $Z\gamma$ production. 138
9.5 Distribution of photon transverse momenta for $Z\gamma \to ee\gamma$ candidates. 139

9.6 Comparison of Poisson and Gaussian probability densities in which the average number of expected events is 14.0. Also shown are the cumulative probabilities for observing greater than N events. candidates. 140
9.7 Probability of observing 14 or fewer events as a function of h_{30}^Z and h_{40}^Z for $\Lambda = 500$ GeV. 144
9.8 Correlated limits on h_{30}^Z and h_{40}^Z for $\Lambda = 500$ GeV from the event counting technique. 146
9.9 Correlated limits on h_{30}^γ and h_{40}^γ for $\Lambda = 500$ GeV from the event counting technique. 147
9.10 Plot of $\ln(L)$ as computed from equation 9.7 over the h_{30}^Z-h_{40}^Z plane for $\Lambda = 500$ GeV. 151
9.11 Correlated limits on h_{30}^Z and h_{40}^Z for $\Lambda = 500$ GeV from the fit to the photon transverse momentum spectrum. 153
9.12 Correlated limits on h_{30}^γ and h_{40}^γ for $\Lambda = 500$ GeV from the fit to the photon transverse momentum spectrum. 154
9.13 Likelihood functions in which only one variable is allowed to deviate from its SM value for $\Lambda = 500$ GeV. The resulting uncorrelated 95% CL limits on h_{30}^Z, h_{40}^Z, h_{30}^γ, and h_{40}^γ are indicated by the dotted lines. . 156
9.14 Correlated limits on h_{30}^Z and h_{40}^Z for $\Lambda = 500$ GeV from the fit to the photon transverse momentum spectrum using the five $Z\gamma$ production candidate events only. 157
10.1 Correlated limits on the coupling pairs (h_{30}^Z, h_{40}^Z) and $(h_{30}^\gamma, h_{40}^\gamma)$ for $\Lambda = 500$ GeV from the fit to the photon transverse momentum distribution. The confidence region corresponds to $\delta = 1.92$ (85% CL). . 161
10.2 (a) Photon transverse momentum distribution for ensemble of $55 + 5 = 60$ events expected for an integrated luminosity of 1 fb^{-1}. (b) Correlated limits on the coupling pair (h_{30}^Z, h_{40}^Z) obtained from this sample. 163
B.1 Typical trigger efficiencies for electromagnetic and hadronic objects as a function of transverse energy. The efficiency at the trigger threshold E_T^0 is not 50% due to offline energy corrections. 176
B.2 Transverse energy distribution of jets in the multijet sample for the central (CC) region and forward (EC) regions for the various filters used in this study. 178
B.3 Transverse energy distribution of electrons and photons in the multijet sample for the central (CC) region and forward (EC) regions for the various filters used in this study. 179
B.4 Jet, electron, and photon CC candidates identified in the multijet sample. 182

B.5 Jet misidentification probabilities as a function of transverse energy for objects in the central and forward regions. 184
B.6 Left: transverse energy distribution of jets in multijet candidate events. Right: distribution of the number of jets per event. See text for selection criteria. 186
B.7 Top: Invariant mass of dielectron candidates and predicted multijet background. Bottom: Invariant mass spectrum of dielectron candidates and predicted multijet background for the sidebands on either side of the $Z \rightarrow ee$ peak. Also indicated are the number of expected events based on the PYTHIA Monte Carlo generator. Error bars are statistical only. 189

FERMILAB
LIBRARY

Chapter 1

Introduction

1.1 The Standard Model of Elementary Particle Physics

As its name implies, Elementary Particle Physics is the study of the building blocks of nature. Specifically, physicists aim to answer the following question: "What constitutes matter and what holds it together?" In the 100 years since J.J. Thompson first identified the electron, much experimental and theoretical progress has been made toward this goal. In fact, a theory of elementary particles has evolved which describes experimental data so well that it is now known as the "Standard Model" (SM). The work discussed here is a search for deficiencies in the Standard

Model when confronted with experimental data; evidence of such would be an indication of new physical phenomena.

The SM posits that all matter is composed of pointlike particles called quarks and leptons which are subject to three fundamental forces: electromagnetism, the "weak" force, and the "strong" force. Although gravity has not been incorporated into the SM, its effects are negligible at presently available energies. According to the SM, the electromagnetic, weak, and strong forces are mediated by the exchange of spin-1 bosons associated with the respective forces. The photon transmits the electromagnetic force, the $W^{\pm}$ and Z bosons transmit the weak force, and gluons transmit the strong force.

One of the main features of the SM is that the electromagnetic and weak forces are unified; they are manifestations of the same force. This so-called electroweak (EW) interaction is the focus of this work. The next section gives a brief description of the electroweak sector of the Standard Model in order to provide context for further discussion.

1.2 The Standard Model of Electroweak Interactions

The electroweak portion of the Standard Model is based on the assumption that quarks and leptons carry internal quantum numbers which transform under

the $SU(2)_L \times SU(1)_Y$ symmetry group. The L subscript denotes the fact that only left-handed particles transform under the SU(2) internal "weak isospin" symmetry group, while the Y subscript indicates that both left-handed and right handed particles transform under the U(1) "weak hypercharge" group. To make this more concrete, consider the spinors e and ν representing the electron and electron neutrino, respectively. The left handed parts of the spinors form a weak isospin doublet E_L transforming as a $j = 1/2$ representation of SU(2) [1]:

$$E_L = \begin{pmatrix} \nu_L \\ e_L \end{pmatrix}$$

where $e_L = \frac{1}{2}(1-\gamma^5)e$ and $\nu_L = \frac{1}{2}(1-\gamma^5)\nu$. All present experimental evidence precludes the existence of right-handed neutrinos, so the right handed electron must exist as a weak isospin singlet transforming as a $j = 0$ (trivial) representation of SU(2):

$$E_R = e_R$$

where $e_R = \frac{1}{2}(1+\gamma^5)e$. Thus, the SU(2) weak isospin transformation rules for the left and right handed states are given by

$$E'_L = \exp(-ig\vec{\alpha}\cdot\vec{\tau}/2)E_L$$

and

$$E'_R = E_R$$

where g is a constant, $\vec{\alpha}$ is a vector specifying the transformation, and $\vec{\tau}$ is a vector of SU(2) generator matrices. In the $j = 1/2$ representation of SU(2), these generators are the familiar Pauli spin matrices. The U(1) gauge transformations of the left and right handed states are given by

$$E'_L = e^{-ig'\beta/2} E_L$$

and

$$E'_R = e^{-ig'\beta} E_R$$

where g' is a constant and β specifies the transformation. The important thing to notice here is that the U(1) transformations simply result in an overall phase change, while the SU(2) transformations mix the components of the left-handed doublet. This latter characteristic is one feature of such non-Abelian transformations. As will be discussed later, this has important consequences for the gauge boson sector as well.

Another important ingredient of the electroweak theory is that of local gauge (phase) invariance. That is, the theory is required to yield the same results when the fields are changed according to the above prescriptions at every point in space-time independently. In this case, $\vec{\alpha}$ and β are functions of the space-time coordinate x. This principle was first developed for the case of SU(2) by Yang and Mills [2] in the context of strong interactions. This theory was ultimately unsuccessful in describing strong interactions and lay dormant for a few years until Glashow [3] added U(1)

symmetry and applied it to weak interactions. In Glashow's theory, all fermions were considered massless particles which carry weak isospin (I_w) and hypercharge (Y) quantum numbers. Local gauge invariance then required the existence of four massless "gauge fields" which interacted with the fermion fields. For example, the "free" langrangian density for the left-handed massless electron isodoublet is

$$\mathcal{L}_{\text{free}} = \bar{E}_L \gamma^\mu \partial_\mu E_L \tag{1.1}$$

The requirement that the action be invariant under local gauge transformations is satisfied by the appropriate replacement of ∂_μ by the "covariant derivative" D_μ whose form is determined by the gauge symmetry group. For the case of simultaneous $\mathrm{SU}(2)_L$ and $\mathrm{U}(1)_Y$ gauge symmetries, the existence of a vector field $\vec{W}(x)$ and a scalar field $B(x)$ are needed in order to appropriately construct D_μ. The required (infinitesimal) gauge transformation properties of these fields are [12]:

$$\vec{W}'_\mu = \begin{cases} \vec{W}_\mu, & \mathrm{U}(1)_Y \\ \vec{W}_\mu + \partial_\mu \vec{\alpha} + g\vec{\alpha} \times \vec{W}_\mu, & \mathrm{SU}(2)_L \end{cases} \tag{1.2}$$

and

$$B'_\mu = \begin{cases} B_\mu + \partial_\mu B_\mu, & \mathrm{U}(1)_Y \\ B_\mu, & \mathrm{SU}(2)_L \end{cases} \tag{1.3}$$

where the cross product in (1.2) is evaluated in I_w space. The required form of the covariant derivative is

$$D_\mu = \partial_\mu + ig\vec{W}_\mu \cdot \vec{\tau} + \frac{1}{2} i g' B_\mu Y \tag{1.4}$$

where Y is the weak hypercharge assigned to the isodoublet on which D_μ operates. Substitution of equation 1.4 into the lagrangian of equation 1.1 reveals that the requirement of local gauge invariance has generated interaction terms between the fermion fields and the $\vec{W}$ and B fields.

Unfortunately, this procedure does not work for massive fermions, nor can it accommodate massive gauge fields. The theory also turns out to be unrenormalizable. Nevertheless, the physical gauge boson fields can be formally identified as linear combinations of the $\vec{W}$ and B fields which represent states of definite electromagnetic charge Q, where $Q = I^3 + Y/2$. These are given by

$$W_\mu^\pm = (W_\mu^1 \mp iW_\mu^2)/\sqrt{2} \tag{1.5}$$

$$Z_\mu = W_\mu^3 \cos\theta - B_\mu \sin\theta \tag{1.6}$$

$$A_\mu = W_\mu^3 \sin\theta + B_\mu \cos\theta \tag{1.7}$$

where θ is a parameter known as the Weinberg angle and A_μ represents the electromagnetic field.

Further progress toward a satisfactory theory was made by Weinberg [4] and Salam [5], who built upon earlier work by Higgs [6] and formulated Glashow's theory in terms of spontaneously broken gauge symmetry. In this scheme, the photon is massless and the W/Z bosons are massive. A few years later, 't Hooft [7] proved that the Glashow-Weinberg-Salam (GWS) electroweak theory was renormalizable. The GWS theory described contemporary experimental data quite well, and direct

W and Z boson production was observed at CERN in 1983 [8, 9, 10, 11].

The GWS electroweak theory begins with the assumption that two or more scalar fields exist which carry I_w and Y quantum numbers. Conventionally, it is assumed that only two such fields exist as an SU(2) weak isospin doublet Φ [12]:

$$\Phi = \begin{pmatrix} \phi^+ \\ \phi^0 \end{pmatrix}$$

where ϕ^+ and ϕ^0 are complex scalar fields. The ϕ^+ scalar field is assigned quantum numbers of $(I^3, Y, Q) = (1/2, 1, 1)$, and the ϕ^0 field is assigned $(I^3, Y, Q) = (-1/2, 1, 0)$. A crucial piece of the Higgs mechanism is the introduction of a potential which results in a non-zero vacuum expectation value for Φ. The most general renormalizable form of the potential V is

$$V(\Phi) = \mu^2 \Phi^\dagger \Phi + \lambda (\Phi^\dagger \Phi)^2.$$

With the addition of the kinetic term, the Lagrangian density describing the field is

$$\mathcal{L}_\Phi = (\partial_\mu \Phi)^\dagger (\partial^\mu \Phi) - \mu^2 \Phi^\dagger \Phi - \lambda (\Phi^\dagger \Phi)^2 \tag{1.8}$$

As is shown in figure 1.1, The minimum of the potential (physical vacuum) does not coincide with $|\Phi| = 0$ for $\mu^2 < 0$, but occurs instead at $|\Phi| = \sqrt{-\mu^2/2\lambda}$. Since perturbation theory is only valid for fluctuations about the physical vacuum, it is necessary to reformulate the theory in terms of excitations about the points at which $|\Phi| = \sqrt{-\mu^2/2\lambda}$. In the *unitary* (or *physical*) gauge, the scalar doublet is

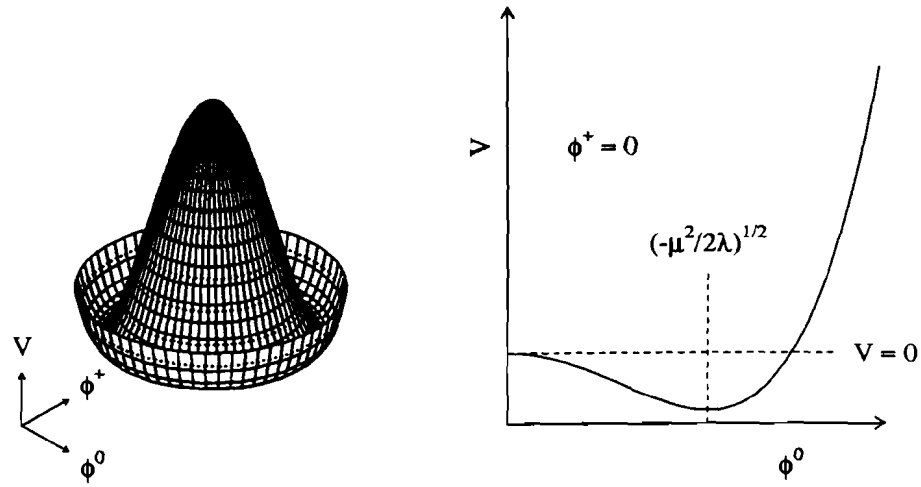

Figure 1.1: A plot of the Higgs potential both as a function of the complex scalars ϕ^+ and ϕ^0 (left) and as a function of ϕ^0 only.

redefined as

$$\Phi = \frac{1}{\sqrt{2}} \begin{pmatrix} 0 \\ v + H(x) \end{pmatrix} \tag{1.9}$$

where v is the vacuum expectation value of Φ and H represents excitations above the minimum of the potential. Effectively, a particular direction has been chosen in (I, Y) space and the manifest gauge symmetry of the Lagrangian has been destroyed in exchange for a formulation which represents physics at energies low enough so that the W/Z bosons cannot be considered massless.

Substitution of 1.9 into 1.8 and addition of the terms required to satisfy local gauge invariance yields [1, 12]

$$\mathcal{L}_\Phi = \frac{1}{2}(\partial_\mu H)^*(\partial^\mu H) + \mu^2 H^2 \tag{1.10}$$

$$-\frac{1}{4}A_{\mu\nu}A^{\mu\nu} \tag{1.11}$$

$$-\frac{1}{4}(W^-_{\mu\nu}W^{+\mu\nu} - \frac{g^2v^2}{2}W^-_\mu W^{+\mu}) \tag{1.12}$$

$$-\frac{1}{4}(Z_{\mu\nu}Z^{\mu\nu} - \frac{g^2v^2}{4\cos^2\theta}Z_\mu Z^\mu) \tag{1.13}$$

$$+ig\sin\theta(W^-_\mu W^+_\nu A^{\mu\nu} + W^+_\mu W^{-\mu\nu}A_\nu - W^{+\mu\nu}W^-_\mu A_\nu) \tag{1.14}$$

$$+ig\cos\theta(W^-_\mu W^+_\nu Z^{\mu\nu} + W^+_\mu W^{-\mu\nu}Z_\nu - W^{+\mu\nu}W^-_\mu Z_\nu) \tag{1.15}$$

$$-\frac{1}{2}g^2(W^+_\mu W^{-\mu}W^+_\nu W^{-\nu} - W^+_\mu W^{+\mu}W^-_\nu W^{-\nu}) \tag{1.16}$$

$$-g^2\sin^2\theta(W^+_\mu W^{-\mu}A_\nu A^\nu - W^+_\mu A^\mu W^-_\nu A^\nu) \tag{1.17}$$

$$-g^2\cos^2\theta(W^+_\mu W^{-\mu}Z_\nu Z^\nu - W^+_\mu Z^\mu W^-_\nu Z^\nu) \tag{1.18}$$

$$-g^2\sin\theta\cos\theta(W^+_\mu W^{-\mu}A_\nu Z^\nu - W^+_\mu W^-_\nu A^\mu Z^\nu) \tag{1.19}$$

$$+\frac{g^2}{4}(\frac{1}{\sqrt{2}}vH + \frac{1}{2}H^2)[2W^-_\mu W^{+\mu} + \frac{1}{\cos^2\theta}Z_\mu Z^\mu] \tag{1.20}$$

$$+\frac{\mu^2}{v}H^3 + \frac{4\mu^2}{v^2}H^4 \tag{1.21}$$

where θ is the Weinberg angle, g is the electroweak coupling constant, and $V_{\mu\nu} \equiv \partial_\mu V_\nu - \partial_\nu V_\mu$; $(V = W^\pm, Z, A)$. The first line represents the kinematic and mass terms[1] of the scalar Higgs field, and lines 1.12 through 1.14 are the kinematic and

[1]The mass term is the piece of the Lagrangian which is quadratic in the field variable. This is easily verified by applying the Euler-Lagrange equations of motion to the Lagrangian.

mass terms of the electroweak gauge fields. It should be noted that there is no mass term associated with photon field A, while the W and Z bosons have masses of $gv/\sqrt{2}$ and $gv/(2\cos\theta)$, respectively. Lines 1.15 and 1.16 describe trilinear $W^+W^-\gamma$ and W^+W^-Z couplings which are a consequence of the non-Abelian symmetry of the theory. Similarly, lines 1.17 - 1.19 contain non-abelian $WW\gamma\gamma$, $WWZZ$, and $WWZ\gamma$ quartic couplings, and line 1.18 contains trilinear couplings between the W/Z bosons and the Higgs scalar. Finally, line 1.19 contains cubic and quartic self-interactions of the Higgs field.

At the focus of this study are the interactions between the gauge bosons, the most accessible of which are the trilinear couplings.[2] The lagrangian $\mathcal{L}_3$ describing this portion of the EW sector is given by

$$\begin{aligned}\mathcal{L}_3 &= +ig\sin\theta(W_\mu^- W_\nu^+ A^{\mu\nu} + W_\mu^+ W^{-\mu\nu} A_\nu - W^{+\mu\nu} W_\mu^- A_\nu) \\ &\quad +ig\cos\theta(W_\mu^- W_\nu^+ Z^{\mu\nu} + W_\mu^+ W^{-\mu\nu} Z_\nu - W^{+\mu\nu} W_\mu^- Z_\nu). \qquad (1.22)\end{aligned}$$

It should be noted that (1.22) contains no interactions between the Z and A fields. On the other hand, the $W^\pm$ bosons carry electric charge and therefore couple to the photon. The photon and Z fields are *defined* to be orthogonal combinations of the interacting W and B fields in order to yield states which correspond to the observed vector boson masses, so they do not interact *by construction* in the GWS theory.

[2]As can be seen from (1.17-1.19), the quartic interactions are suppressed by an extra factor of g. Additionally, measurement of such couplings generally involves triple gauge boson production, which is less kinematically favorable than diboson production and is beyond the range of present experimental sensitivity.

1.3 Beyond the Standard Model

Despite the success of the electroweak SM, it does have possible shortcomings. There are a large number of *ad hoc* parameters in the SM which are not calculable from first principles, and there are reasons to believe the SM will ultimately fail as experiments probe ever higher energies[12]. To date, there is no conclusive experimental evidence for the existence of Higgs boson(s). Some other unanswered questions are listed below. The aim of this study is to address these questions.

1. Is the Higgs mechanism responsible for electroweak symmetry breaking? If so, how many Higgs scalars exist?

2. How many gauge bosons exist?

3. Are quarks, leptons, and gauge bosons composed of other, more fundamental, particles?

1.4 New Physics Searches

One way to experimentally test the SM is to search for direct production of new particles. At a $p\bar{p}$ collider, one might search for Higgs bosons through the reaction $p\bar{p} \rightarrow Z^* \rightarrow ZH$. However, the production rate of massive particles is limited by the energy available in the collisions[3], so observation of such relatively

[3]The production cross section is also affected by the coupling between the heavy particle and the initial/final state particles. Nevertheless, the kinematic argument given here remains valid.

rare processes is difficult unless large amounts of data are collected or higher energies are reached. For example, top quark production was only recently observed at the Tevatron [13, 14] after a rather large amount of data had been collected. It was not observed at the CERN $S\bar{p}pS$ collider due to the lower energy and amount of available data.

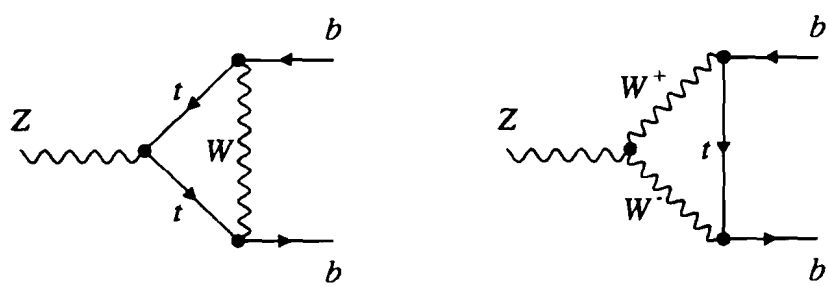

Figure 1.2: Corrections to the $Z \to b\bar{b}$ vertex involving the top quark.

Another way to search for undiscovered physical phenomena is to look for *indirect* effects on observables at lower energies. This approach provides a possible glimpse at new physics before high enough energies are reached to allow for *direct* particle production to be observed. As an example, consider the diagrams in figure 1.2 which represent corrections to the $Z \to b\bar{b}$ vertex. These and other corrections are sensitive to the mass of the top quark and are manifested in several

experimental observables in $e^+e^- \rightarrow Z$ studies. If these quantities are measured precisely, the mass of the top quark can be predicted, despite the fact that no real top quarks are created. This approach was followed by groups at the LEP and SLC e^+e^- experiments. Using additional data from $p\bar{p}$ and νN experiments, the predicted mass of the top quark was found to be [15]

$$m_t = 179 \pm 9 \,^{+17}_{-19} \text{ GeV}$$

where the first uncertainty is the combined systematic and statistical error for an assumed Higgs mass of 300 GeV, and the second uncertainty reflects the variation of m_t for Higgs masses between 60 and 1000 GeV. When the top quark was directly observed, its measured mass was [13, 14]

$$m_t = 199 \,^{+19}_{-21} \pm 22 \text{ GeV}$$

and

$$m_t = 176 \pm 8 \pm 10 \text{ GeV}$$

by the DØ and CDF experiments, respectively. Thus, given a model and some reasonable assumptions, the mass of the top quark was inferred before direct production was observed. This indirect method of searching for new phenomena is the one employed here. Although it does not ultimately replace the direct approach, it can provide possible guidance to future experiments.

1.5 Physics at the Tevatron

The apparatus used in this search for $Z\gamma$ interactions is the Tevatron, which is a $p\bar{p}$ collider operating at $\sqrt{s} = 1.8$ TeV. The purpose of this section is to give an overview of $p\bar{p}$ physics in order to provide background for later discussion.

Any discussion of hadron collider physics must address the fact that hadrons are not fundamental particles; the outcome of hadron collisions is the result of collisions between hadronic constituents which are generically referred to as partons. This means that knowledge of the parton densities inside the colliding hadrons is necessary if one wants to calculate a cross section. The authors of references [16] and [17] have inferred these densities from recent experimental data. Figures 1.3a and 1.3b show the results of this analysis. In figure 1.3a, the parton density functions (pdf's) are plotted as a function of the proton momentum fraction x for the up, down, sea, and gluon constituents. Typically, electroweak gauge boson production at the Tevatron is sensitive to pdf's in the region of $x \approx 0.2$, which is indicated by "x_{wx}" in figure 1.3b. The pdf's shown in figure 1.3a have been evolved to a renormalization and factorization scale of $\mu = M_Z$, which is an energy characteristic of EW boson production. If cross sections could be calculated to all orders in perturbation theory, any scale dependence would disappear. Unfortunately, this is not feasible, so any calculation is subject to uncertainties arising from the choice of scale. Generally, this "theoretical uncertainty" is evaluated by varying the scale within a reasonable

range. Figure 1.3b shows the variation of the up and down quark distributions as the scale is changed by factors of two. These "valence" quark pdf's decrease as μ increases. More gluon and sea quarks are resolved at higher scales, so the valence quark distributions must decrease to satisfy momentum sum rules.

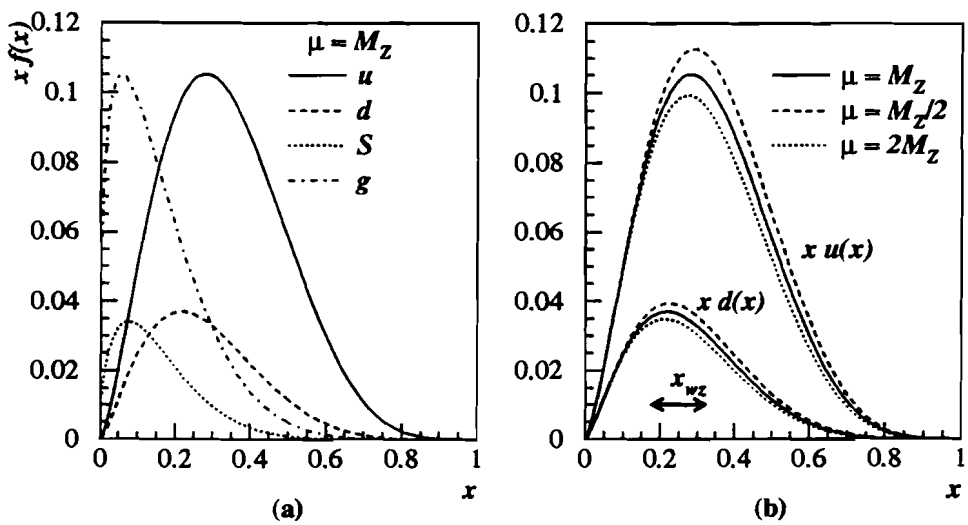

Figure 1.3: (a) Parton distributions from the MRSD'_ set evaluated at $\mu = M_Z$. (b) Sensitivity of the up and down quark distributions to the scale μ. Typical x values for gauge boson production are indicated by x_{WZ}.

Once the parton densities have been determined, it is possible to calculate cross sections for hadronic collisions. Figure 1.4 shows the predictions of the ISAJET [18] Monte Carlo calculation for various processes at the Tevatron as a function transverse momentum. At all transverse momenta, the overwhelmingly dominant

process is multijet production. (The "soft" diffractive $p\bar{p}$ processes have been neglected here since they mainly yield in low-p_T objects at forward angles.) This implies that the experiment would record multijet events almost exclusively if it were triggered by any object with $p_T > 10$ GeV, which would preclude the study of other physical processes with any statistical precision. The solution is to use particle identification and topological criteria in the trigger to select which events get recorded. For example, if the trigger required an isolated electromagnetic calorimeter cluster, much of the data recorded would be due to direct photon and π^0 production. Also indicated on figure 1.4 are the EW gauge boson production cross sections. Clearly, the hadronic decay modes $W/Z \rightarrow jj$ are very difficult to observe since particle identification cannot be used to distinguish these processes from (much more frequent) multijet production. One is therefore forced to concentrate on the leptonic decays of the W/Z in order to study gauge boson production. This is made possible by the fact that multijet processes rarely result in a signal which mimics the high-p_T isolated lepton topology characteristic of W/Z production. (Leptons originating from b or c quark decays tend to be found in or near jets.) As will be discussed later, this study involves identification of Z bosons, and attention is focused exclusively on the leptonic decay modes for the reasons outlined above.

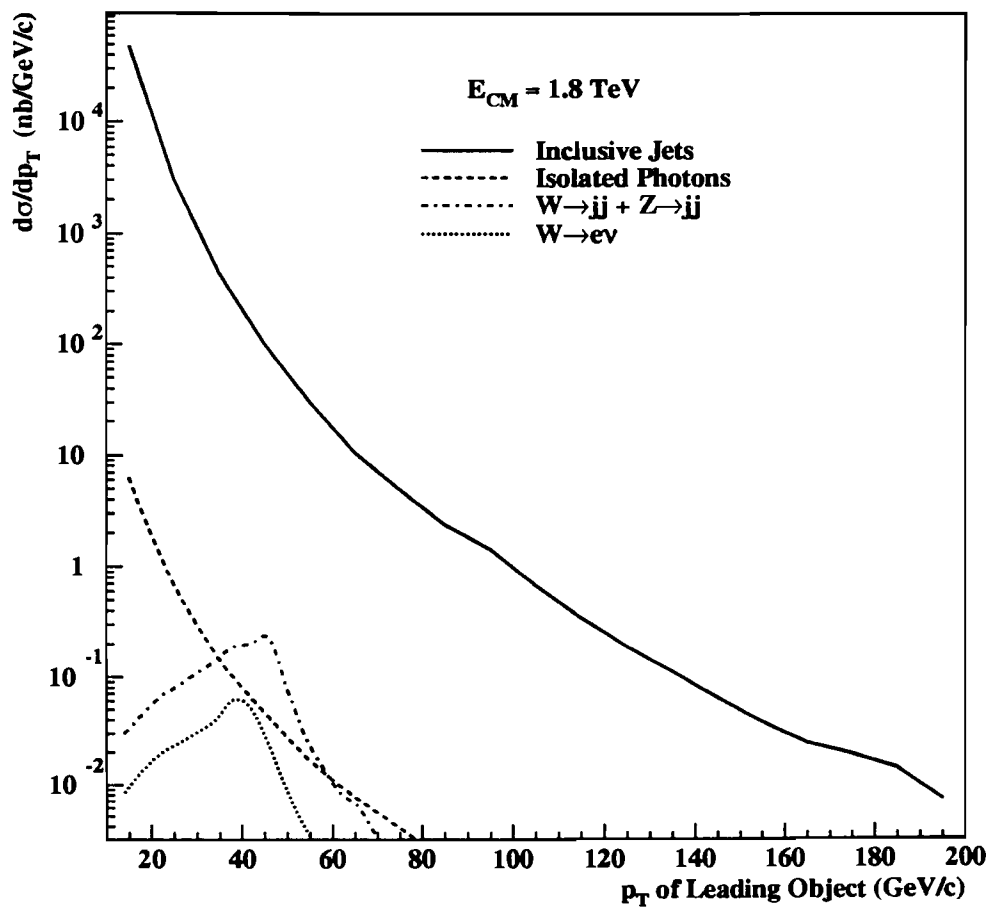

Figure 1.4: Cross sections for various processes at the Tevatron as predicted by the ISAJET Monte Carlo.

Chapter 2

$Z\gamma$ Interactions

This study involves a search for new physics indirectly manifested as interactions between the Z boson and photon. Specifically, evidence for the trilinear $ZZ\gamma$ or $Z\gamma\gamma$ vertices indicated in figure 2.1 would signal new physics. Recall from section 1.1 that such diagrams are not present at tree level within the SM. The blobs in figure 2.1 are meant to represent the underlying details of the specific mechanism(s) responsible for such couplings. (Incidentally, the $\gamma\gamma\gamma$ vertex is forbidden by spin and statistics considerations [19].) This chapter introduces some formalism which provides a quantitative description of $Z\gamma$ interactions. After this formalism is developed, the effects of $Z\gamma$ interactions on experimental observables are discussed, and several possible scenarios are presented which could give rise to such interactions. Finally, recent experimental searches for $Z\gamma$ couplings are reviewed in order to provide a motivation for the present study.

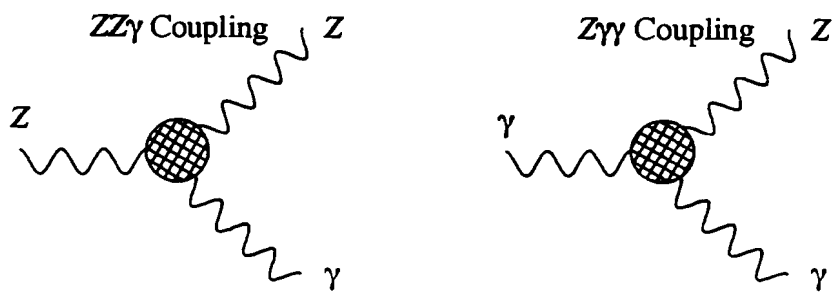

Figure 2.1: $ZZ\gamma$ and $Z\gamma\gamma$ vertices

2.1 Probing $Z\gamma$ Interactions at the Tevatron

The most straightforward way to search for evidence of $Z\gamma$ interactions at the Tevatron is through the study of the $\ell^+\ell^-\gamma$ final state. Here, ℓ denotes electrons or muons; the $\tau^+\tau^-\gamma$ final state is not considered due to high backgrounds. The $\nu\bar{\nu}\gamma$ final state, although interesting, is not considered here either. The main focus of this study will be the $e+e^-\gamma$ channel, but the since the theoretical implications are identical (in the high-energy limit) for the $\mu+\mu^-\gamma$ final state, the $\ell^+\ell^-\gamma$ notation is used in this chapter.

Both the $ZZ\gamma$ and $Z\gamma\gamma$ vertices shown in figure 2.1 contribute to the $\ell^+\ell^-\gamma$ final state. These vertices are probed by searching for events in which a Z^* or γ^* is produced and subsequently undergoes one of the following transitions: $Z^* \rightarrow Z^*\,\gamma$,

$Z^* \to \gamma^* \gamma$, or $\gamma^* \to Z^* \gamma$, where V^* denotes a possibly off-shell vector boson V.

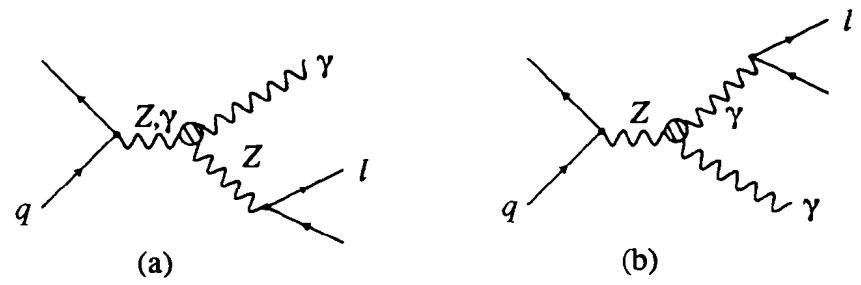

Figure 2.2: Diagrams for $q\bar{q} \to \ell^+\ell^-\gamma$ via $ZZ\gamma$ and $Z\gamma\gamma$ couplings.

Processes exist within the SM which also yield the $\ell^+\ell^-\gamma$ final state and therefore constitute a background to the study of these non-SM processes. As indicated in figure 2.3, these consist of t and u channel $Z\gamma$ "production" (or "initial state radiation") diagrams in which one of the initial state quarks emits a Z or γ, and the radiative "decay" diagrams in which a photon is emitted from one of the decay leptons following s channel Z or γ production. It turns out that the non-SM diagrams of figure 2.2 and the Standard Model diagrams of figure 2.3 interfere constructively, so the existence of non-SM physics is expected to result in a cross section enhancement relative to the Standard Model prediction. To expand on this point further, it is necessary to introduce some formalism, so further discussion of

how $Z\gamma$ interactions affect experimental observables is delayed until section 2.6.

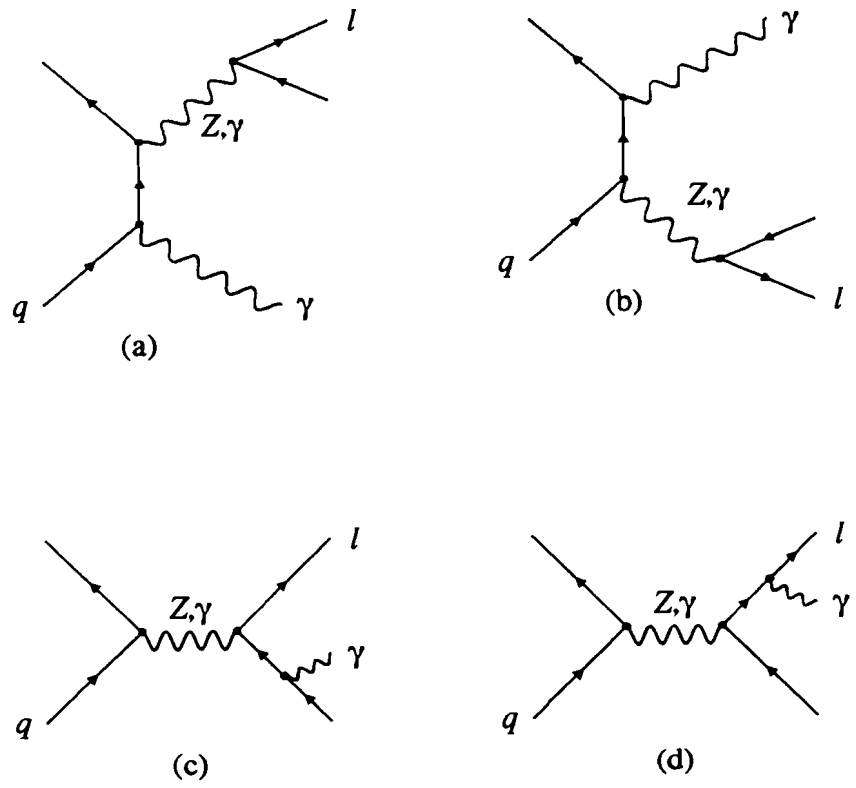

Figure 2.3: Diagrams for $q\bar{q} \rightarrow \ell^+ l^- \gamma$ via Standard Model processes. (a) and (b): Associated $Z\gamma$ production. (c) and (d): Radiative Decays.

2.2 Formalism

Now that the focus of this study has been identified, it is appropriate to explicitly quantify the search for $ZZ\gamma/Z\gamma\gamma$ couplings. To do so, it is necessary to establish a theoretical framework. Since the mechanism(s) responsible for these couplings are unknown *a priori*, this framework must be sufficiently general so that it can accommodate any reasonable source of $Z\gamma$ interactions. Therefore, a formalism is introduced which is similar to that employed in lepton-nucleon scattering [12, 20].

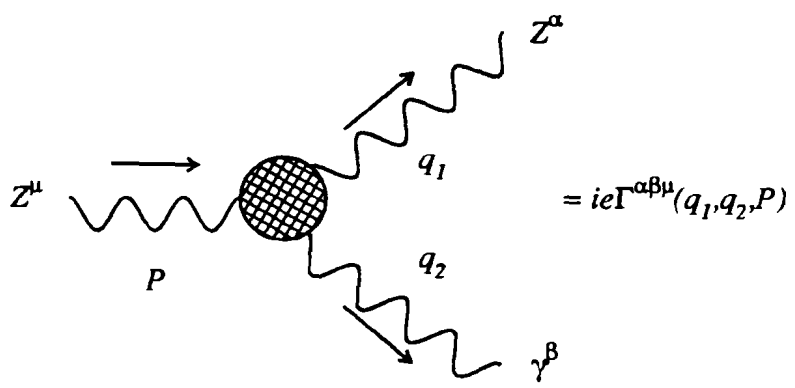

Figure 2.4: The $ZZ\gamma$ vertex function with notation as used in the formalism.

Consider the $ZZ\gamma$ vertex function, denoted $\Gamma_{ZZ\gamma}$, shown in figure 2.4. The vertex function can only depend on the three boson momenta $\{P, q_1, q_2\}$, and the functional dependence of $\Gamma_{ZZ\gamma}$ is restricted by the fact that it must be Lorentz

and gauge invariant.[1] Given these minimal constraints, the vertex function can be expressed as [21, 22, 23]

$$\begin{aligned}\Gamma^{\alpha\beta\mu}_{ZZ\gamma}(q_1,q_2,P) &= \frac{P^2-q_1^2}{M_Z^2}\times \\ &\left\{h_1^Z(q_2^\mu g^{\alpha\beta}-q_1^\alpha g^{\mu\beta})+\frac{h_2^Z}{M_Z^2}P^\alpha[(P\cdot q_2)g^{\mu\beta}-q_2^\mu P^\beta]\right. \\ &\left.+h_3^Z\epsilon^{\mu\alpha\beta\rho}q_2^\rho+\frac{h_4^Z}{M_Z^2}P^\alpha\epsilon^{\mu\alpha\rho\sigma}P_\rho q_{2\sigma}\right\} \qquad (2.1)\end{aligned}$$

where the free parameters h_1^Z, h_2^Z, h_3^Z, and h_4^Z are dimensionless functions of the momenta $\{P, q_1, q_2\}$, and the factors of the Z boson mass, M_Z, have been arbitrarily introduced to make the $\{h_i\}$ dimensionless. The functions h_1^Z and h_2^Z contribute to CP-violating interactions, while h_3^Z and h_4^Z result in CP-conserving interactions. Similarly, the $Z\gamma\gamma$ vertex can be written

$$\begin{aligned}\Gamma^{\alpha\beta\mu}_{Z\gamma\gamma}(q_1,q_2,P) &= \frac{P^2}{M_Z^2}\times \\ &\left\{h_1^\gamma(q_2^\mu g^{\alpha\beta}-q_1^\alpha g^{\mu\beta})+\frac{h_2^\gamma}{M_Z^2}P^\alpha[(P\cdot q_2)g^{\mu\beta}-q_2^\mu P^\beta]\right. \\ &\left.+h_3^\gamma\epsilon^{\mu\alpha\beta\rho}q_2^\rho+\frac{h_4^\gamma}{M_Z^2}P^\alpha\epsilon^{\mu\alpha\rho\sigma}P_\rho q_{2\sigma}\right\} \qquad (2.2)\end{aligned}$$

where the four parameters $\{h_i^\gamma\}$ are analogous to the $\{h_i^Z\}$ in the $ZZ\gamma$ vertex function. Hereafter, all eight parameters will be denoted $\{h_i^V\}$ or simply $\{h_i\}$ where $V = Z, \gamma$ is implied. All h_i are identically zero in the Standard Model.

That only four parameters $\{h^Z_{1\ldots4}\}$ are sufficient to parameterize the $ZZ\gamma$ vertex function follows from spin considerations [22]. As indicated in table 2.1, only

[1] Recall that electromagnetic gauge invariance implies that the interaction is unchanged under the transformation $\epsilon_2^\mu \to \epsilon_2^\mu + \lambda q_2^\mu$. The allowed functional dependence of $\Gamma_{Z\gamma Z}$ on the boson momenta and polarizations is discussed further in reference [21].

J_Z^3	J_γ^3	$J_{\min}$	Transition
+1	+1	2	forbidden
+1	−1	0	allowed
0	+1	1	allowed
0	−1	1	allowed
−1	+1	0	allowed
−1	−1	2	forbidden

Table 2.1: Summary of $Z^* \to Z\gamma$ transitions allowed by spin conservation.

four of the total six possible final state spin combinations are accessible by the $J = 1$ channel, which implies that there are only four independent helicity amplitudes to be considered. This is also true for the $Z\gamma\gamma$ vertex as well.

2.3 Self Consistency

At this point, the functional dependencies of the $\{h_i\}$ on $\{P, q_1, q_2\}$ are undetermined since they depend on the specifics of unknown new physics. However, self-consistency of the formalism places restrictions on the high-energy behavior of the $\{h_i\}$ and allows a reasonable guess to be made regarding their functional forms. Using the vertex function from equation 2.1 to compute the scattering amplitude (or matrix element) for the diagrams in figures 2.2 and 2.3, one finds that the energy behavior of the contributions from $ZZ\gamma$ couplings are [23]

$$\Delta\mathcal{M} \sim (\sqrt{\hat{s}}/M_Z^2)^3$$

for $h_{1,3}$, and

$$\Delta\mathcal{M} \sim (\sqrt{\hat{s}}/M_Z^2)^5$$

for $h_{2,4}$. Here, $\sqrt{\hat{s}}$ is the energy of the collision in the quark-antiquark center of mass frame. Clearly, this is an indication that the $\{h_i\}$ cannot be constants. Otherwise, the amplitudes diverge at high energies, which is unphysical; the $\{h_i\}$ must tend toward zero as $\hat{s}$ increases to avoid this behavior.

Fortunately, a precedent for this type of situation exists: elastic lepton-nucleon scattering. In this case, the high energy differential cross section is approximated by [20]

$$\frac{d\sigma}{dq^2} = \frac{4\pi\alpha^2}{q^4}\left[\frac{G_E^2 + \frac{|q^2|}{4M^2}G_M^2}{1 + \frac{|q^2|}{4M^2}}\right]$$

where q is the momentum transfer associated with the virtual photon, M is the nucleon mass, and the quantities G_E and G_M are the electric and magnetic nucleon form factors, respectively. Empirically, it is found that the form factors of the proton are described by

$$G_E^p = \frac{G_M^p}{\mu_p} = \frac{1}{(1 + \frac{|q^2|}{\Lambda^2})^2} \tag{2.3}$$

where μ_p is the proton magnetic moment, and Λ is referred to as the form factor scale. A fit to experimental data favor $\Lambda^2 = 0.71$ GeV^2. Physically, equation 2.3 represents the Fourier transform of of an exponentially decaying charge distribution with spatial extent described by the parameter Λ. The form factor scale also has

another interpretation: as momentum transfers become higher ($-q^2 \geq \Lambda^2$), the virtual photon becomes sensitive to the individual (quark) charges inside the proton, and the proton is easily broken apart. Inelastic processes become more likely, so the elastic form factors (and cross section) become smaller and approach zero. The onset of such non-elastic physics is characterized by the scale Λ. This behavior is just what is needed to regulate the high energy behavior of the $\{h_i\}$ functions in the case of $Z\gamma$ interactions.

Motivated by this example, the functional forms of the $\{h_i^V\}$ are assumed to be described the generalized dipole form factor ansatz

$$h_i^V = \frac{h_{i0}^V}{(1+\hat{s}/\Lambda^2)^{n_i}} \tag{2.4}$$

where the Λ is the form factor scale, n_i is the form factor power, and the $\{h_{i0}^V\}$ are form factor coupling strengths. form factor is the special case of $n = 2$.) In practice, these coupling strengths are measured experimentally for a fixed values of Λ and n_i. Figure 2.5 illustrates the form factor behavior of equation 2.4 as a function of the energy $\sqrt{\hat{s}}$ for different values of the form factor scale. For $\sqrt{\hat{s}} \ll \Lambda$, the form factors are relatively independent of energy[2], which implies that experiments limited to this regime are insensitive to the physics at scale Λ. This energy insensitivity of the form factors is analogous to the case of low-energy lepton-nucleon scattering in which the wavelength of the virtual photon is sufficiently large that the nucleon substructure

[2]Formally, $(1+\hat{s}/\Lambda^2)^{-n} \approx 1 - n\hat{s}/\Lambda^2$ for $\sqrt{\hat{s}} \ll \Lambda$, and therefore the form factors are approximately constant in this limit.

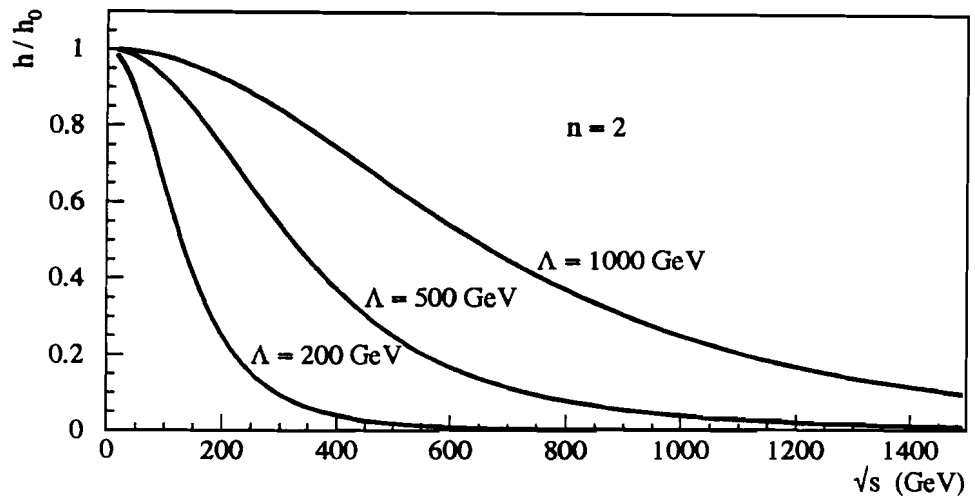

Figure 2.5: Form factor behavior as a function of the parton subprocess center-of-mass energy for different values of the form factor scale Λ.

is unresolved. At higher energies, the pointlike quark charges are resolved and the form factor decreases.

The form factor ansatz (2.4) was motivated by the desire to regulate the high energy behavior of scattering amplitudes. However, not all values of $\{h_{i0}\}$, Λ, and $\{n_i\}$ will solve this problem. For example, it is clear that the amplitudes will diverge for $n_i < 0$, regardless of Λ. The allowed values of these parameters which result in non-divergent amplitudes can be found by decomposing the amplitude into partial waves. The amplitude for the fermion annihilation process $f\bar{f} \to Z\gamma$ can be written

as [20, 24]

$$\mathcal{M}(\sigma\bar{\sigma}, \lambda_Z\lambda\gamma) = 16\pi \sum_J (2J+1)\mathcal{T}^J_{\lambda_Z\lambda\gamma} d^J_{\sigma-\bar{\sigma},\lambda_Z-\lambda\gamma}(\theta) \tag{2.5}$$

where σ, $\bar{\sigma}$, λ_Z, and $\lambda\gamma$ denote the helicities of the intial state fermions and final state Z and γ, respectively. The T-matrix amplitude of partial wave J is denoted $\mathcal{T}^J$, and $d(\theta)$ are the familiar d functions which are related to spherical harmonics. Bounds on the $\mathcal{T}^J$ can be derived from probability conservation considerations; this is generally referred to as "S-Matrix Unitarity". Such bounds are often useful due to the very general nature of the assumptions made in their derivation. The authors of references [23, 24] have used this technique for the $J = 1$ partial amplitude to place bounds on the form factor powers $\{n_i\}$ and coupling strengths $\{h_{i0}\}$ for given values of the form factor scale Λ and the center of mass energy $\sqrt{\hat{s}}$. They found that $n > \frac{3}{2}$ for $\{h_{10}, h_{30}\}$ and $n > \frac{5}{2}$ for $\{h_{20}, h_{40}\}$ are required to satisfy unitarity for all values of $\sqrt{\hat{s}}$, regardless of the form factor coupling strengths or scale. Similarly, if the form factor powers $\{n_i\}$ are fixed, bounds can be placed on the coupling strengths $\{h_{i0}\}$. Figure 2.6 shows the simultaneous exclusion contours for the pair (h^Z_{30}, h^Z_{40}) for different values of Λ assuming that $h^Z_{10} = h^Z_{20} = h^\gamma_i = 0$, $n_3 = 3$, and $n_3 = 4$. As Λ is increased, the form factors effectively extend out to higher energies, so the coupling strengths are required to be weaker to ensure that unitarity is not violated.

For the purposes of this study, it is assumed that $n = 3$ for $\{h^V_{10}, h^V_{30}\}$, and $n = 4$ for $\{h^V_{20}, h^V_{40}\}$. Aside from satisfying the lower bounds of $\frac{3}{2}$ and $\frac{5}{2}$ required by

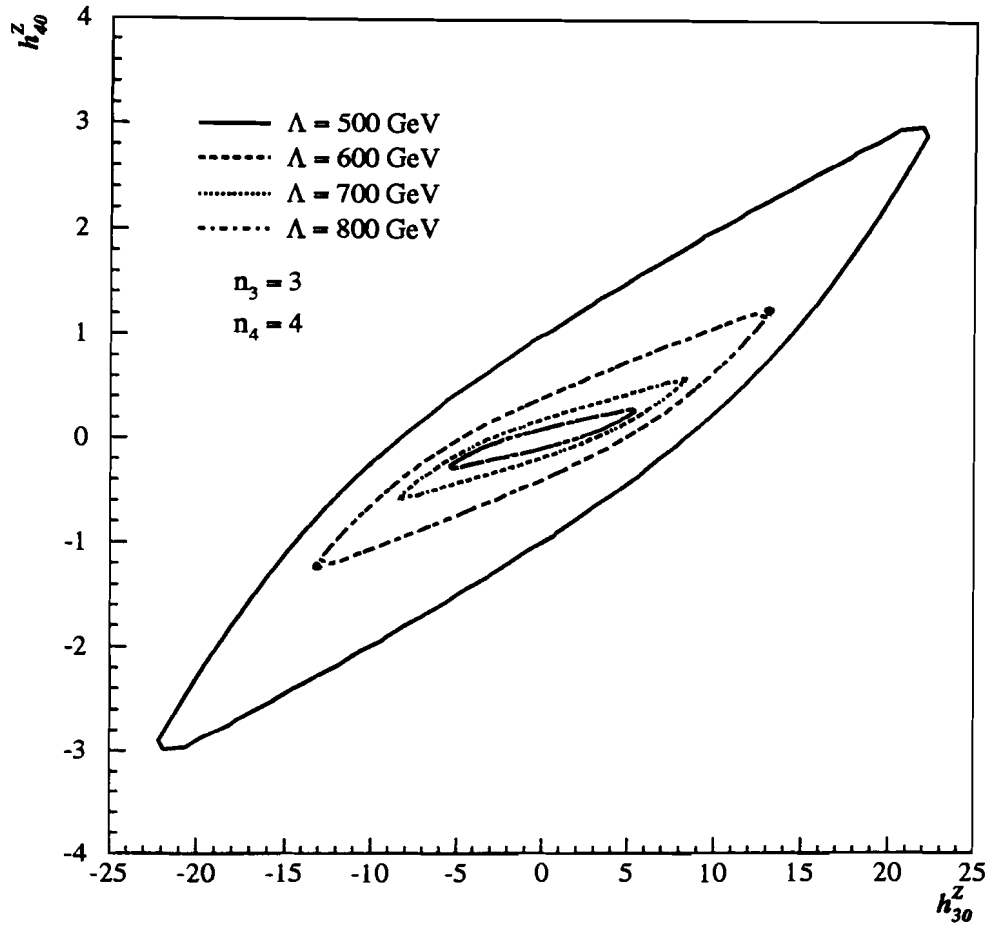

Figure 2.6: Exclusion regions for the couplings h^Z_{30} and h^Z_{40} based on unitarity for different values of the form factor scale Λ.

unitarity considerations, these choices also result in the same high-energy behavior of terms containing the various $\{h_{i0}\}$ [23]. This assumption also maximizes the interference between these terms, so experimental limits placed on the couplings are consequently conservative. Another important assumption involves the form

factor scale: $\Lambda \equiv 500$ GeV. As will be discussed later, this choice ensures that the experimental limits on the coupling strengths $\{h_{i0}\}$ are more stringent than unitarity bounds alone. Higher values of Λ can be probed by more sensitive future experiments. As a practical matter, the above choices allow direct comparisons to be made between contemporary experiments since identical choices have been made elsewhere. Finally, it is not necessary that the above choices are "correct"; they simply define the context in which the search for $Z\gamma$ interactions takes place. Any experimental limits on the couplings must be accompanied by enough information to completely specify the context.

2.4 Manifestations of $Z\gamma$ Interactions

Given the theoretical framework for $Z\gamma$ interactions, it is now possible to quantitatively examine how such phenomena might affect experimental observables. To this end, it is advantageous to first consider the kinematics of the Standard Model "background" $q\bar{q} \to \ell^+\ell^-\gamma$ processes of figure 2.3. It should be noted that these leading order diagrams contain infrared and collinear singularities in the massless fermion approximation. The infrared singularities occur as the photon energy approaches zero, while the collinear singularities occur as the emission angle relative to the initial or final state particles approaches zero. However, an actual detector cannot resolve arbitrarily soft photons or photons which are not spatially separated

from other final state particles, so the regions of phase space containing the singularities are not experimentally accessible.[3] The kinematic criteria listed below in table 2.2 are sufficient to avoid the singularities and represents the phase space which is generally within the reach of most detectors.

Three-body invariant mass:	$m_{\ell^+\ell^-\gamma} > 20$ GeV
Dilepton invariant mass:	$m_{\ell^+\ell^-} > 10$ GeV
Lepton transverse momentum:	$p_T^{\ell\pm} > 10$ GeV
Photon transverse momentum:	$p_T^{\gamma} > 10$ GeV
Lepton angular acceptance:	$\lvert\eta_{\ell\pm}\rvert < 4.5$
Photon angular acceptance:	$\lvert\eta_{\gamma}\rvert < 4.5$
Lepton-Photon angular separation:	$\Delta\mathcal{R}_{\gamma\ell\pm} > 0.7$

Table 2.2: Kinematic criteria used to define the phase space of the experimentally "visible" cross section.

Here, η is the pseudorapidity, which is defined by $\eta = -\ln(\tan\frac{\theta}{2})$ where θ is the polar angle measured with respect to the z (beam) axis. The angular separation $\Delta\mathcal{R}$ is defined by

$$\Delta\mathcal{R} = \sqrt{(\Delta\eta)^2 + (\Delta\phi)^2}$$

where $\Delta\eta$ is the polar angular separation and $\Delta\phi$ is the azimuthal angular separation of two given objects. In general, the initial state q and $\bar{q}$ carry different fractions of the p and $\bar{p}$ momenta, so the $q\bar{q}$ center of mass has a net z momentum

[3]Due to the presence of singularities in the absence of kinematic cuts, the total cross section is somewhat ill-defined, since it depends on the necessarily restricted phase space under consideration. In practice, the predicted event yield is a more meaningful quantity since it is reflects the experimentally accessible phase space.

in the laboratory frame. Therefore, the angular separation is defined in terms of the pseudorapidity so that it is invariant under boosts in the z direction; $\Delta\mathcal{R}$ is approximately the same in the lab and center of mass frames.

Figure 2.7 shows the invariant mass and transverse momentum distributions for Standard Model $q\bar{q} \to \ell^+\ell^-\gamma$ in $p\bar{p}$ collisions at $\sqrt{s} = 1.8$ TeV subject to the requirements of table 2.2. These distributions were made using the Monte Carlo generator provided by the authors of reference [23] and the MRSD'_ pdf set [16, 17]. The total visible cross section (within the phase space defined by table 2.2) is 5.52 pb for the combined electron and muon channels. In these plots, the production and decay contributions are indicated by the dashed and dotted lines, respectively. The three body mass distribution shows a peak near the Z boson mass ($M_Z \approx 91.2$ GeV) which is due to radiative decays and a high mass tail due to $Z\gamma$ production. Conversely, the dilepton mass contains a peak near M_Z due to production and another peak at lower masses due to radiative decays in which the one of the final state leptons has lost energy to the final state photon. The dip between the peaks is a consequence of the particular set of kinematic cuts used here and becomes less prominent as the ΔR and p_T^γ cuts are relaxed. The photon p_T distribution is dominated by radiative decays out to the kinematic limit of $p_T \approx M_Z/2$.[4] At higher p_T, the spectrum is dominated by production. The lepton transverse momenta

[4] Recall that the transverse momentum distribution of Z boson decay products exhibits a so-called Jacobian peak near the endpoint at $p_T \approx M_Z/2$ for Z bosons produced at rest. See reference [12], section 8.5 for details.

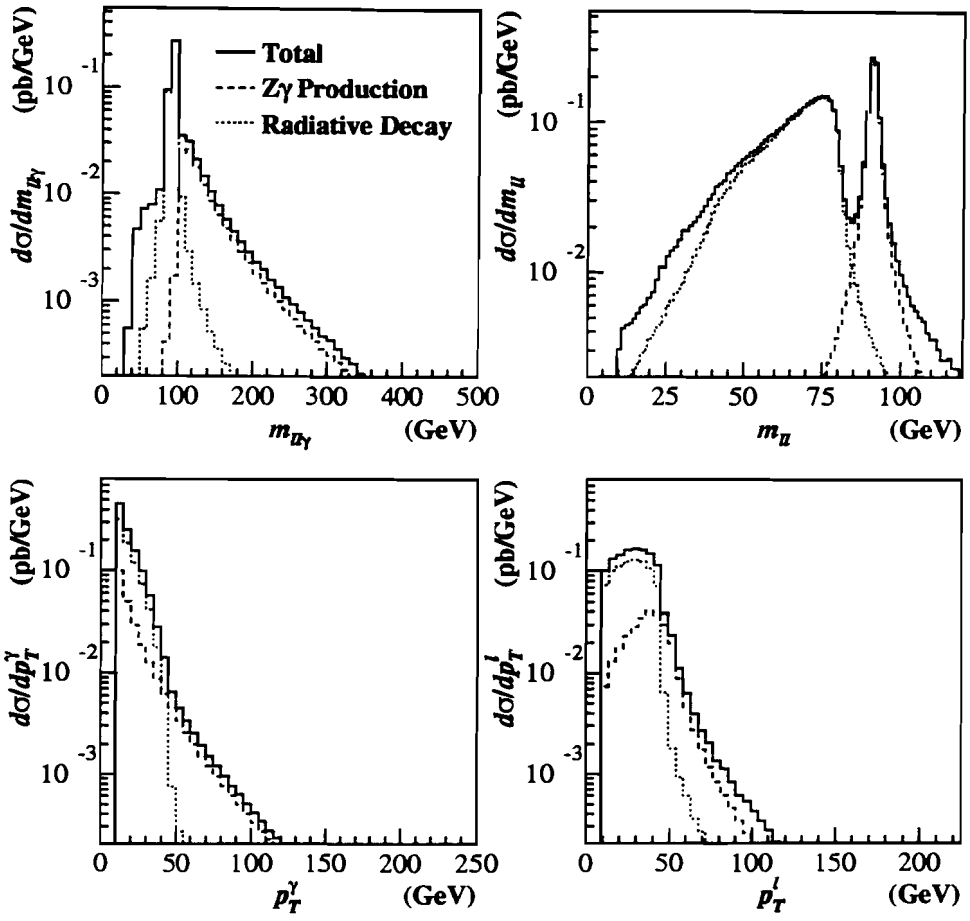

Figure 2.7: Invariant mass and transverse momentum distributions of the final state products in Standard Model $p\bar{p} \to \ell^+\ell^-\gamma$ at $E_{\rm CM} = 1.8$ TeV.

follow similar trends, with the region below $M_Z/2$ dominated by radiative decays, and the region above $M_Z/2$ dominated by production.

Figure 2.8 shows the angular separation and pseudorapidity distributions for

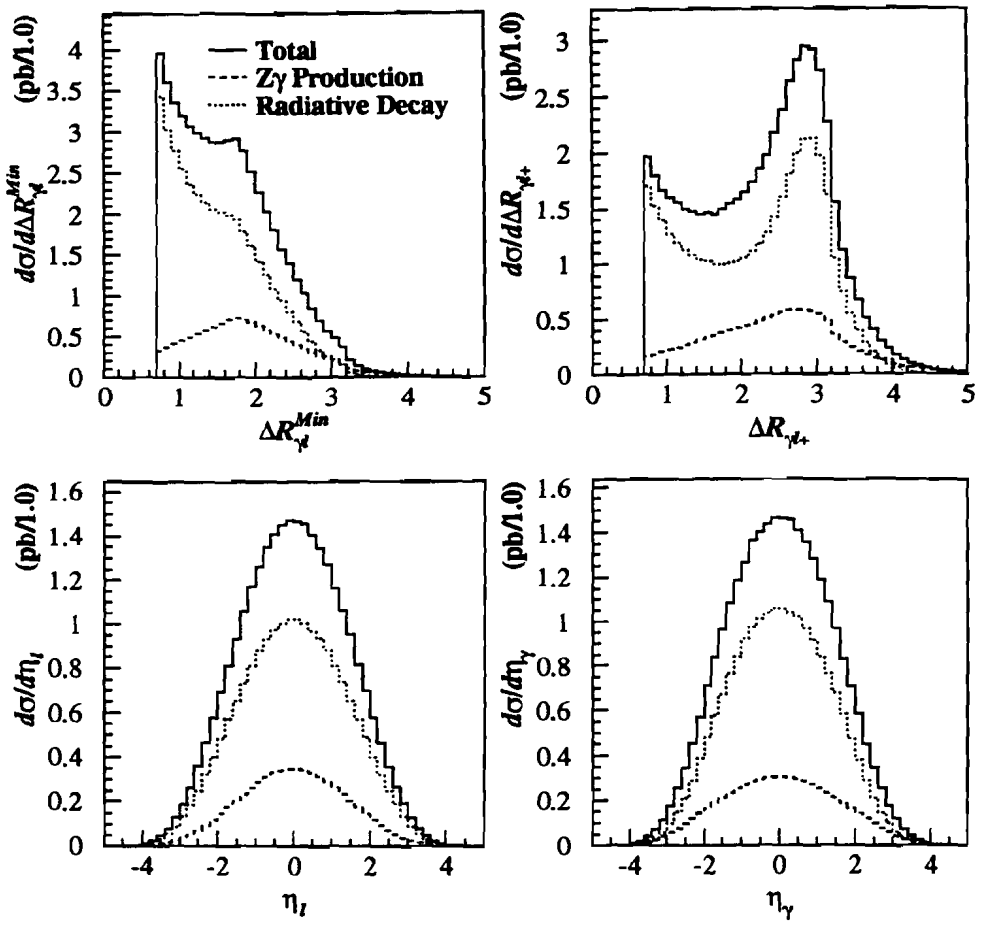

Figure 2.8: Angular distributions of the final state products in Standard Model $p\bar{p} \to \ell^+\ell^-\gamma$ at $E_{\rm CM} = 1.8$ TeV.

the final state particles. As expected, the separation between the photon and nearest lepton, denoted $\Delta\mathcal{R}_{\rm Min}$, peaks near the imposed cutoff of 0.7 for the radiative decay contribution. (The collinear singularity occurs as $\Delta\mathcal{R}_{\rm Min} \to 0$.) The production contribution is most significant at large separations. The distribution of the

$\gamma\ell^+$ separation exhibits similar characteristics. The peak at small values of $\Delta\mathcal{R}_{\gamma\ell^+}$ originates from radiation off of the ℓ^+, while the peak at $\Delta\mathcal{R}_{\gamma\ell^+} \approx \pi$ is due mostly to a radiation from the ℓ^-. (The $Z \to \ell^+\ell^-$ decay tends to yield back-to-back leptons with $\Delta\phi \approx \pi$, so bremsstrahlung off of the opposite lepton peaks at $\Delta\mathcal{R}_{\gamma\ell^+} \approx \pi$.) On the other hand, $Z\gamma$ production contributes most at large values of separations. In terms of angular distributions, the decay contributions are more centrally peaked (toward $\eta = 0$) than the production contributions for both the photon and leptons. This is due to the characteristic t channel forward-backward pole which originates from the fermion propagator. In the $q\bar{q}$ center of mass, the angular distribution is roughly proportional to $1/\hat{t}^2$ or $1/(1-\cos\hat{\theta})^2$ for production.

As mentioned earlier, the existence of non-SM $Z\gamma$ couplings is manifested by an increase in the total cross section relative to the SM expectation. This excess depends on the coupling values, and the terms containing the contributions from different couplings can interfere appreciably with one another. Interference effects are strongest for the coupling pairs (h_{10},h_{20}) and (h_{30},h_{40}) [23]. These interference effects are illustrated in figure 2.9, which shows the cross section as a function of the h_{30}^Z and h_{40}^Z. If no interference were present, the surface $\sigma(h_{30}^Z, h_{40}^Z)$ would have elliptical cross sectional contours with the major axis along either the h_{30}^Z or h_{40}^Z axis. In this case, the major axis is oriented about 15° from the h_{30}^Z axis, so interference effects are non-negligible. Therefore, it is necessary to consider cases in which both h_{30}^Z and h_{40}^Z are simultaneously varied from their SM (zero) values

when searching for $ZZ\gamma$ couplings. Otherwise, regions of parameter space in which interference is significant might be overlooked. Similar considerations must be made when searching the $Z\gamma\gamma$ coupling parameter space. Finally, it should be noted that interference effects between $ZZ\gamma$ and $Z\gamma\gamma$ couplings are small [23], so the two types of couplings can be varied independently with minimal consequences.

The cross section contribution due to $Z\gamma$ interactions occurs mainly in regions of phase space where the SM contributions are small. Figures 2.10 and 2.11 show the invariant mass, transverse momentum, and angular distributions expected for $h_{30}^{Z} = 2$ along with the SM case of $\{h_{i0}\} = 0$ for comparison. As discussed earlier, it is assumed that $\Lambda = 500$ GeV and $n = 3$. The resulting cross section is 6.61 pb for the combined electron and muon decay modes, which represents an increase of about 20% relative to the SM cross section.

Aside from the larger total cross section, the non-zero $Z\gamma$ coupling results in enhanced tails in the dilepton-photon invariant mass distribution, the photon transverse momentum distribution, and the lepton transverse momentum distribution. Also, the dilepton invariant mass peak near M_Z is enhanced; more on-shell Z bosons are produced if $Z\gamma$ interactions exist than would be expected from the SM alone. In terms of angular distributions, $Z\gamma$ interactions result in more central events with larger separations between the photon and leptons than in the SM case. Most of these effects can be attributed to the fact that non-SM $l^+\ell^-\gamma$ production takes place in the s channel, which results in larger contributions in the central

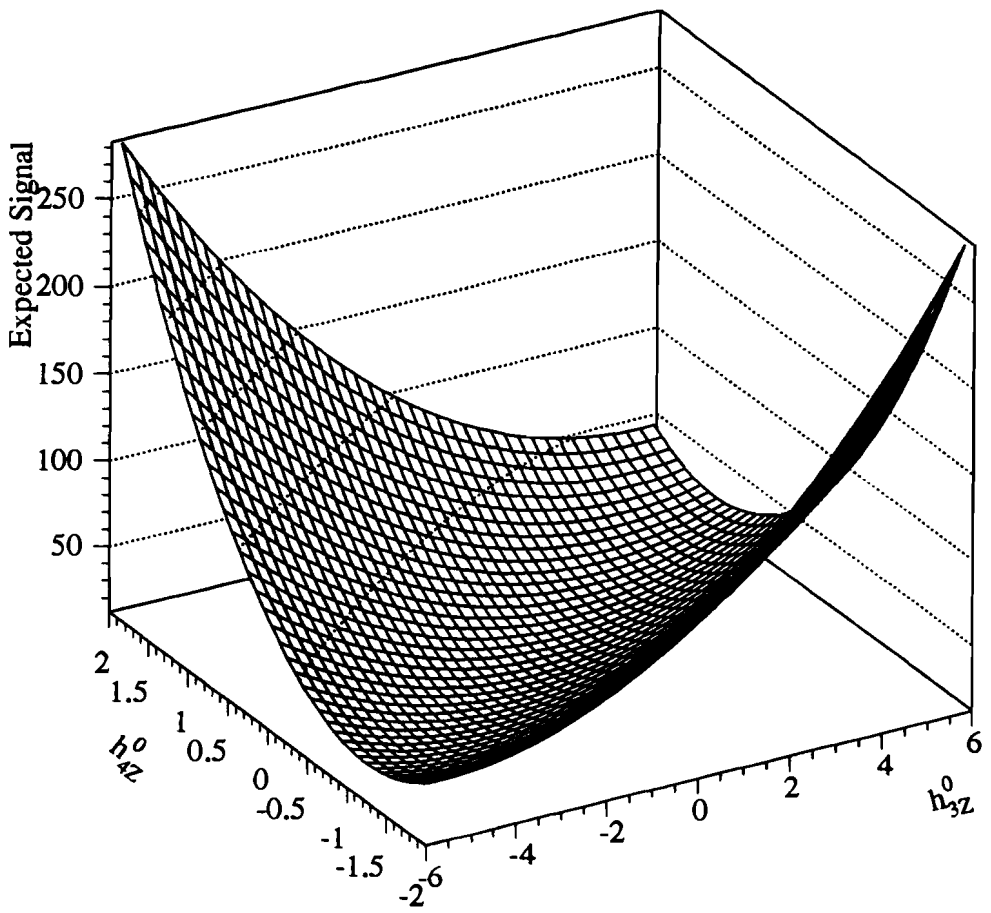

Figure 2.9: Predicted cross section for $p\bar{p} \to \ell^+\ell^-\gamma$ at $E_{\rm CM} = 1.8$ TeV as a function of h^Z_{30} and h^Z_{40}.

region at high p_T than the SM t channel contributions.

In summary, $Z\gamma$ interactions result in higher cross sections than would be expected from SM $l^+\ell^-\gamma$ processes. These cross section enhancements are concentrated in regions of phase space characterized by high invariant masses and high

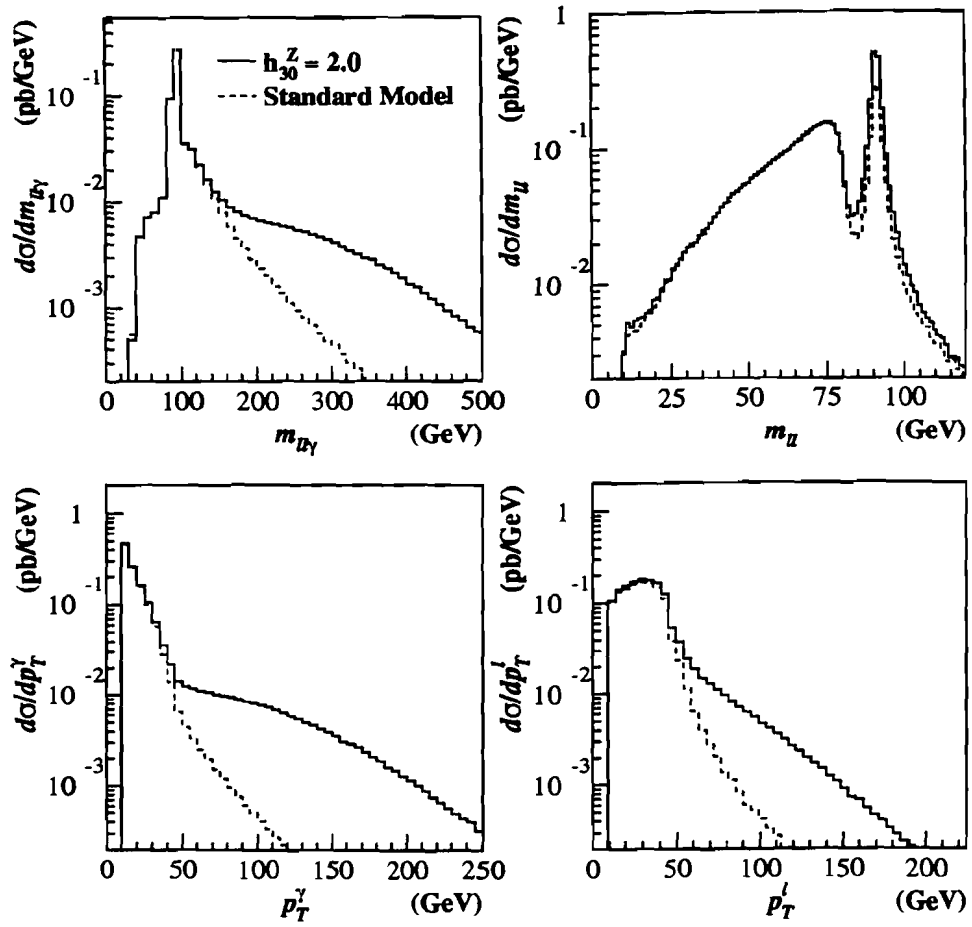

Figure 2.10: Invariant mass and transverse momentum distributions of the final state products in $p\bar{p} \to \ell^+\ell^-\gamma$ at $E_{\rm CM} = 1.8$ TeV case of $h_{30}^Z = 2$.

transverse momenta at small rapidities. Although it is clear that several kinematic variables are sensitive to non-SM physics, this study will concentrate mainly on the photon transverse momentum. One advantage of this variable is that it is relatively insensitive to the lepton momentum resolution, so results from different channels

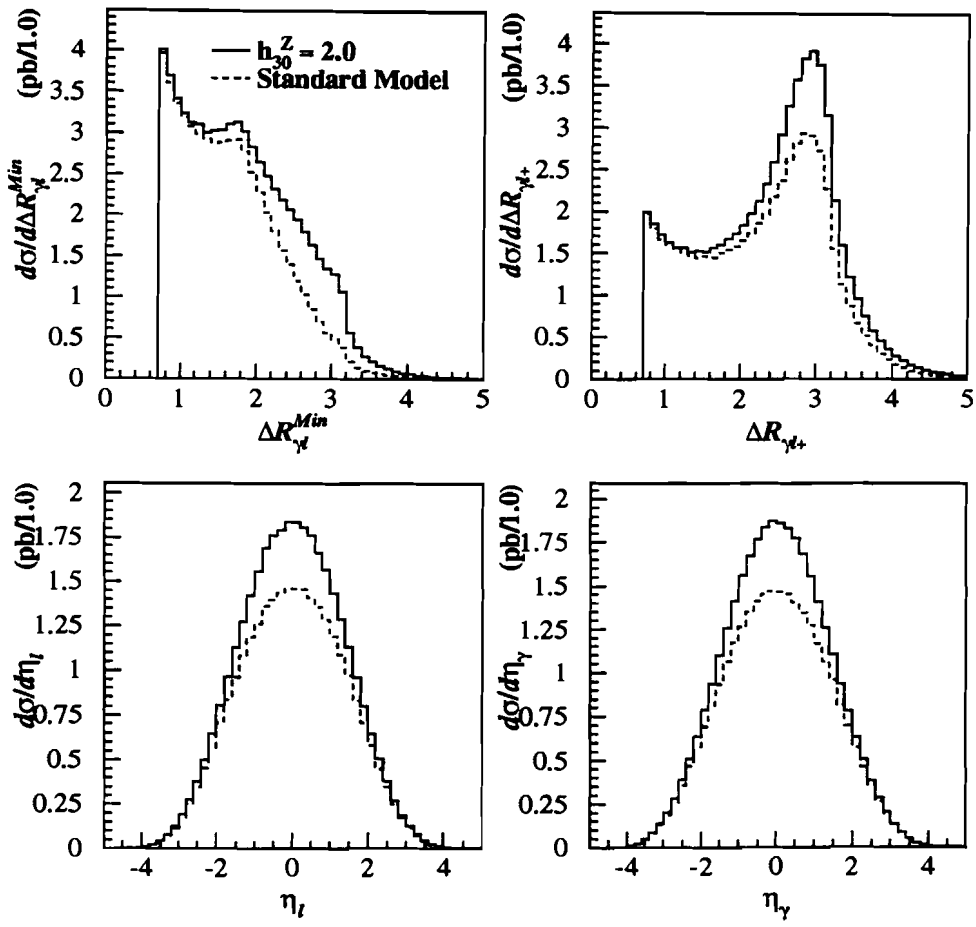

Figure 2.11: Angular distributions of the final state products in $p\bar{p} \to \ell^+\ell^-\gamma$ at $E_{\rm CM}$ = 1.8 TeV for the case of $h_{30}^Z = 2$.

can be easily combined when extracting limits on couplings.

2.5 NLO Corrections

The calculations used in the previous section were based on leading order calculations, so it is natural to ask whether the conclusions differ when next-to-leading order (NLO) corrections are included. Such corrections have been calculated for the $Z\gamma$ production diagrams [25] and involve both internal virtual gluon loops and initial state gluon radiation. The virtual gluon loops do not change the $l^+\ell^-\gamma$ final state signature, but they do affect the cross section since they effectively modify quark propagators and vertex factors. The QCD radiation diagrams, indicated schematically in figure 2.12, result in an additional gluon in the final state which may be detected as a hadronic jet if it is sufficiently energetic. There are also additional quark-gluon fusion diagrams which must be included, but their contribution is small at Tevatron energies.

Recall from section 2.4 that the photon spectrum is sensitive to $Z\gamma$ interactions above ~ 50 GeV, and that SM $Z\gamma$ production is the main background source in this kinematic region. It is therefore sufficient to consider only corrections to SM $Z\gamma$ production in this regime in order to estimate how NLO corrections affect sensitivity to $Z\gamma$ interactions.

The NLO corrections to $Z\gamma$ production are small at Tevatron energies. Figure 2.13 shows the ratio of the NLO and LO differential cross sections as a function

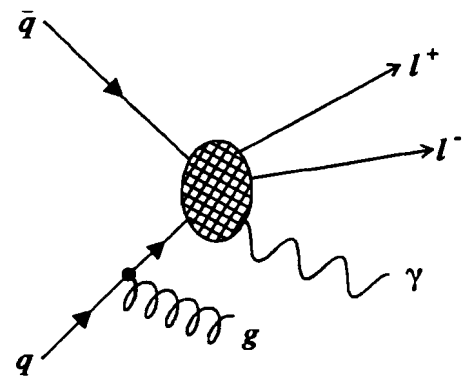

Figure 2.12: Correction to $q\bar{q} \to \ell^+\ell^-\gamma$ due to QCD initial state radiation.

of the photon transverse momentum. In the range from 50 to 100 GeV, where sensitivity is to $Z\gamma$ interactions is highest, the ratio changes by about 10%. Since this ratio is relatively constant, a so called k-factor [12] can be used approximate the NLO result in terms of the LO calculation:

$$\sigma_{\rm NLO} \approx k\, \sigma_{\rm LO}.$$

Since no full NLO calculation of the $p\bar{p} \to \ell^+\ell^-\gamma$ (incorporating radiative decays and possible non-SM $Z\gamma$ interactions) is available, the k-factor approach is used in this study. The leading order calculation is used with $k = 1.34$ to account for higher order corrections.[5]

[5]Formally, $k = 1 + \frac{8}{9}\pi\alpha_s$ along with the approximation $\alpha_s(M_Z) \approx 0.12$ is used.

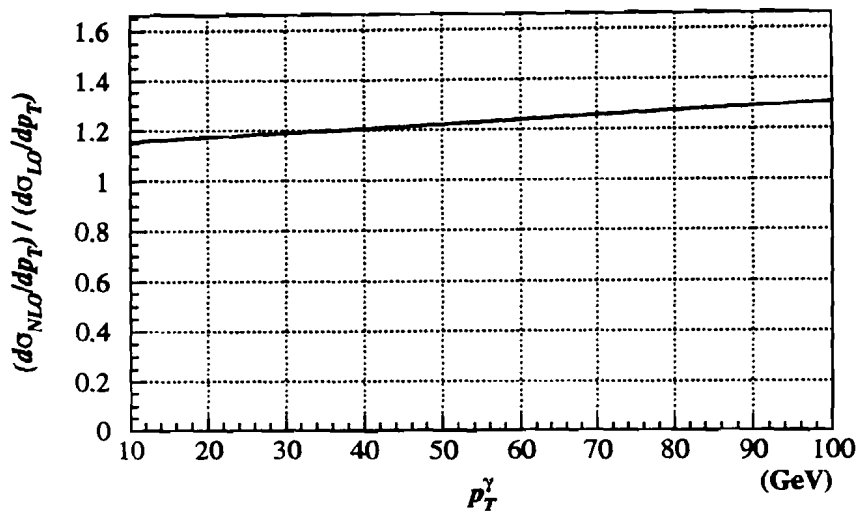

Figure 2.13: Ratio of NLO to LO predicted cross section for $p\bar{p} \rightarrow \ell^+\ell^-\gamma$ at $E_{\rm CM}$ = 1.8 TeV as a function of the photon transverse momentum.

2.6 Possible Sources of $Z\gamma$ Interactions

There are several possible mechanisms which could result in $Z\gamma$ interactions. For example, if the Z boson is a composite particle with constituents which couple to the electromagnetic field, a situation similar to that shown in figure 2.14 can be expected. That is, an exited composite Z can decay radiatively into a Z and γ. Several theories have been proposed which incorporate this idea [26, 27, 28, 29, 30, 31]. Most share the same basic premise: matter is composed of spin-$\frac{1}{2}$ particles ("preons", "Rishons", "haplons") and the the weak interactions are realized as residual interactions among these particles. In this scenario, the weak interactions among

quarks and leptons are analogous to low energy strong interactions between nucleons via effective pion exchange [40]. The substructure of the "effective" intermediate boson becomes apparent only at high energies. In terms of the formalism devel-

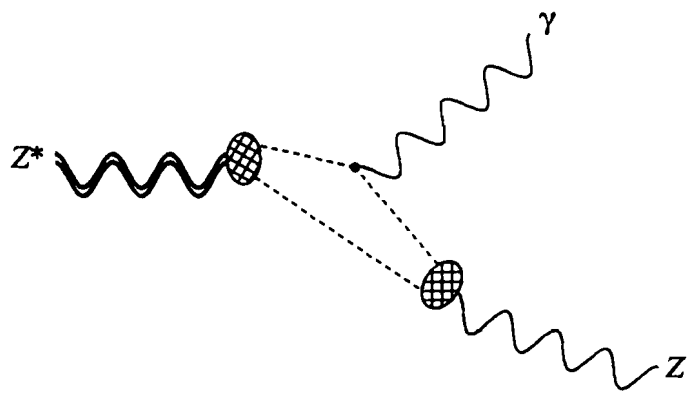

Figure 2.14: Composite Z Boson Scenario.

oped in section 2.2, composite bosons are expected to result in $\{h_i\}$ of order 0.1-1.0 [41], depending on the compositeness scale and how the constituents couple to the photon.

Loop corrections due to new particles could also result in effective $Z\gamma$ interactions. Such a scenario is shown in figure 2.15. These effects are difficult to observe experimentally due to the fact that the contributions to the $ZZ\gamma$ vertex are suppressed by the three coupling factors at the triangle vertices. Also, triangle diagrams will be suppressed by propagator factors if the loop particles are heavy [21]. If the

final state Z and γ are on-shell, the loops due to SM fermions give zero contributions [42]. For off-shell Z or γ, the SM fermion loop contributions result in couplings on the order of 10^{-4} [23], which is beyond the sensitivity attainable by any foreseeable experiment. Thus, one only expects to observe such effects if the particles in the loop couple strongly to the Z and γ and/or are relatively light. As a specific example, the authors of reference [32] address the case of a simple two-Higgs doublet. There are four physical Higgs scalars in this model; the three neutral states can participate in the loop and give rise to CP-violating $Z\gamma$ interactions corresponding to very small coupling values on the order of 10^{-6}.

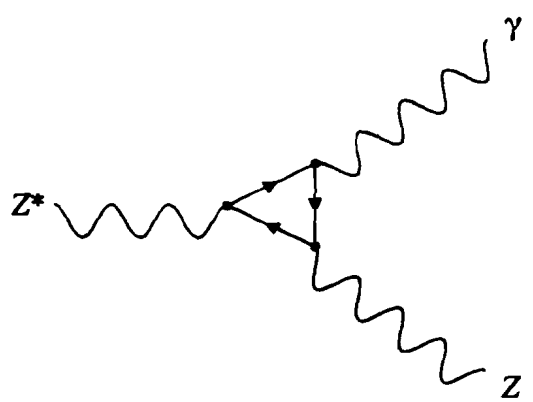

Figure 2.15: Contribution to neutral gauge boson couplings due to loop effects.

Although the radiative decays of exited leptons are not strictly classified as anomalous $Z\gamma$ interactions, their existence might be accidentally interpreted as such

if leptonic Z decays are being observed. As shown in figure 2.16, such exited leptons can be produced via Z boson or γ^* decay. The leptons can then decay radiatively in a manner similar to the composite Z case described earlier. This scenario received much attention [33, 34, 35, 36, 37] when only a handful of Z decays had been observed [10, 11] and an anomalously large fraction were radiative decays. After more data were collected, the exited lepton hypothesis was ruled out for masses below M_Z [43]. Nevertheless, the search for leptonic structure continues as higher energies are reached [38].

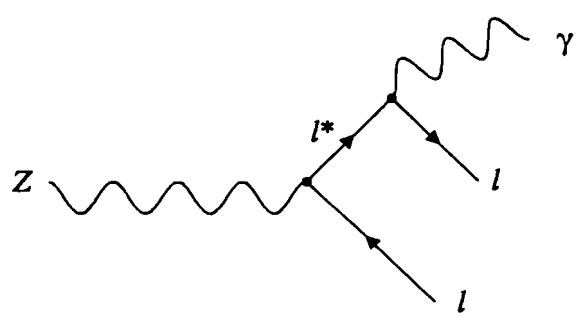

Figure 2.16: Contribution to $l^+l^+\gamma$ production due to exited lepton decay.

2.7 Previous Experimental Limits

Present experimental limits on $ZZ\gamma$ and $Z\gamma\gamma$ couplings can be divided into two categories: low energy bounds and high energy bounds. The low energy bounds are based on measurements at energies below ~ 1 GeV which limit loop contributions involving the $ZZ\gamma$ and $Z\gamma\gamma$ vertices. Currently, controversy exists among experts regarding the validity of the assumptions made in calculations which are used to extract the bounds from experimental data. Bounds which depend on powers of the loop cutoff parameter Λ are the most sensitive to dynamical assumptions, so those involving only logarithmic cutoff dependences are likely to be most reliable [23, 44, 45, 46, 47]. One such bound has been derived by computing [50] the contribution of the $Z\gamma\gamma$ vertex to the muon anomalous magnetic moment $(g-2)_\mu$ indicated in figure 2.17. Present $(g-2)_\mu$ experimental data [49] result in the limit of

$$|h_3^\gamma \ln(\frac{\Lambda^2}{M_Z^2})| < 9$$

under the assumption that the other $h_i^\gamma = 0$. For a scale of $\Lambda = 500$ GeV, this translates to a limit of

$$|h_3^\gamma| < 2.7$$

A Brookhaven experiment (E821) aims to improve the precision of the $(g-2)_\mu$ measurement by a factor of 20, so this limit should improve significantly in the future. However, it should be kept in mind that interference effects can weaken these bounds significantly if the couplings are allowed to vary simultaneously from

their SM values.

A similar calculation has not yet been performed for the well measured [51] neutron (quark) dipole moments. However, in the case of anomalous $WW\gamma$ couplings, this procedure results in very tight limits ($< 10^{-4}$) on the CP-odd couplings $\Delta\tilde{\kappa}$ and $\tilde{\lambda}$ [47, 48], so it is plausible that similarly stringent limits can be placed on the CP-odd $ZZ\gamma$ and $Z\gamma\gamma$ couplings as well. Therefore, for the purposes of this study, it is assumed that

$$\boxed{h_1^\gamma \equiv h_2^\gamma \equiv h_1^Z \equiv h_2^Z \equiv 0} \tag{2.6}$$

and the search for $Z\gamma$ interactions is restricted to the remaining CP-even couplings.

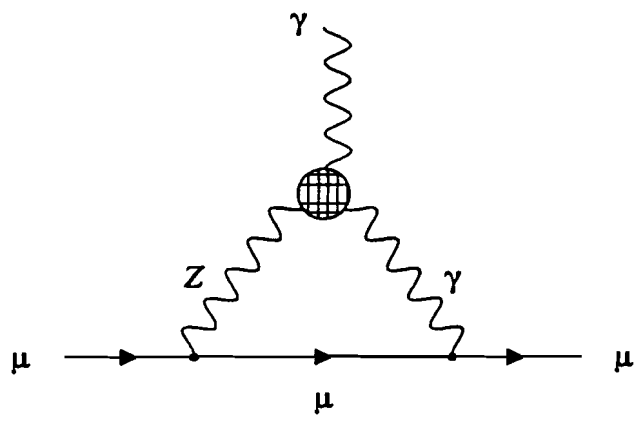

Figure 2.17: Contribution of $Z\gamma\gamma$ vertex to the muon anomalous magnetic moment $(g-2)_\mu$.

In contrast to the low energy limits on $Z\gamma$ interactions, high energy direct

measurements are unambiguous and model-independent by explicit construction. (See section 2.2) Presently, the tightest limits on $ZZ\gamma$ and $Z\gamma\gamma$ couplings are obtained by combining LEP e^+e^- data with Tevatron $p\bar{p}$ data. Figure 2.18 illustrates the complementary nature of the two sets of experiments. The limits from the LEP

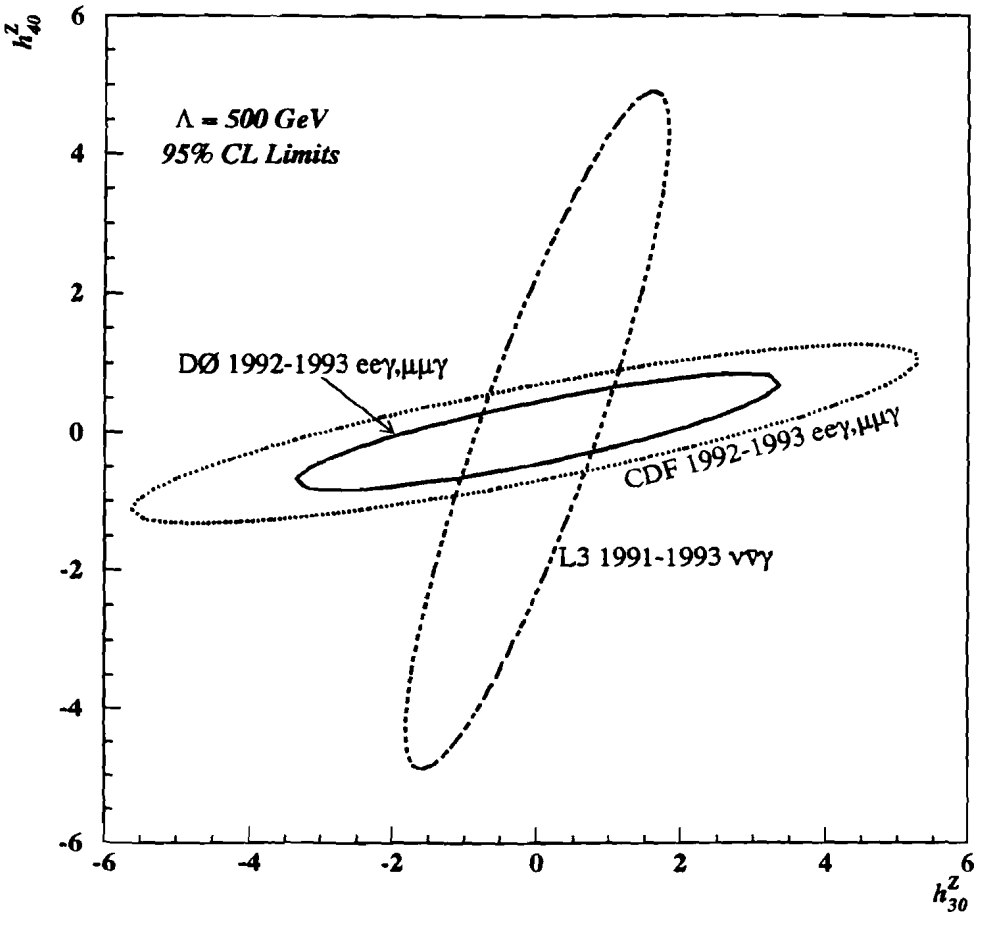

Figure 2.18: Limits on the CP-even couplings h^Z_{30} and h^Z_{40} from previous collider experiments at the Tevatron and LEP.

L3 experiment were obtained by studying $e^+e^- \to \gamma\nu\bar{\nu}$ in 50.8 pb^{-1} of data taken at $\sqrt{s} \approx M_Z$ [52]. The DØ and CDF limits were both obtained by fitting the p_T^γ spectrum for $p\bar{p} \to \ell^+\ell^-\gamma$ in 14 and 20 pb^{-1} of data collected by the respective experiments [53, 54, 55]. Although the Tevatron experiments recorded similar amounts of data, the CDF exclusion contour is less stringent due to the presence of one event with $p_T^\gamma \approx 64$ GeV in the data sample. The different regions excluded by the LEP and Tevatron data are due largely to the different operating energies of the colliders; the Tevatron experiments effectively probe parton energies up to a few hundred GeV. (Recall from section 2.3 that the amplitude terms containing h_3 have different energy dependence than those containing h_4.)

These results provide some guidance in the search for $Z\gamma$ interactions. The aim of this study is to explore the parameter space which has been previously inaccessible due to the rather small datasets. To this end, this work extends the earlier DØ analysis to a data sample approximately six times larger than was previously available.

Chapter 3

Experimental Apparatus

This chapter contains brief descriptions of the various pieces of equipment used in this study. Emphasis is placed on those aspects which are most directly applicable to this analysis. The interested reader is urged to consult the references given here for further details.

3.1 The FNAL Collider Complex

A series of accelerators are used to create and store the protons and antiprotons which eventually end up in the TeVatron [56]. An overview of the FNAL complex is shown in figure 3.1 (courtesy J. Thompson). First, H^+ ions from a plasma source are accelerated to 750 keV at the preaccelerator. A linear accelerator is then used to accelerate the ions to 400 MeV as they are transferred to

the Booster synchrotron. After reaching the Booster, the ions are stripped of their electrons by passing them through a thin carbon foil and the resulting protons are further accelerated to 8 GeV. These protons are then transferred to the Main Ring synchrotron.

The Main Ring is 1000m in radius and is housed in the same tunnel as the Tevatron. Once the protons have been injected into the main ring, they are accelerated and can be subsequently extracted for antiproton production (at 120 GeV), injected into the Tevatron (at 150 GeV) for collider experiments, or can be extracted to fixed target experiments at energies up to 400 GeV. The Main Ring antiproton production cycle is 2.4 seconds in length and is characterized by two periods of heavy losses. The first of these is during injection (from the Booster) at the beginning of the cycle, and the second is the so-called "transition" period, which occurs about 0.3 seconds after injection [56]. Since the Main Ring passes through part of the DØ detector, proton losses can give rise to spurious signals, so events are not recorded during the heavy loss periods. (During normal operation, the Main Ring is continuously used for antiproton production, even while beams are colliding in the Tevatron.) For antiproton production, the Main Ring proton beam is directed to a nickel target, and the resulting antiprotons are selected from the other collision products by a series of magnets. These antiprotons are captured and "cooled" in the Debuncher ring and subsequently transferred to the Accumulator ring for storage and further cooling.

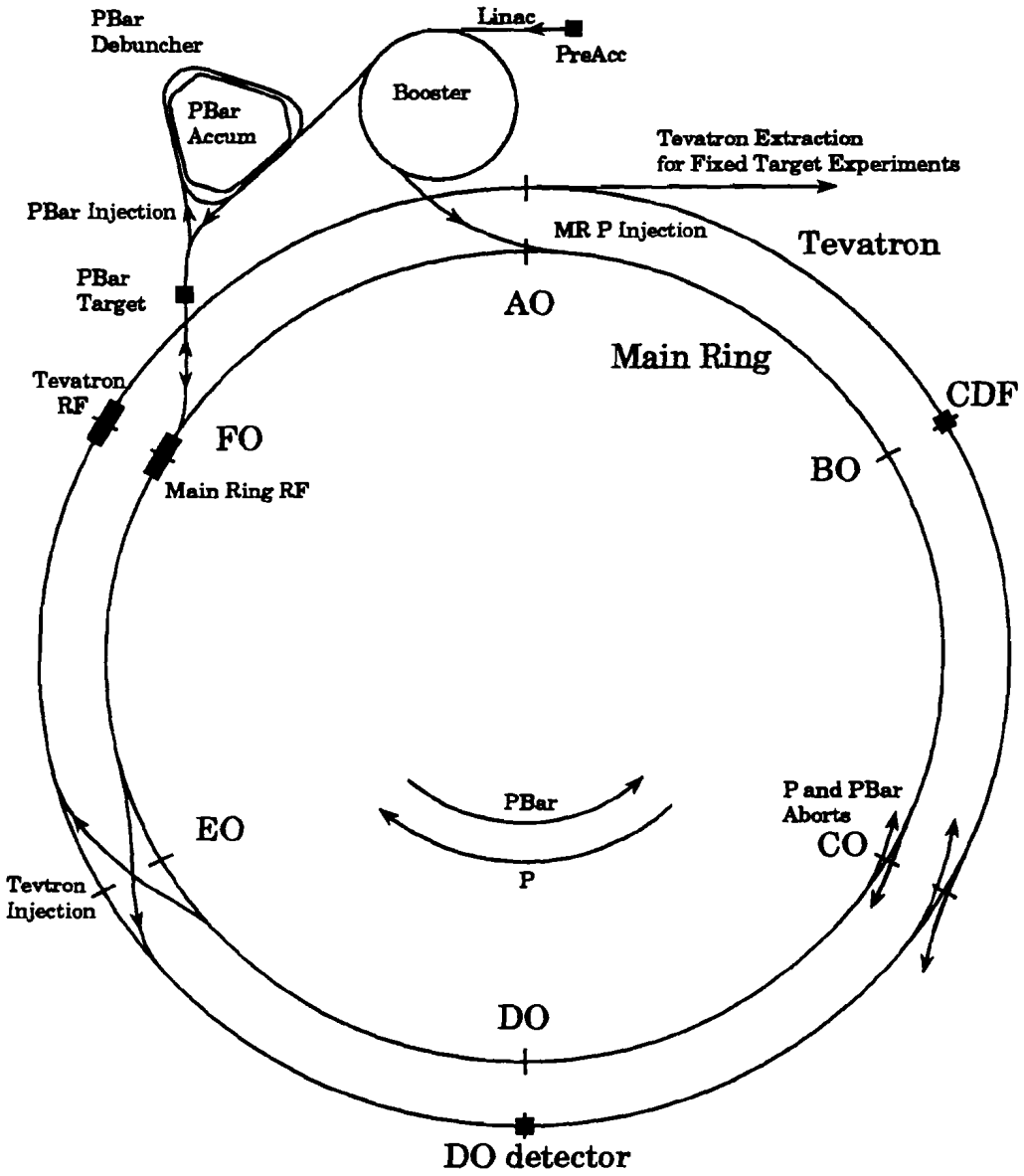

Figure 3.1: Schematic of the FNAL facility (not to scale).

The Tevatron is a superconducting synchrotron which can accelerate proton (or antiproton) beams to energies of 900 GeV. For collider mode operations, proton bunches are transferred from the Main Ring to the Tevatron at an energy of 150 GeV.

Next, antiprotons are transferred from the Accumulator to the Main Ring (in the opposite direction), and are then transferred to the Tevatron after being accelerated to 150 GeV. Both beams are then accelerated concurrently to 900 GeV (flattop), and the luminosity is increased by focusing the beams with superconducting quadrupole magnets located near the BØ and DØ interaction regions. The resulting beam spot has $\sigma_{x,y} \approx 40\mu$m and $\sigma_z \approx 30$ cm.

During the 1993-1995 run ("run 1B"), the Tevatron was operated with six proton and six antiproton bunches spaced by about 3.5 μs. The peak luminosity recorded during run 1B was about 3×10^{31} particles per square centimeter per second, and the total integrated luminosity delivered to the DØ experiment was in excess of 100 pb^{-1}.

3.2 The DØ Detector

The main purpose of the DØ detector is to identify collision products and measure their momentum [65]. As can be seen in figure 3.2 the detector is quite large (about 5500 tons) and is comprised of three main subsystems: the central tracking detectors, the calorimeter, and the muon spectrometers. This section contains descriptions of these systems and a discussion of how the experiment is triggered and data are recorded.

Before discussing the DØ detector further, it is necessary to define the coordinate system and angle conventions used in the experiment. The z axis is coincident with the beamline, with the positive direction defined by the proton direction of travel. The x and y axes are then defined by the horizontal and vertical directions, respectively, where $\hat{x} \times \hat{y} = \hat{z}$. The azimuthal angle ϕ is measured with respect to the $+x$ direction, and the polar angle θ is measured with respect to the $+z$ direction. Another useful quantity is pseudorapidity, η, which is defined by $\eta = -\ln[\tan(\theta/2)]$. In the massless limit, the pseudorapidity approaches the true rapidity of a particle:

$$\eta \approx \frac{1}{2} \ln \left(\frac{E + p_z}{E - p_z} \right)$$

for $E \gg m$, where m is the mass of the particle. Often it is convenient to express polar angles in terms of "detector pseudorapidity", denoted η_{det}, which is computed with respect to $z = 0$. In practice, the interaction point is characterized by a Gaussian centered at $z \approx 0$ with $\sigma_z \approx 30$ cm, so η and η_{det} differ slightly for a given

particle.

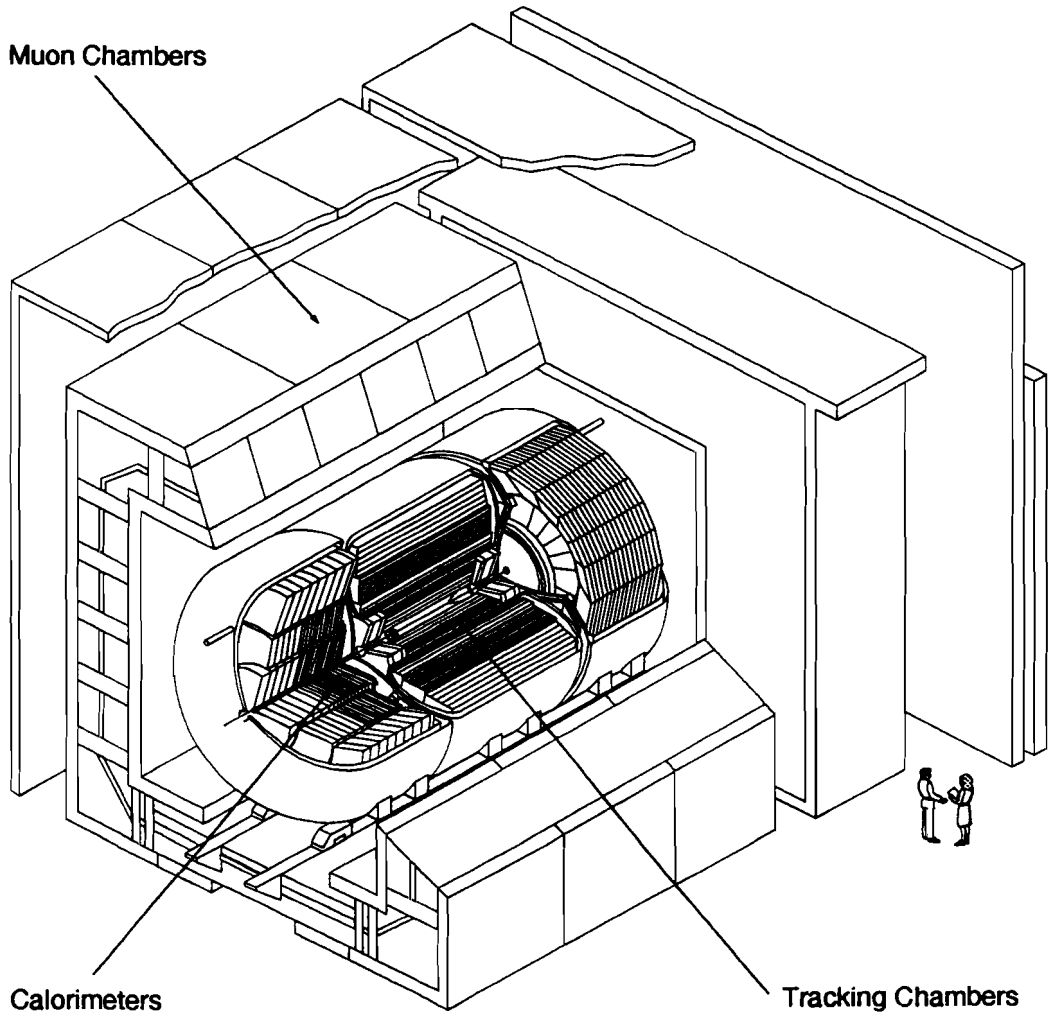

Figure 3.2: Isometric cutaway view of the DØ detector.

3.2.1 Central Detector

The purpose of the central detector is to non-destructively measure the directions of the particles emanating from the interaction point. Since there is no magnetic field in the tracking volume, particle momenta (energies) are measured using the calorimeter. The central detector consists of a vertex drift chamber (VTX), a transition radiation detector (TRD), central drift chambers (CDC), forward drift chambers (FDC), and the forward level-Ø (LØ) counters. For efficiency reasons, the VTX and TRD subdetectors are not used in this analysis and are not discussed here. Further description of the LØ system can be found in section 3.2.4.

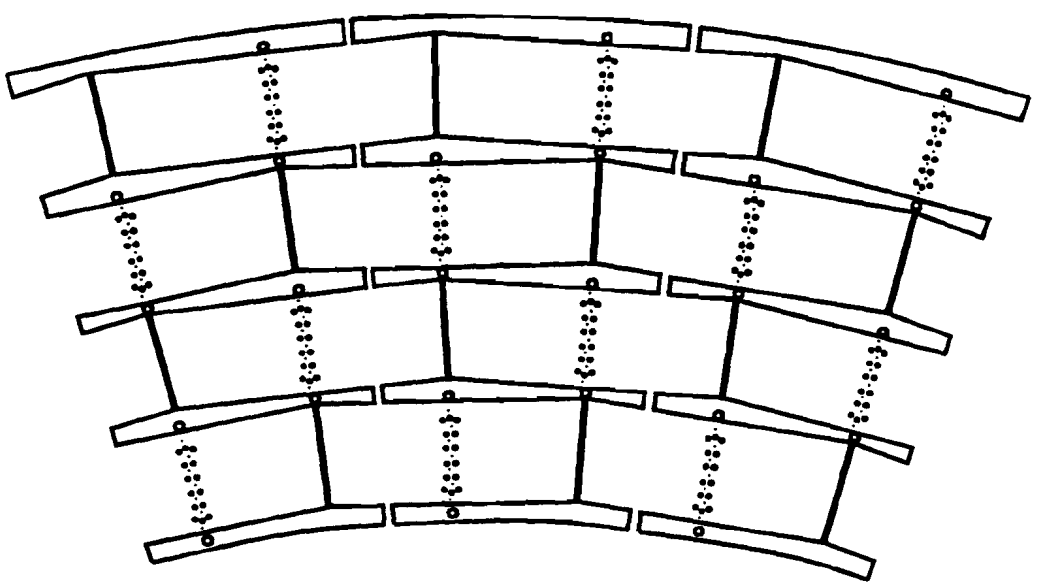

Figure 3.3: End view of three CDC modules. Sense wires are indicated by small dots, guard (field shape) wires by large dots, and delay lines by open circles.

The CDC provides coverage for $|\eta| < 1.2$ and is in the shape of a cylindrical shell [65]. As is shown in figures 3.3 and 3.5, it is made up of four layers of drift cells which occupy the region between 49.5cm and 74.5cm from the beamline. Each layer consists of 32 cells which contain seven sense wires (anodes), and two delay lines. The gas is a combination of argon, methane, carbon dioxide, and a small amount of water vapor. During operation, the sense wires are held at a potential of about 1.5 kV, so electrons liberated from gas molecules by the passage of a charged particle drift toward the anodes. The electric field increases dramatically in the vicinity of the anodes [64], and an avalanche occurs when the electrons reach this region. The azimuthal distance between the initial ionization trail and the sense wire is inferred from the time of drift prior to the avalanche. The z coordinate of the original ionization trail is measured using the signal induced on the delay lines by the avalanches on nearby anodes. Timing information is then used to infer the initial signal position along the delay line.

The FDC consists of two sets of drift chambers located at the ends of the CDC which provide tracking coverage for $1.4 < |\eta| < 3.1$ [57, 65]. Figure 3.4 shows one such set of chambers. Each FDC consists of a Φ chamber sandwiched between two Θ chambers. The Θ chambers are divided into quadrants, and each quadrant into six box-shaped cells. These Θ cells contain eight azimuthal sense wires along the z direction, so electron drift is approximately in the θ direction. For redundancy, each Θ cell is equipped with one delay line to measure ϕ. The Φ chambers are

divided azimuthally into 36 segments, each of which contains 16 radial sense wires in the z direction. The direction of drift is therefore approximately azimuthal in the Φ chambers. All FDC chambers are filled with a gas mixture similar to that used in the CDC.

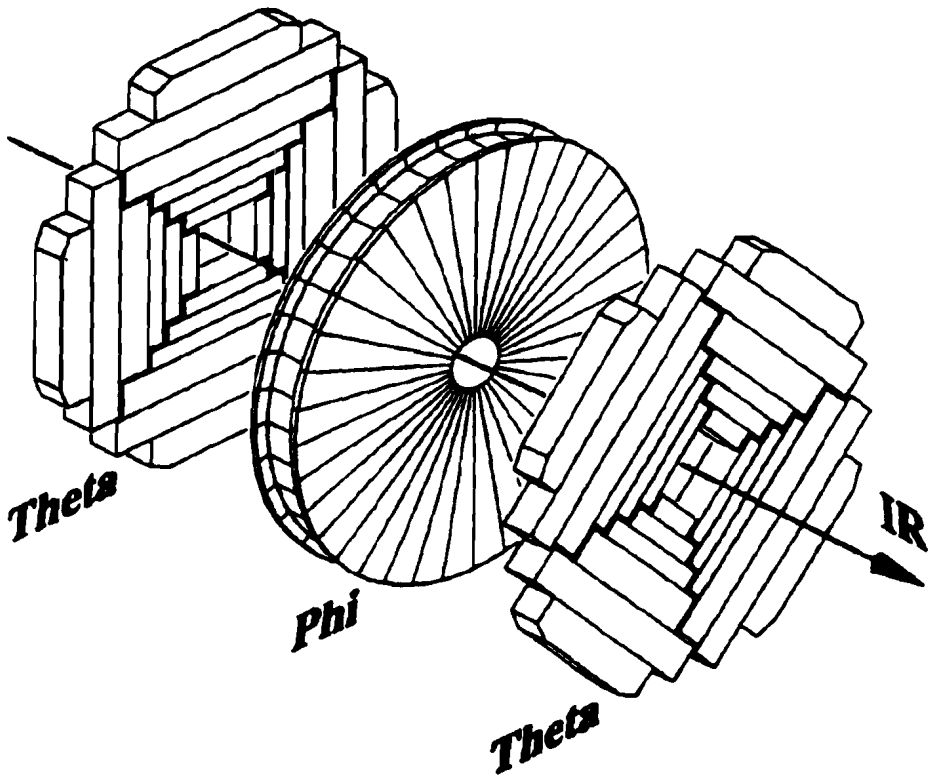

Figure 3.4: Exploded isometric view of one half of the FDC tracking system.

3.2.2 Calorimetry

Particle energies are measured in the DØ detector using a liquid argon sampling calorimeter system which is divided into three modules contained in separate

cryostats: the Central Calorimeter (CC), the North End Calorimeter (ECN), and the South End Calorimeter (ECS). In each module, a series of absorber plates cause incident particles to shower, and the resulting shower particles deposit ionization (energy) in the liquid argon gaps between the absorber plates. A voltage gradient causes the the resulting charges to drift and induce a signal on pickup boards located in the gaps. Signals from several boards are then ganged to form readout cells. Figure 3.5 shows a side view of the calorimeter and central detectors. Also indicated is the readout cell segmentation. The calorimeter modules are further subdivided by depth into longitudinal modules which are described below.

For the purposes of this analysis, the most important parts of the calorimeter system are the "electromagnetic" calorimeters (EM), since electron and photon showers are mainly contained in these compartments. The CCEM covers the region $|\eta_{\rm det}| < 1.1$, and the ECEM modules provide coverage for $1.5 < |\eta_{\rm det}| < 2.5$.

The CCEM modules use depleted uranium as an absorber medium and sample showers at the four intervals after approximately 2.0, 4.0, 10.8, and 20.6 radiation lengths of absorber. The transverse segmentation of each layer is $\Delta\eta \times \Delta\phi \approx 0.1 \times 0.1$ except in the third layer, which has 0.05×0.05 segmentation. The finer segmentation in the third layer is motivated by shower position resolution, since electron/photon showers are of maximum transverse width ("shower maximum") in the third layer. The CCEM is constructed using 32 azimuthal segments containing two EM towers

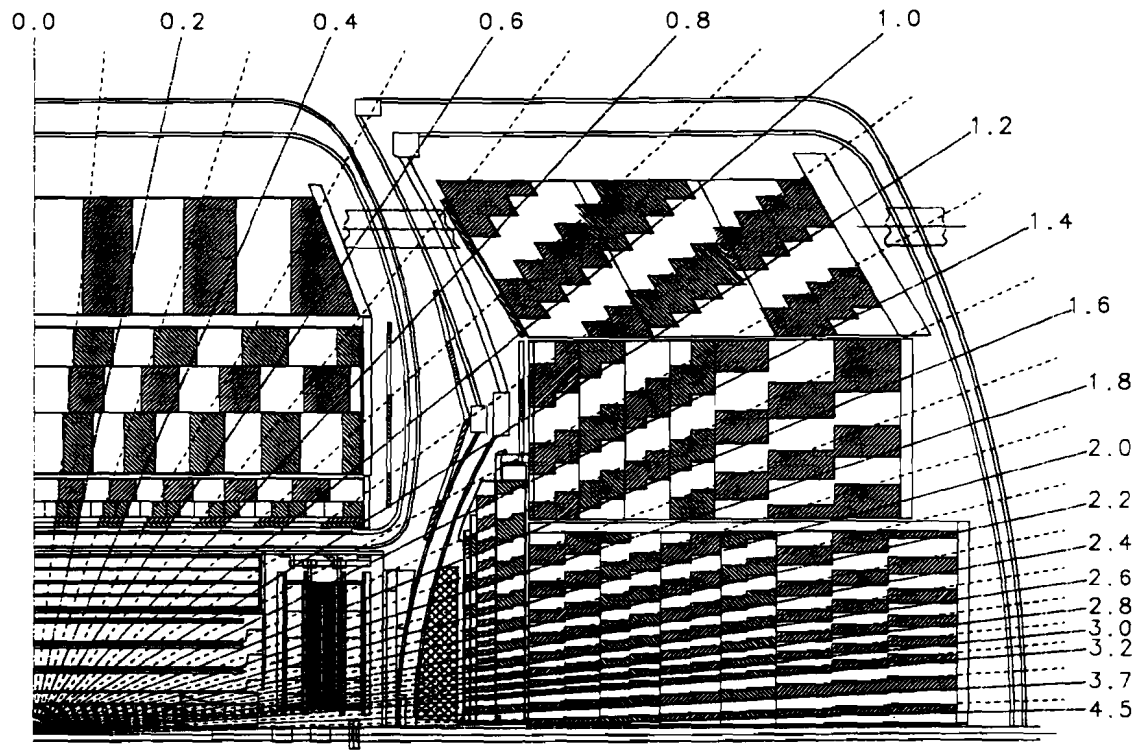

Figure 3.5: Side view of one quadrant of the calorimeter and central detector. The lines of constant pseudorapidity intervals with respect to $z = 0$.

apiece, and there is a small uninstrumented crack between each pair of these ϕ modules. Showers originating from particles which enter the CCEM near the ϕ cracks are likely to be distorted, which makes particle identification difficult in this region. Therefore, electron or photon showers reconstructed near the ϕ cracks are discarded during offline analysis.

The ECEM is similar to the CCEM. Showers are sampled after approximately 0.3, 2.9, 11.8, and 21.1 radiation lengths of uranium absorber. The ECEM transverse segmentation is identical to the CCEM, except that the third layer segmentation is

0.1×0.1 for $|\eta_{\text{det}}| > 2.5$. For this reason, electron and photon candidates are restricted to $1.5 < |\eta_{\text{det}}| < 2.5$ in the EC. In contrast to the CC, the EC is constructed such that there are no intermodule ϕ cracks, so no azimuthal requirement is placed on electromagnetic showers in the EC.

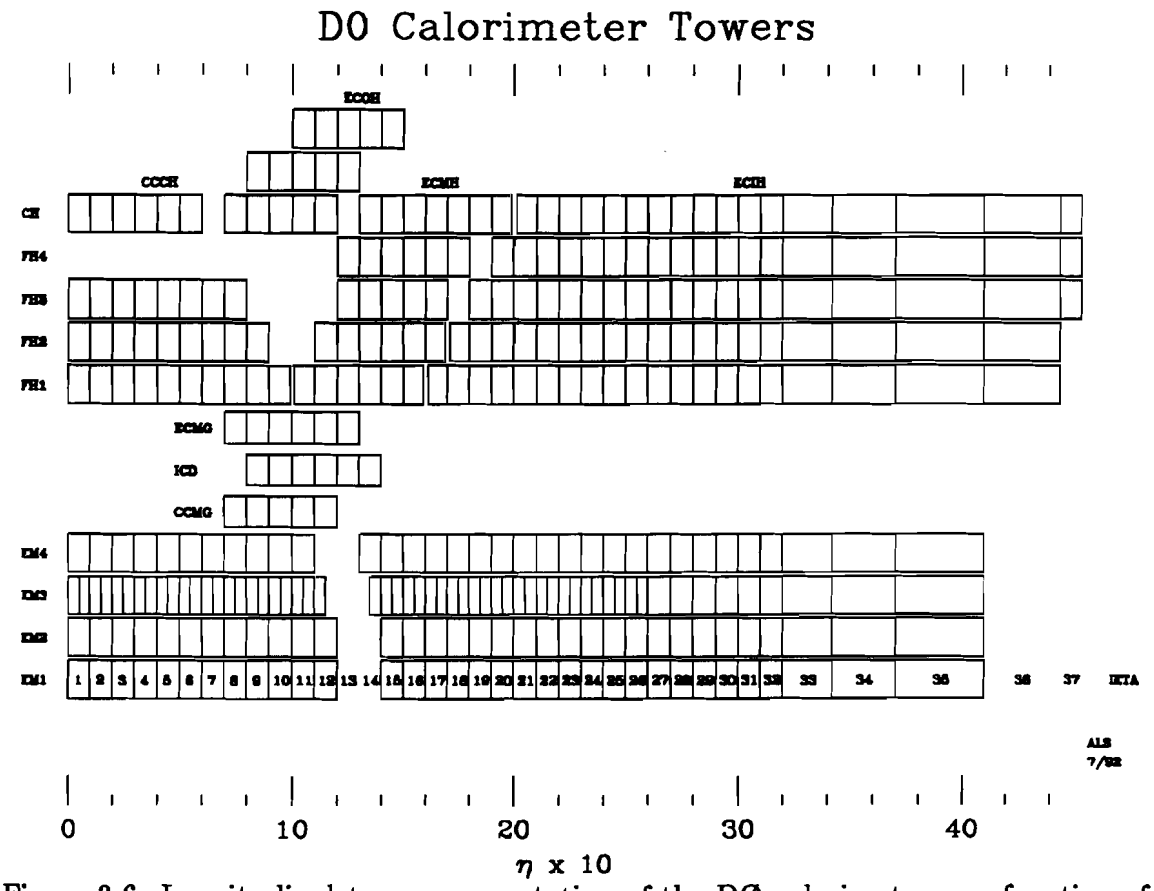

Figure 3.6: Longitudinal tower segmentation of the DØ calorimeter as a function of pseudorapidity.

The layers immediately outside the CCEM and ECEM are the "Fine Hadronic" layers (FH) which contain uranium-nobium alloy absorbers and are used to sample

hadronic showers. The outermost calorimeter layers use copper (CC) or steel (EC) absorbers and are known as the 'Coarse Hadronic" (CH) sections. The transverse segmentation for both the FH and CH sections is approximately 0.1×0.1. Figure 3.6 shows a schematic representation of the calorimeter segmentation as a function of depth and $\eta_{\rm det}$.

It should also be noted that the main ring beam pipe passes through the CH section of the CC. (c.f. figures 3.2 and 3.5) This creates problems in jet and missing E_T reconstruction, but has minimal consequences for this analysis since only the EM calorimeters are used.

3.2.3 Muon Tracking

The calorimeter is of sufficient thickness that only muons are likely to penetrate the outermost layers. The momenta of such muons are measured using a spectrometer consisting of three layers of drift tubes situated on either side of toroidal magnets (see figure 3.2). The muon system is not used for this analysis, and the interested reader is referred to the literature for details [65].

3.2.4 Trigger and Data Acquisition

In 6×6 operation, the bunch crossing rate is about 286kHz, so it is impractical to read out the entire detector for every beam crossing. Additionally, many physics processes of interest have very small cross sections relative to the total $p\bar{p} \rightarrow X$

cross section, and an excessively large number of such "zero bias" events would need to be collected in order to study these processes (c.f. figure 1.4) To overcome these obstacles, the readout system is "triggered" and events are recorded only if they satisfy certain topological or kinematic criteria, e.g. contain a high-E_T jet. This section gives abbreviated descriptions of the DØ trigger and data acquisition systems.

Beam Vetos

As was mentioned previously, the Main Ring passes through the muon system and outer hadronic calorimeter, and the Main Ring is continually used for antiproton production during normal collider operation. If protons are lost from the Main Ring, they can give spurious signals in the detector. Therefore, events are not recorded during periods which are expected to be especially noisy. In this analysis, no attempt is made to infer the presence of neutrinos by missing transverse energy, nor is jet reconstruction crucial, so events are only discarded which occur during the periods of maximal Main Ring losses. Specifically, only events which occur in the `MICROBLANK` window *within* the 400ms `MRBS_LOSS` window after Main Ring proton injection are rejected. (The 1.6μs `MICROBLANK` gate occurs every 21μs and is consistent with the passage of Main Ring protons through the DØ detector.) This veto is known as "`Max_Live`", since it is the least stringent veto used by the experiment. The total dead time incurred by the `Max_Live` veto is about 2%.

Level Ø

The LØ detector consists of scintillator arrays mounted between the FDC and EC [58]. These detectors are used to quickly signal the presence of an inelastic collision and as luminosity monitors. The luminosity is estimated using LØ hit rates, measured values of the total inelastic cross section, and acceptance estimates from Monte Carlo studies [76]. A systematic normalization uncertainty of 5.4% is assigned to the luminosity determination, which is based on differences between different Monte Carlo calculations and zero-bias data. Additionally, the timing information from the LØ counters is used to determine the interaction z position for subsequent trigger levels.

Level 1

The L1 trigger [60] is based in hardware in order to minimize the decision time as much as possible. For this study, the relevant trigger was based on calorimeter information and required two 0.2×0.2 EM towers with $E_T > 7$ GeV (the so-called em_2_med trigger). This trigger was not prescaled during data collection, which means that no events were discarded for the purposes of bandwidth management.

Level 1.5

The rather low E_T thresholds used at L1 are motivated by the E_T resolution of the L1 calorimeter trigger[1] and the desire for full efficiency at $E_T \approx 20$ GeV. Since the background rate for electrons grows dramatically as E_T thresholds are lowered, it is advantageous improve resolutions to reject background. This one one of the reasons for the introduction of the L1.5 calorimeter trigger during run 1B [61]. The L1.5 trigger is DSP-based and improves energy resolution by examining the energy in towers neighboring the L1 EM towers. Additionally, energy sums are computed from adjacent hadronic towers, and the ratio E_{EM}/E is used for further background rejection. For this analysis, events passing the em_2_med L1 trigger were required to have at least one L1.5 electron candidate with $E_T > 12$ GeV and $E_{\mathrm{EM}}/E > 0.85$.

Level 2

The L2 trigger system is software-based and consists of a farm of 48 VAX nodes. If an event satisfies the LØ, L1, and L1.5 triggers, the analog data at the detector front ends are digitized and sent to an available L2 node. Since time constraints are not as stringent at L2 relative to L1, more sophisticated algorithms can be used to reject background events. Electron candidates are reconstructed beginning with the original L1 EM tower. Neighboring towers are added to include

[1]The energy deposited by electrons entering the calorimeter near tower boundaries can be shared between towers, which results in decreased trigger efficiency near the tower boundaries.

portions of the shower which cross tower boundaries. These candidates are then subjected to longitudinal and transverse shower shape cuts which were tuned to give good efficiency for test beam electrons [62]. For example, one of the longitudinal shape criteria is based on the ratio $E_{\mathrm{EM3}}/E_{\mathrm{EM}}$, and is useful in rejecting electron candidates due to "hot" calorimeter cells. Additionally, an energy isolation requirement can be placed on electrons which places limits on the allowable amount of energy in the hadronic portion of the calorimeter in the vicinity of the electron. This is similar to the offline isolation requirement discussed in section 4.5.

All events in this analysis are required to satisfy the `em2_eis2_hi` L2 software filter. This filter required two L2 electron candidates with $E_T > 20$ GeV which satisfied electron shower shape and isolation cuts. After accounting for dead time, the estimated integrated luminosity for which these data were collected was 89 ± 4.8 pb^{-1}.

A schematic of the DØ data acquisition system is shown in figure 3.7 [65, 63]. Signals from the subdetector systems are organized into seven readout sections consisting of 80 VME crates. The data from the readout sections and the LØ and L1 triggers are read out using eight high-speed data cables. Upon receipt of a valid L1 trigger, a supervisor computer is used to determine which L2 node receives the event. Events which pass L2 are then sent to the host machine where they are temporarily stored on disk. The resulting raw event files are copied to 8mm magnetic tape for permanent storage.

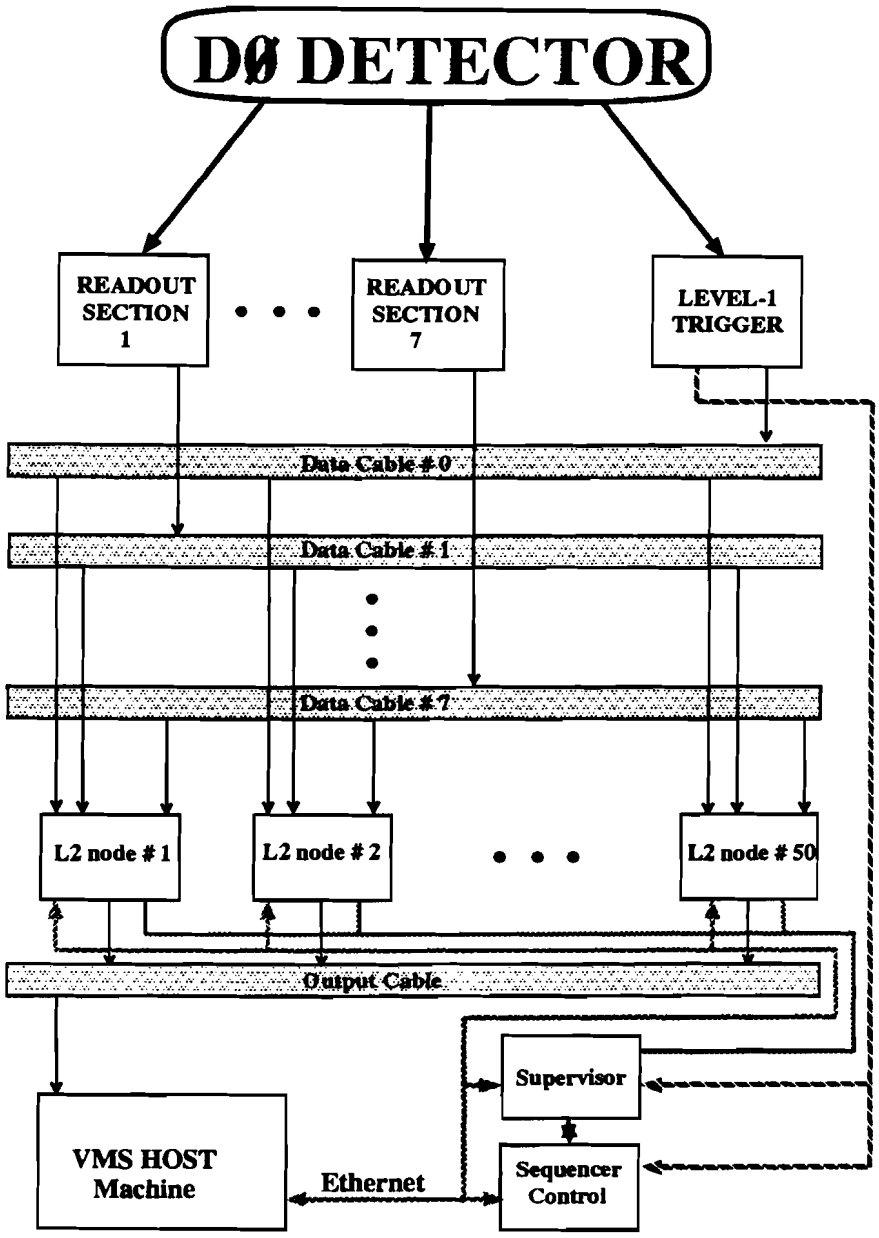

Figure 3.7: Schematic of data aquisition at DØ.

3.3 Data Reconstruction

The raw data are reconstructed on a farm of SGI and IBM workstations. The number of nodes in the farm was dependent on demand and consisted of as

many as 96 nodes during run 1B. Two files types are output from the reconstruction farm: "STA" and "DST". The STA files range from 600-1000kB per event and contain enough important information that events can be reconstructed from STA files themselves. DST files contain summary event data which are used in physics analyses such as reconstructed electrons, photons, muons, and jets. However, the size of the run 1B data sample necessitated a change to a third file type, the μDST, which contained the minimum amount of information needed to perform analyses. All events from run 1B are placed on disks in μDST format, and these files are further filtered by analysis groups to make the size of the dataset manageable.

Chapter 4

Event Reconstruction and Particle Identification

The raw information recorded by the detector is in the form of digitized pulse heights, widths and times, which are not immediately useful to humans. It is the job of reconstruction software to transform these digitizations into objects which are recognizable as signatures of high-energy particles. In this experiment, this task is done by a program called DØRECO. This chapter describes how various pieces of DØRECO reconstruct the event and the how additional criteria are applied to enhance particle identification.

4.1 Tracking

The trail of ionization deposited by a charged particle in the drift chambers is reconstructed as a track using the drift times of the sense wire pulses to infer how far the particle passed from the wire. The resulting "hits" are used to form track segments which are subsequently linked to form a track. For each track, directional information is specified by five parameters: the coordinates of a reference point (x_0, y_0, z_0), the polar angle θ and the azimuthal angle ϕ. It should also be mentioned that track and hit reconstruction is only performed within rather wide "roads" defined by calorimeter clusters and the event vertex in the forward region. All tracks and hits are reconstructed in the central region. These choices were dictated by computational considerations.

In addition to providing directional information, the amount of ionization along the track (dE/dx) provides an additional handle for background rejection. Since particles in a typical event are highly relativistic, it is difficult to distinguish between different types of particles, e.g. π, K, p, on the basis of ionization. However, it is possible to distinguish between tracks due to single particles and tracks due to overlapping particles. For example, an electron track should have roughly half the ionization as one due to a $\gamma \rightarrow e^+e^-$ conversion.[1] However, for reasons of efficiency, dE/dx information is not used in this analysis.

[1] Since the DØ tracking system is nonmagnetic, particles of opposite charge can overlap such that they are not resolved into two separate tracks.

4.2 Vertexing

Once the tracks in an event have been reconstructed, the next step is to determine the interaction point(s) from which they originated. The method employed by DØRECO utilizes histograms of track z-intercepts to determine the z position of the interaction point as is illustrated in figure 4.1. Each CDC track is projected back to the beamline (at $x \approx y \approx 0$) and the interaction vertices are identified as peaks in the distribution of z-intercepts. The peak associated with the "primary" or "hard scatter" vertex is assigned to the peak with the largest number of tracks in the event.[2] This method typically achieves vertex z resolutions of 1-2 cm for low-multiplicity events. Unfortunately, the histogram vertexing method becomes unreliable when the number of interactions per crossing is large (high luminosity) or the interesting (high-p_T) interaction happens to have a lower total charged track mulitiplicity than the other minimum bias interaction(s) in the event. Thus, a correction is introduced which is based on the angular information associated with physics objects in the event. Discussion of this correction is deferred until after the reconstruction of electrons has been described.

Once the vertices in an event have been identified, the calorimeter-based objects can be reconstructed. These include jets, electrons, and photons. Jets are reconstructed as collections of cells in the calorimeter; no attempt is made at the

[2]As used here, "primary" and "secondary" refer to the multiplicities associated with vertices; this has nothing to do with decays of long-lived particles.

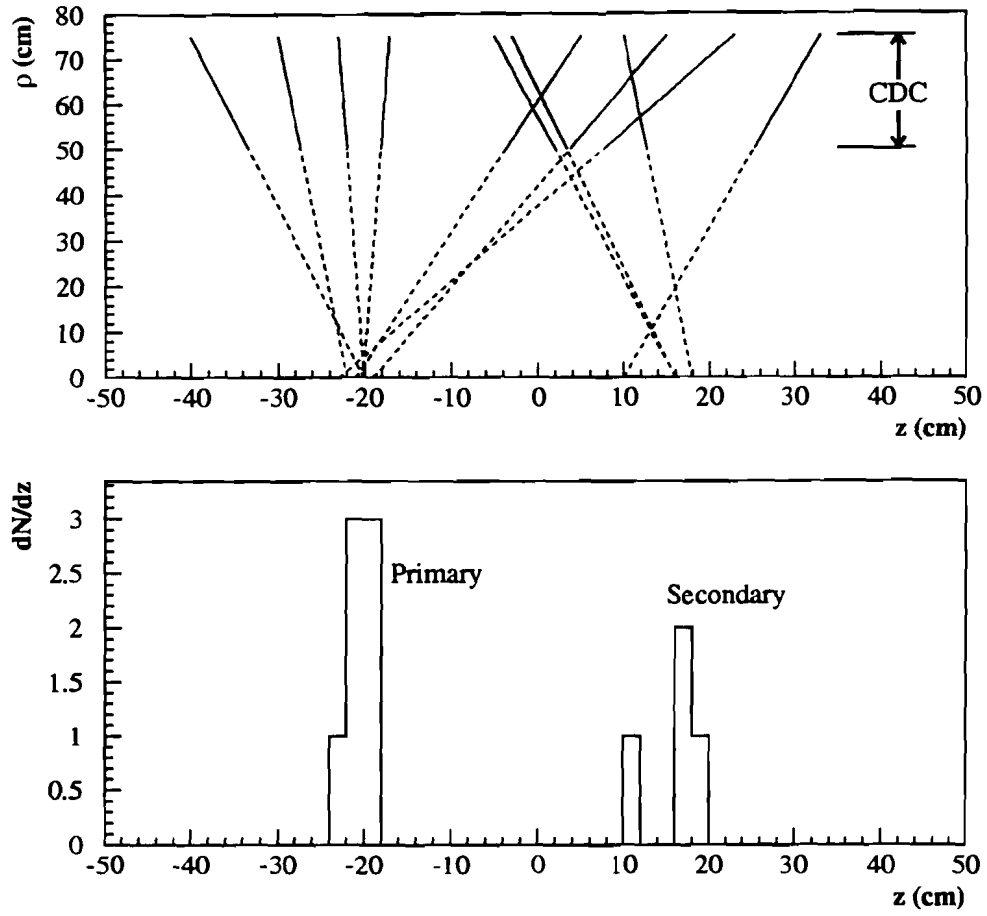

Figure 4.1: Vertex determination by histogram method. Top: projections of tracks to the beamline. (View is integrated over all azimuthal angles ϕ.) Bottom: Resulting distribution of z-intercepts from which vertices are determined.

reconstruction level to discern the physical origin of these showers. Showers which are concentrated in the electromagnetic portion of the calorimeter are likely to be due to electrons or photons and are classified accordingly. The sections below detail how these objects are reconstructed from the raw data and which criteria are used

to discern their identities.

4.3 Jets

The portion of DØRECO which is responsible for jet reconstruction is called CAJETS. Although several algorithms can be used for jet reconstruction, the most common is the "cone algorithm" and is the one discussed here. The use of the cone algorithm requires one to choose the cone size $\mathcal{R}$, where $\mathcal{R} = \sqrt{\Delta\eta^2 + \Delta\phi^2}$ describes the maximum transverse radius of the jet. Most (but not all) analyses use jets reconstructed with $\mathcal{R} = 0.5$. The reconstruction proceeds as follows: The transverse energy is calculated for all $\Delta\eta \times \Delta\phi = 0.1 \times 0.1$ towers. These towers are sorted in order of decreasing E_T. Beginning with the highest E_T tower, clusters are formed by adding towers within $\mathcal{R}$ of the highest energy tower. The process is repeated for the remaining calorimeter towers. Once this is complete, the center of each jet is calculated by performing an E_T-weighted sum of the tower (η, ϕ) positions. The whole clustering process is repeated using the jet centers as cluster seeds until the jet centers do not change appreciably from one iteration to the next.

Criteria exist which can be used to distinguish jets from instrumental backgrounds. Since jets are not used for this analysis, these are not discussed here, and the interested reader is referred to the existing GOOD_JET routine [66] which

describes cuts designed to eliminate jets due to "hot" cells or regions in the calorimeter.

4.4 Electrons and Photons

Since the the showers from electrons and photons are expected to be very similar [64], the reconstruction of these objects proceeds along the same lines. The piece of code responsible for this task is called CAPHEL at DØ. In contrast to the cone-based jets described previously, electron and photon calorimeter clusters are reconstructed using a so-called "nearest neighbor" algorithm. First, the energies in the four electromagnetic (EM) and the first ("fine") hadronic layers are summed to create EM towers (in the CATE bank). Next, beginning with the towers of highest energy, clusters are created by adding physically adjacent towers with $E > 50$ MeV to the cluster. After all possible clusters have been identified, those which *fail* the following criteria are dropped from further consideration:

- Total energy above 1.5 GeV; $E_{\mathrm{EM}} + E_{\mathrm{FH1}} > 1.5$ GeV.
- Total transverse energy above 1.5 GeV; $E_{T,\mathrm{EM}} + E_{T,\mathrm{FH1}} > 1.5$ GeV.
- Electromagnetic energy fraction greater than 90%; $E_{\mathrm{EM}}/E_{\mathrm{EM+FH1}} > 0.90$.
- Fraction of energy outside the tower of maximum energy less than 60%; $E_{\mathrm{out}} < 0.6\,E$, where E_{out} is the energy in the cluster not in the highest energy

tower. This is equivalent to the requirement that 40% of the cluster energy be contained in the highest energy tower.

The centroid positions of the remaining candidates are then calculated using a log-energy weighting technique in EM3 to account for the transverse distribution of energy within the shower. (Recall that transverse sampling is finest in EM3) Small corrections to the centroid position are made which account for the entry angle of the electron into the calorimeter[67]. The reconstructed centroid has a resolution of about 2mm.

At this point, a distinction between electrons and photons is made. Tracking "roads" of width $(\Delta\theta \times \Delta\phi) = \pm 0.1 \times \pm 0.1$ are first defined using the cluster centroid positions and the primary vertex position, then a search is performed for tracks within the road. If one or more tracks are found, the object is classified as an electron. Otherwise, it is classified as a photon. (In the language common to DØ, these objects are sometimes called PELC'S and PPHO'S, respectively, in reference to the banks which contain the reconstructed object information.) Clearly, this distinction is problematic if the vertex is incorrectly identified and the tracking roads are miscalculated. A more robust method which does not rely on the vertex position was developed to overcome this situation and is described in section 4.8

The emphasis in DØRECO is toward maximum efficiency in reconstructing electrons and photons; the task of further separating signal from background is

accomplished in the final analysis steps. To do this, additional criteria are used in the final selection of candidates which retain most genuine electrons while rejecting as much background as possible. The first two such criteria are based on calorimeter information and exploit the differences between electron (or photon) showers and showers originating from hadronic jets.

4.5 Shower Isolation

Since production of π^0/η particles which are spatially isolated from other hadrons is relatively rare[3], an *isolation* requirement can reduce this source of background. Since electromagnetic showers are usually contained in a cone of radius $\mathcal{R} = 0.2$, a calorimetric isolation variable I can be defined as

$$\mathcal{I} = \frac{E(0.4) - E(0.2)_{\mathrm{EM}}}{E(0.2)_{\mathrm{EM}}}$$

where $E(0.4)$ denotes the total energy in a cone of radius 0.4 around the cluster center and $E(0.2)_{\mathrm{EM}}$ denotes the electromagnetic energy in a core cone of radius 0.2. Small values of $\mathcal{I}$ are indicative of a relatively quiet environment in the vicinity of the shower. This is illustrated in figure 4.2, which shows the distribution of $\mathcal{I}$ for both $Z \rightarrow ee$ decay candidates and electron candidates from events collected with rather unrestrictive ("loose") multijet triggers. The former sample is dominated by

[3]In the momentum range of interest, the photons from $\pi^0 \rightarrow \gamma\gamma$ have a small enough opening angle in the lab frame that they are unresolved in the calorimeter. See appendix B for a discussion of background sources for electrons and photons.

signal, and the latter is dominated by background. For this analysis, a requirement of $\mathcal{I} < 0.10$ is imposed on electron and photon candidates. This cut rejects the tail of the background distribution while retaining most of the signal.

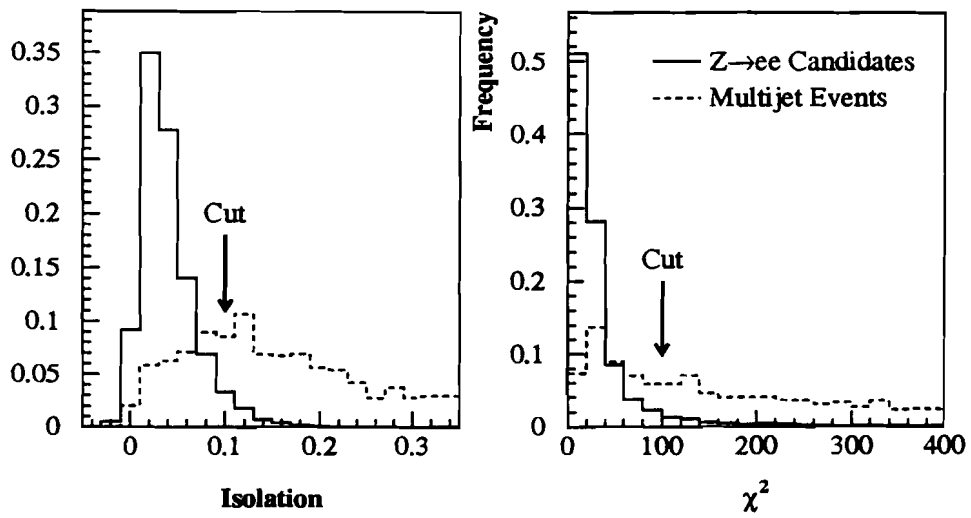

Figure 4.2: Isolation and χ^2 distributions for $Z \rightarrow ee$ candidates and electrons identified in multijet-triggered data.

4.6 Shower Shape

The shape of the shower within the core cone can also be exploited for background rejection purposes. The approach used at DØ is based on a covariance matrix of shower parameters [68]. Given a sample of electrons, the matrix element

describing the correlation between observable quantities x_i and x_j is given by

$$M_{ij} = \langle\ (x_i - \langle x_i \rangle)(x_j - \langle x_j \rangle)\ \rangle = \langle x_i x_j \rangle - \langle x_i \rangle \langle x_j \rangle$$

where the brackets denote averages taken over the whole sample. In the DØ implementation of this technique, 41 observables are used: the shower energy fractions in layers EM1, EM2, and EM4, the energy fractions in the 6×6 array (in $\eta \times \phi$) of cells in EM3 surrounding the hottest cell, the logarithm of the shower energy, and the vertex z position. The covariance matrix M is computed from Monte Carlo samples of simulated electron showers at different energies, angles, and vertex positions. In order to distinguish electrons from background, a χ^2 variable is constructed which describes the deviation of a given shower from the "average" shower shape expected for electrons:

$$\chi^2 = \sum_{i,j} (x_i - \langle x_i \rangle) H_{ij} (x_j - \langle x_j \rangle)$$

where the "H-Matrix" is given by $H = M^{-1}$. Showers which match the shape of Monte Carlo electrons result in small values of χ^2. An example of this is shown in figure 4.2. Electron candidates from $Z \rightarrow ee$ events tend to populate the small-χ^2 region of the distribution, while candidates collected from multijet triggers are distributed over a relatively large range of χ^2. For this analysis, electron candidates are required to have $\chi^2 < 100$ in the CC and $\chi^2 < 200$ in the EC. (The looser cut for EC electrons is motivated by the desire to obtain similar efficiencies for both central and forward electrons; the χ^2 distribution for electrons in the EC has a longer tail

than the CC distribution.)

4.7 Track Matching

Electron backgrounds can also be reduced through the use of tracking information. The ionization trail in the drift chamber from a genuine electron is expected to be aligned with the shower produced in the calorimeter, so gains in background rejection can be expected if more stringent track-cluster matching criteria are used instead of the road based method employed by DØRECO for electron/photon discrimination. To quantify how well a track matches a cluster, the track is extrapolated into the EM3 layer of the calorimeter and the distance between the resulting projection and the cluster centroid position is calculated. Figure 4.3 illustrates the resolution achieved in track projection-cluster matching for $Z \rightarrow ee$ candidates in both the longitudinal (θ) and transverse (ϕ) directions. For central electrons, the track-cluster difference distribution has a longitudinal width of about 1.7 cm, and a transverse width of about 0.3 cm. For electrons in the forward region, these resolutions are about 0.7 and 0.3 cm, respectively. Given these track-cluster matching resolutions, it is possible to construct a discriminant similar to the H-Matrix χ^2 discussed previously. This variable is called "track match significance", and is defined by

$$s_{\text{track}} = \sqrt{\frac{(\Delta x_L)^2}{\sigma^2_{\Delta x_L}} + \frac{(\Delta x_T)^2}{\sigma^2_{\Delta x_T}}}$$

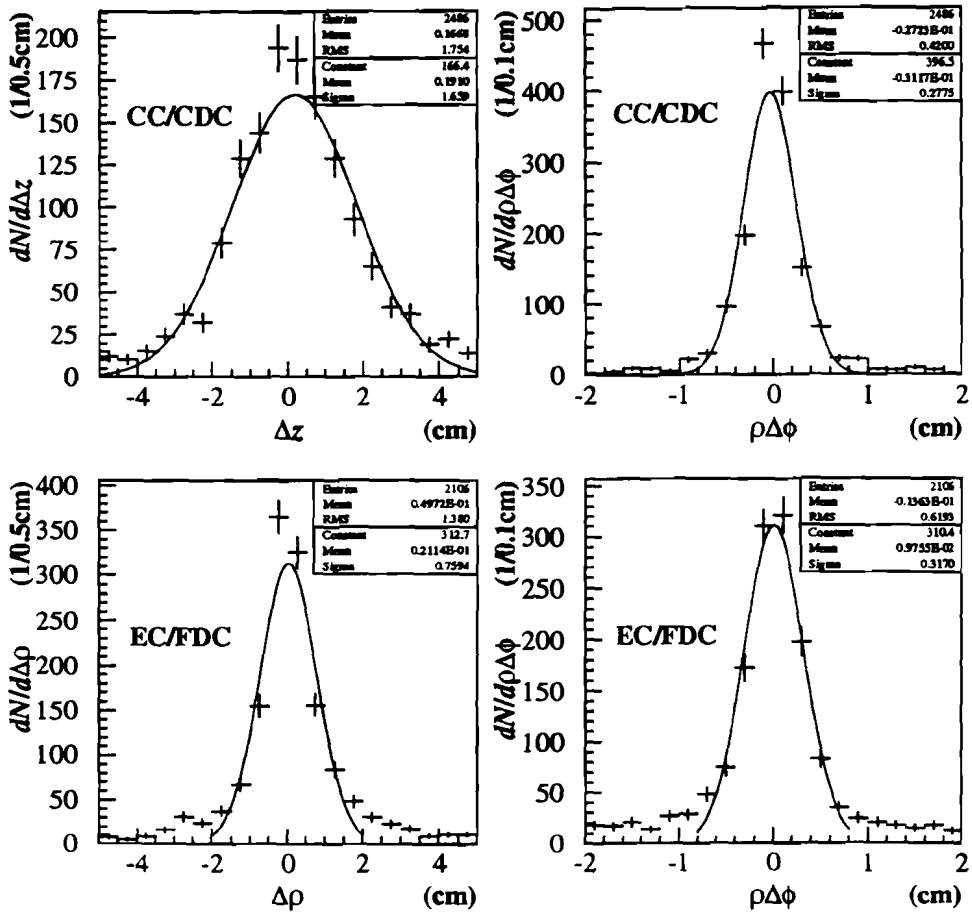

Figure 4.3: Differences in cluster and projected track positions for $Z \rightarrow ee$ candidates. Only candidates with $s_{\mathrm{trk}} < 30$ are shown.

where Δx_L and Δx_T are the differences in the longitudinal and transverse directions of the cluster-track projection, respectively. The variables $\sigma_{\Delta x_L}$ and $\sigma_{\Delta x_T}$ are the resolutions obtained from the distributions in figure 4.3. To clarify this point further, an illustration of the physical meaning of the track match significance is shown in

figure 4.4. Track projections which fall within the indicated significance ellipse projected onto the surface of the EM3 layer are considered good matches.

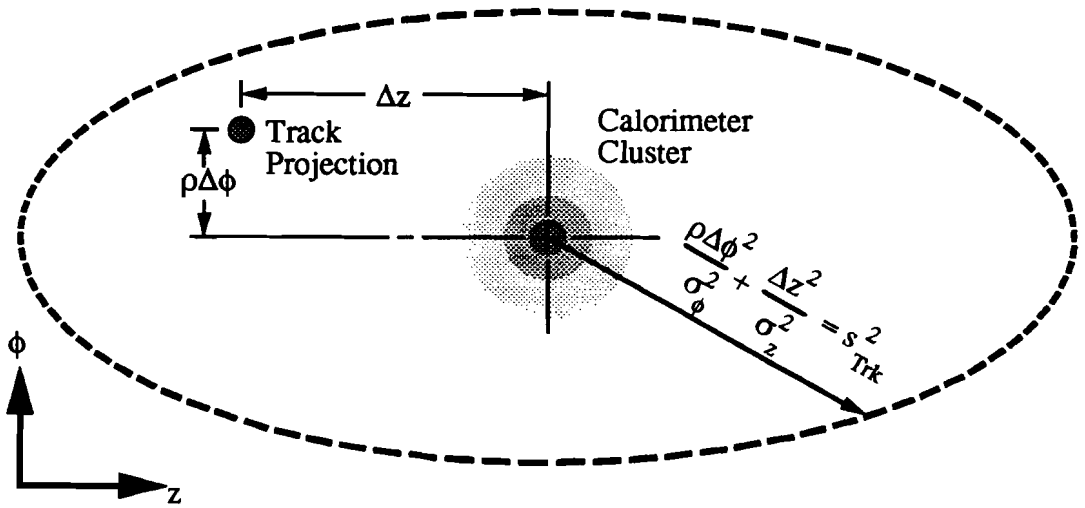

Figure 4.4: Definition of the track match significance in terms of the cluster centroid in EM3 and the projection of a track to this radius.

For electron backgrounds due to jets fragmenting into a leading π^0/η and additional nearby soft charged hadron(s), less proximity between the cluster and track projection is expected. Therefore, track match significance can be used as to discriminate between signal and background. Figure 4.5 shows the significance distributions for both signal and background dominated samples. As expected, the signal distributions peak at small values, while the background distributions exhibit long tails. For this analysis, a the track-cluster match requirement was $s_{\rm trk} < 5$ in the central region and $s_{\rm trk} < 10$ in the forward region.

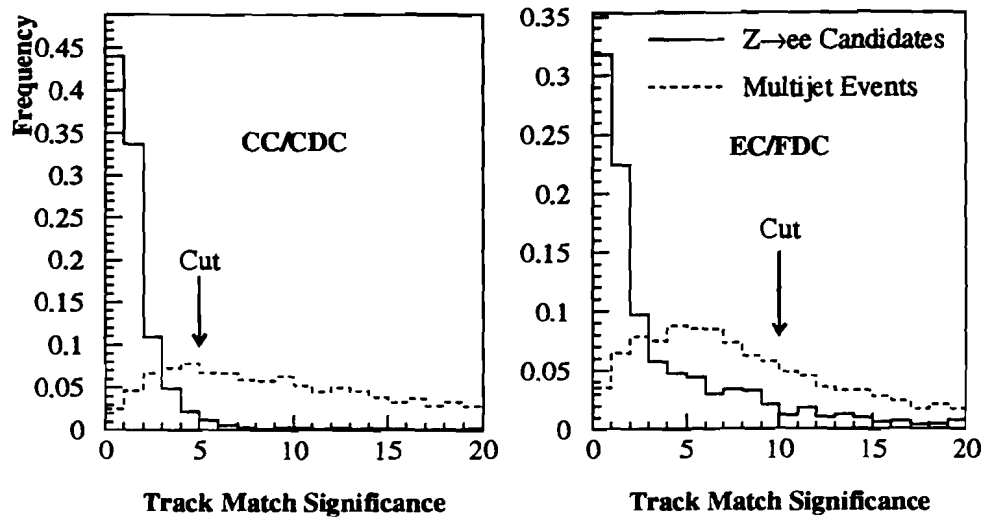

Figure 4.5: Track match significance distributions for $Z \rightarrow ee$ and Multijet-dominated samples for central (CC/CDC) and forward (EC/FDC) angles.

The above criteria (isolation, shower shape, and track matching) form the basis of "standard" electron/photon identification techniques employed at DØ. The next section describes some additional methods which are specific to this analysis.

4.8 Extensions to Standard Techniques

Improvements to "standard" electron/photon identification can be made which result in higher efficiencies, lower background levels, and smaller systematic uncertainties. The extended techniques used in this analysis make use of tracking information to improve vertex determination and discrimination between electrons,

photons, and background.

As mentioned earlier, the standard distinction between photons and electrons is based on whether or not a track is found in the road defined by the calorimeter cluster and the primary vertex. If the vertex position is not measured accurately, the road definition is incorrect, which leads to possible misidentification of electrons as photons. Any kinematic quantities (E_T, invariant masses, etc.) which depend on the vertex position will be affected as well. Fortunately, enough data exists on the μDST to allow this problem to be remedied. A routine called ELE_TRACKS was developed for this purpose. The next section describes how this routine works.

4.8.1 Track-Cluster Matching and Vertex Corrections

Instead of relying on tracking roads, track-cluster association in ELE_TRACKS is based solely on the match significance of a given track-cluster pair.[4] The track which is best matched to a cluster is not required to fall within the tracking road described previously; it need only satisfy the match significance criteria. This track can then be used to unambiguously determine where the electron originated by extrapolating the line connecting the calorimeter cluster centroid and the drift chamber hits center of gravity to the beamline. Thus vertex z position, denoted z_v, is given

[4]The ELE_TRACKS routine only considers tracks from the DTRK and FDCT banks since the linked tracks in the ZTRK bank are fit using the vertex position found by DØRECO. Tracks from the VTX chamber are also ignored.

by

$$z_v = z_0^{\rm trk} - \left(\frac{z_0^{\rm cal} - z_0^{\rm trk}}{\rho_0^{\rm cal} - \rho_0^{\rm trk}} \right) \rho_0^{\rm trk} \tag{4.1}$$

where $(z_0^{\rm trk}, \rho_0^{\rm trk})$ and $(z_0^{\rm cal}, \rho_0^{\rm cal})$ are then centroid positions of the drift chamber and calorimeter hits, respectively.[5] This extrapolation is shown schematically in figure 4.6 for clarity. The track hit centroids are used since corrections to CDC delay line biases are parameterized in terms of the centroid positions [69]. The best matched track must satisfy the significance criteria described earlier: $s_{\rm trk} < 5$ in the central region and $s_{\rm trk} < 10$ in the forward region.

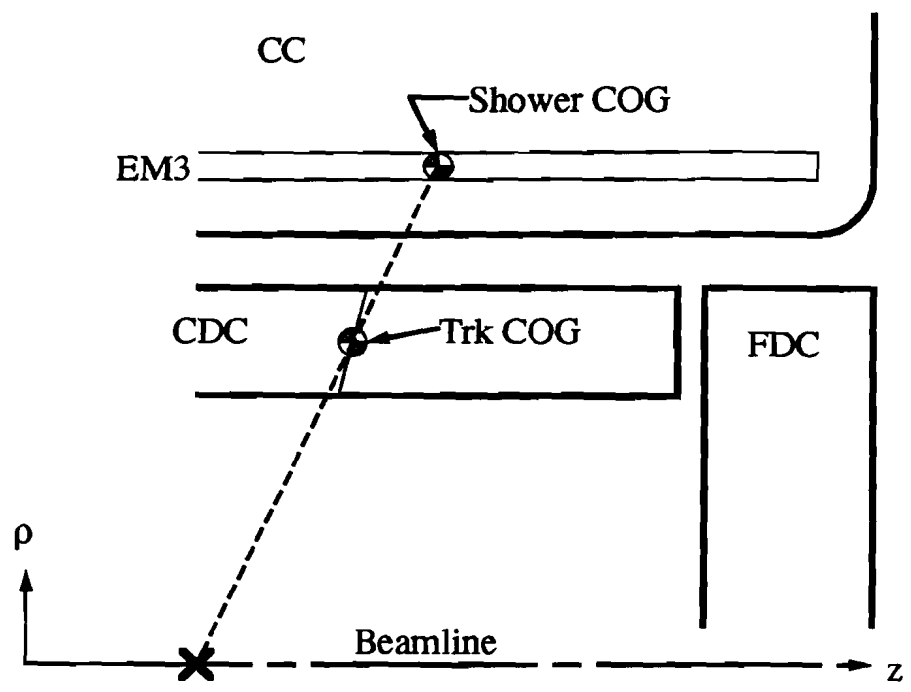

Figure 4.6: Vertex determination by cluster-track projection method.

[5] For FDC tracks, z_0 and ρ_0 are more properly regarded as track parameters than hit centroids since the z_0 position is fixed at ± 105.3 cm for FDC track reconstruction.

The vertex resolution achieved by this technique can be measured from the differences in the z-intercepts from the two electrons in $Z \rightarrow ee$ candidate events. Assuming that the intercepts z_{v1} and z_{v2} are uncorrelated, the single "electron vertex" resolution is given by

$$\sigma_z = \frac{1}{\sqrt{2}}\sigma_{(z_{v1}-z_{v2})}$$

where σ_z is the resolution obtained from either electron alone. Distributions of $(z_{v1} - z_{v2})$ indicate $\sigma_z \approx 2.0$ cm (or better) for either central or forward electrons.

Given the single electron vertex resolution, it is possible to quantify the frequency at which DØRECO mismeasures the primary vertex position. For the purposes of this study, a vertex is considered mismeasured if it is at least 10 cm ($\sim 5\sigma_z$) distant from the electron vertex. As is shown in figure 4.7a, the rate at which this occurs in $Z \rightarrow ee$ candidate events grows as the instantaneous luminosity increases. No mass window was imposed, and the electron vertex was calculated only from the electron nearest $\eta_{det} = 0$ which has a matching track. For the inclusive sample at all luminosities, about 13% of these events have mismeasured primary vertices. Contrarily, the rate at which $(z_{v1} - z_{v2}) > 10$ cm is relatively insensitive to the instantaneous luminosity, which indicates that the electron-vertexing technique is robust. (The busy environment associated with high luminosity running might have been expected to adversely affect the electron vertexing method due to random overlaps and/or track reconstruction inefficiencies.) Shown in figure 4.7b is the $Z \rightarrow ee$ candidate invariant mass spectrum for both vertexing techniques. An increase

of events in the central peak is clearly visible when the electron vertex is employed. The broader distribution characteristic of the standard vertexing algorithm is caused by misreconstructed vertices which lead to miscalculation of the opening angle of the two electrons in the event. This provides the final impetus to employ the electron-based vertexing technique in this analysis.

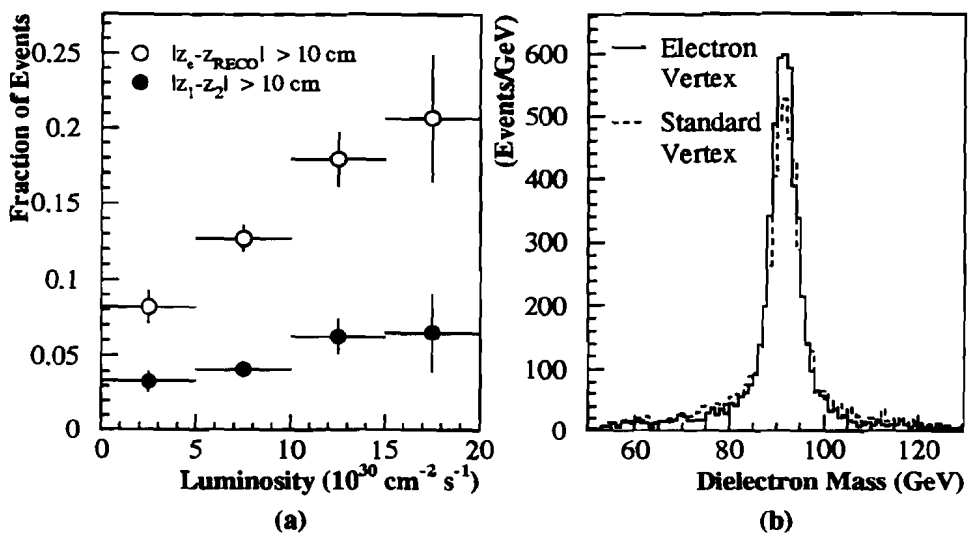

Figure 4.7: (a) Frequency at which the electron vertex is found more than 10 cm from the standard (DØRECO) vertex. Also shown is the rate at which the electron track z intercepts differ by more than 10 cm. (b) Invariant mass distribution for $Z \rightarrow ee$ candidate events using the two vertexing schemes.

4.8.2 Hit Counting Techniques

In the previous section it was demonstrated that the event vertex could be reliably identified using the track associated with one of the electrons in $Z \rightarrow ee$ events. To increase the overall detection efficiency for $ee\gamma$ (or ee) events, it is necessary to relax the tracking requirement on one of the electrons, i.e., accept e"γ"γ events. However, this approach leads to some kinematic ambiguities for the final state since it is not immediately obvious which photon originated from an electron. In principle, this ambiguity can be resolved kinematically through the use of mass combinations, but backgrounds must also be considered. For example, processes such as $WZ \rightarrow ee e\nu$ can yield the $ee\gamma$ signature if one of the electron tracks is not reconstructed. Although this process has a relatively small cross section, any one of the three final state electrons would contribute to the high-p_T tail of the photon spectrum if a track were lost. Since the sensitivity to $Z\gamma$ interactions is highest in this region, the results of the analysis would then be fairly dependent on knowledge of this background. The situation could be improved if a more efficient method were available for distinguishing electrons from photons and it is for these reasons that a "hit counting" technique is used in this analysis.

The hit counting technique employed here uses roads defined by $\Delta\phi = \pm 7.5$ milliradians in the central region and $\Delta\phi = \pm 15$ milliradians [70] in the forward region.[6] Within the road, the number of sense wire hits with drift times compatible

[6]Due to the vertexing problems mentioned earlier, only xy view (ϕ) CDC hit information was

with ionization originating from within the road were counted. Figure 4.8 shows the number of hits $N_{\rm hit}$ within the electron road for $Z \rightarrow ee$ candidates. For central electrons, the distribution peaks near 28 hits, corresponding to the situation in which each of the 28 available sense wires has recorded a signal. Meanwhile, the dashed line indicates the response expected from (non-converting) photons. This distribution was obtained from roads rotated in ϕ for $Z \rightarrow ee$ candidates (see section 6.2). Since no activity is expected in this part of the central detector, the environment should be similar to that produced by a non-converting photon. As expected, the number of hits for such "emulated photons" peaks at zero. The long tail is due to unassociated tracks and hits ("random overlaps") which are not necessarily coincident with the shower in the polar (rz view) direction. A cut at $N_{\rm hit} = 20$ distinguishes the two populations well. Similarly, a cut at $N_{\rm hit} = 36$ is used to discriminate between photons and electrons in the forward region. The high multiplicity environment at forward angles makes this distinction less pronounced than in the forward region.

4.9 Particle ID Summary

In summary, the post-reconstruction criteria used in the selection of electrons and photons involve isolation, shower shape, track matching, and hit counting. One is left with three types of objects: "tight" electrons (e_t) which have a matching

used in this analysis; no delay line (z) information was used. Since the hits are dropped from the μDST files, three-dimensional hit counting cannot be easily performed using the corrected vertex position.

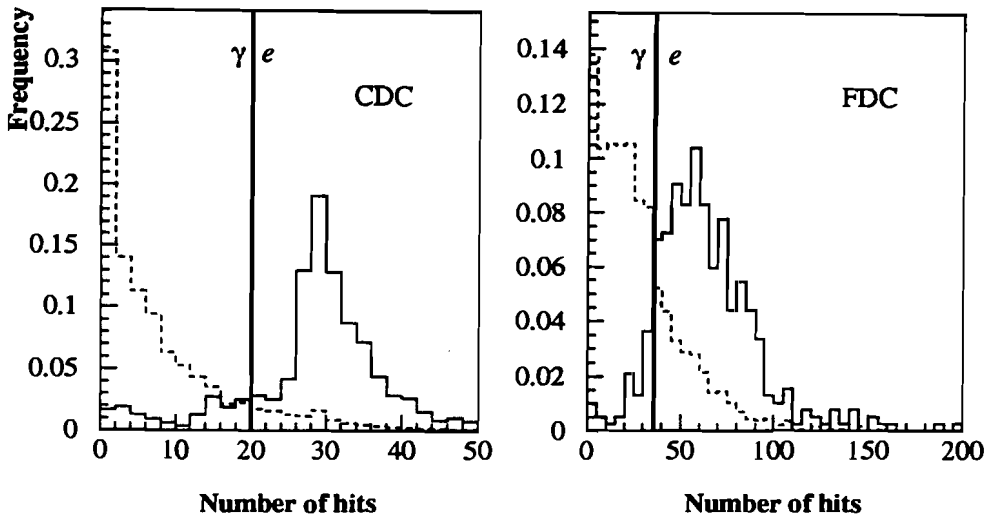

Figure 4.8: Number of drift chamber hits for both $Z \rightarrow ee$ candidates (solid) for both the central and forward regions. The dashed line indicates the number of random hits in emulated photon roads.

Object Type	Energy Isolation	Shower Shape	Track Match	Hits in Road
e_t	$I < 0.10$	$\chi^2 < 100$ (200)	$s_{\rm trk} < 5$ (10)	-
e_l	$I < 0.10$	$\chi^2 < 100$ (200)	-	$N_{\rm hit} > 20$ (36)
γ	$I < 0.10$	$\chi^2 < 100$ (200)	$s_{\rm trk} > 5$ (10)	$N_{\rm hit} \leq 20$ (36)

Table 4.1: Summary of electron/photon selection criteria. Quantities in parenthesis are values used for objects in the forward region.

track, "loose" electrons (e_l) which have hits or a track, and "photons" (γ), which have neither a track nor hits associated with them. For convenience, the cuts leading to these objects are summarized in table 4.1.

Chapter 5

Event Selection

The selection of candidate events is based on both kinematic criteria and the previously described particle identification techniques. Recall that the reaction of interest is $p\bar{p} \rightarrow e^+e^-\gamma X$. The "$X$" denotes that event selection is inclusive, i.e., events are not rejected which contain additional objects such as jets. Therefore, the desired final state is characterized by at least three electromagnetic calorimeter showers.

The choice of kinematic criteria is driven by the desire to maximize sensitivity to signals of $Z\gamma$ interactions while minimizing the amount of background in the final sample. Trigger considerations also influence these choices. For example, as is indicated in figure 1.4, the jet cross section increases rapidly as p_T thresholds are lowered. At the same time, cross sections for electrons due to electroweak boson

production decrease at low-p_T. This implies that triggers with relatively low transverse momentum thresholds will be susceptible to multijet backgrounds and would consume large amounts of available bandwidth while yielding small amounts of the desired signal. Recall also from section 2.4 that $ee\gamma$ events containing low-p_T objects are dominated by radiative decay contributions. Sensitivity to $Z\gamma$ interactions in this kinematic region is minimal, so $ee\gamma$ events at low-p_T contain relatively little information about the physics of interest. In light of these considerations, events are only accepted which satisfy the following criteria:

- Fiducial: $|\eta_{\rm det}| < 1.0$ (CC) or $1.5 < |\eta_{\rm det}| < 2.5$ (EC)
  $|\Delta\phi(\text{cluster}, \text{crack})| > 0.01$ in the CC
- Transverse Energy: $E_T^e > 25$ GeV and $E_T^\gamma > 10$ GeV
- Angular Separation: $\Delta\mathcal{R}_{e\gamma} > 0.7$

The fiducial cuts restrict objects to regions of the calorimeter where particle identification is reliable. (c.f. section 3.2.2.) The $\Delta\mathcal{R}$ requirement ensures that the objects are well separated and satisfy isolation requirements. Radiative decays are the dominant contribution to the cross section at small $\Delta\mathcal{R}$, so this cut does not affect experimental sensitivity to $Z\gamma$ interactions significantly.

The same triggering scheme is used as for $Z \rightarrow ee$ candidates. Recall from section 3.2.4 that two EM towers are required with $E_T > 7$ GeV at the trigger level. The second level software filter, dubbed `em2_eis2_hi`, subsequently requires

two isolated electron candidates with $E_T > 20$ GeV before an event is permanently recorded.

The selection of $ee\gamma$ candidates proceeds by the identification of events collected with the `em2_eis2_hi` filter which have the desired $e_t e_l \gamma$ signature. This process is outlined in table 5.1. Obviously, step 6 can be omitted if one desires $Z \rightarrow ee$ candidates with the $e_t e_l$ signature. As will be discussed in the next section, this sample proves extremely useful in the estimation of electron detection efficiencies.

Event selection is complicated somewhat by absence of drift chamber hit information in μDST files created with DØRECO versions lower than 12.14. To alleviate this shortcoming, $ee\gamma$ candidates were first selected with relatively loose cuts, then the corresponding STA files were obtained. The final event selection was performed on these events after reconstruction with DØRECO v12.20.

A total of 14 $e_t e_l \gamma$ candidates were identified in the run 1B data. The event displays for one candidate are shown in figures 5.1 and 5.2. (The energy deposits visible in the hadronic calorimeter are due to the fact that the event was recorded during the microblank period.) In this event, the photon is of relatively low momentum ($p_T^\gamma \approx 11$ GeV), the dielectron mass is approximately 71 GeV, and the dielectron-photon mass is about 94 GeV, so the event is probably a radiative decay. The kinematic properties and the particle identification quantities of all 14 events are summarized in appendix A. Further meaningful discussion of these events is

1. Events which satisfy the `em2_eis2_hi` L2 filter are selected.
2. Events are required to contain at least 2 electromagnetic clusters which satisfy the isolation and shower shape criteria in table 4.1.
3. At least one cluster is required to have a matching track (e_t). The vertex z position is then calculated using the most central (smallest $|\eta_{\rm det}|$) candidate with a matching track.
4. If a second electron candidate is not found which satisfies the track match criteria, at least one additional cluster is required which satisfies the e_l drift chamber hit criteria of table 4.1.
5. The transverse energies of the objects in the event are calculated using the vertex position from step 2. The two electron candidates e_t, e_l are required to have $E_T > 25$ GeV.
6. A photon candidate with $E_T > 10$ GeV is required which satisfies the criteria of table 4.1 and is separated from either electron candidate by $\Delta\mathcal{R} > 0.7$.

Table 5.1: Selection process for $e_t e_l \gamma$ events.

impossible without knowledge of efficiencies and backgrounds, so further attention to these candidates is deferred until later sections.

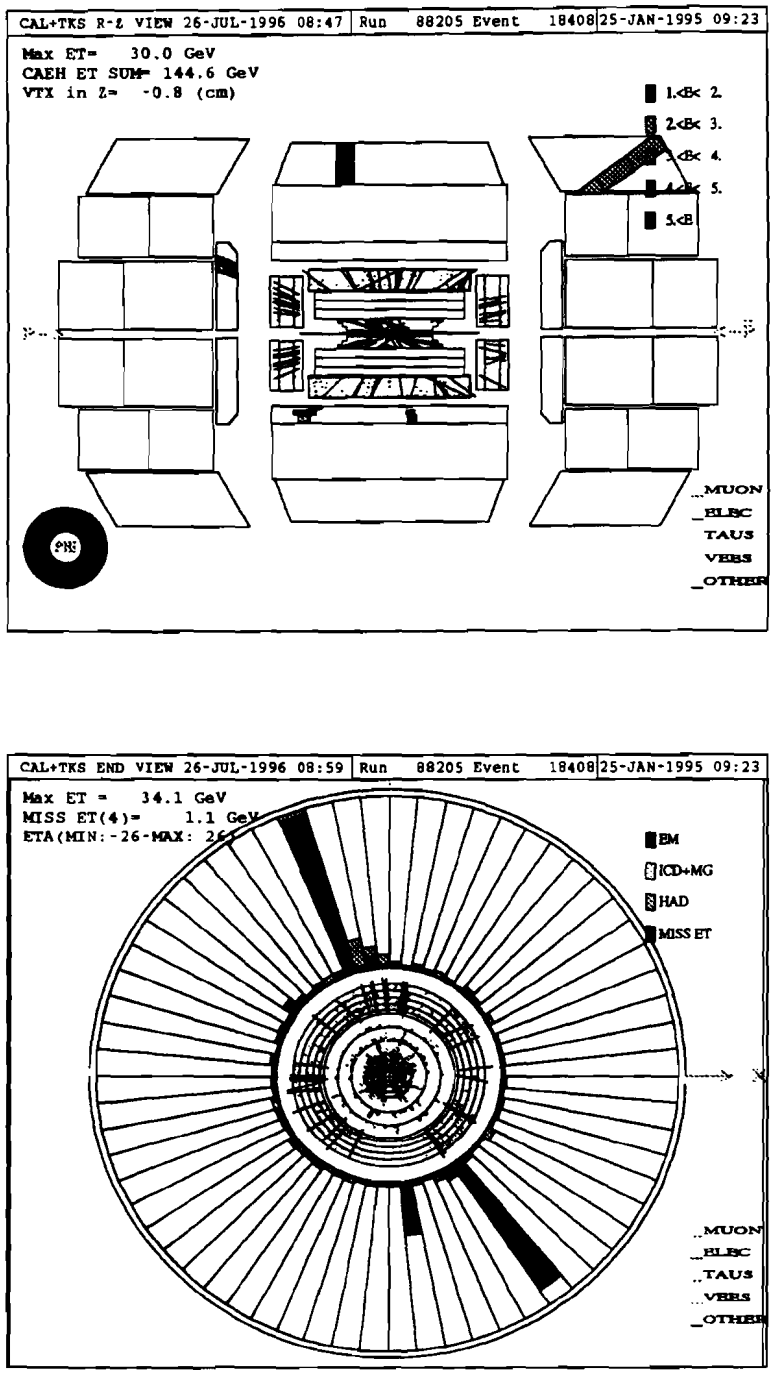

Figure 5.1: Side and end views of one $p\bar{p} \rightarrow ee\gamma$ candidate.

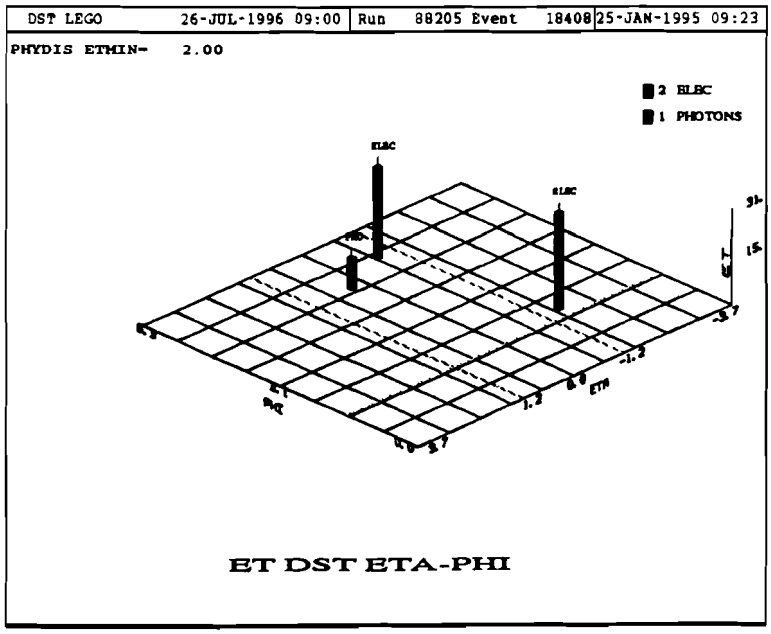

Figure 5.2: Lego plot for one $p\bar{p} \rightarrow ee\gamma$ candidate.

Chapter 6

Detection Efficiencies

Not all $ee\gamma$ events produced in the detector will appear in the final candidate sample. For example, an electron would escape detection if it were directed at the region between the central and end calorimeters where no electromagnetic calorimeter exists. Shower fluctuations could cause an electron to be rejected by the isolation and shower shape requirements. Photons can convert in the detector or might be overlapped by an unassociated random track in the event. Clearly, any measurement of physical processes at the point of collision requires knowledge of the frequency at which events are lost due to such effects. The purpose of this section is to describe how these losses are quantified.

Generally, the overall detection efficiency, denoted by ϵ, can be factored into two pieces:

$$\epsilon = \mathcal{A}\epsilon_{\mathrm{ID}} \tag{6.1}$$

where $\mathcal{A}$ is the kinematic *acceptance* and $\epsilon_{\rm ID}$ is the reconstruction and identification efficiency. The acceptance can be calculated using the geometry and momentum resolution of the detector. The efficiency $\epsilon_{\rm ID}$ can be estimated either from Monte Carlo simulations or from collider data itself. This analysis relies on the latter method as much as possible.

Efficiency measurements are complicated by the absence of drift chamber hit information in μDST's which were reconstructed with DØRECO versions 12.14 or lower. Figure 6.1 shows the distribution of events collected with the `em2_eis2_hi` L2 filter among various DØRECO versions. About 45% of the data were reconstructed with version 12.15, and about 80% were reconstructed with versions 12.15 or higher. For the purposes of this study, efficiencies are measured using only this latter 80% of the whole dataset.

6.1 Electrons

The Tevatron provides a convenient source of high-p_T electrons through the $Z \rightarrow e^+e^-$ process which are ideal for studying efficiencies[71, 72]. The data-based technique used for efficiency measurements relies on the fact that a dielectron candidate pair can be identified ("tagged") as a $Z \rightarrow e^+e^-$ candidate by the invariant mass of the pair. The change in the number of candidates in the mass peak for different cuts allows the relative efficiency to be determined. The relative efficiency

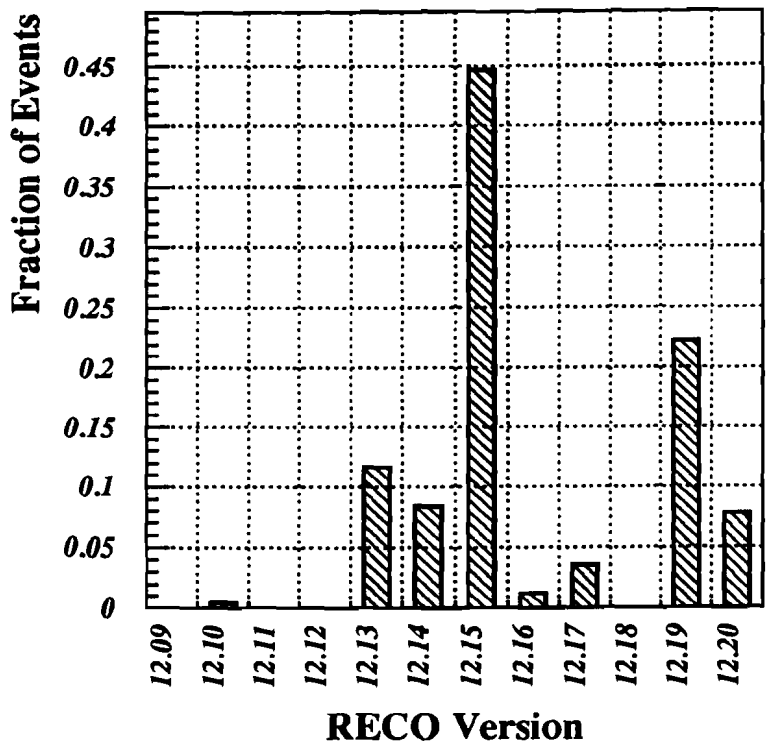

Figure 6.1: Fractions of sample reconstructed with various DØRECO versions for data collected with the `em2_eis2_hi` L2 filter.

of cut "a" relative to (a usually looser) cut "b" is given by

$$\epsilon_{ab} = S_{ab}/S_b$$

where S_{ab} and S_b denote the number of background-subtracted events in the mass peak after background subtraction for cuts "a" and "b" together and cut b alone, respectively. Of course, the precision of any such data-based measurement is statistically limited by the number of available Z events. Also, any ignorance of the

amount of background in the signal peak gives rise to a systematic uncertainty.

Method	Background Subtraction	Signal Peak
A	BW⊗G Fit	$81 < M_{ee} < 101$ GeV
B	BW⊗G Fit	$76 < M_{ee} < 106$ GeV
C	Sideband	$81 < M_{ee} < 101$ GeV
D	Sideband	$76 < M_{ee} < 106$ GeV

Table 6.1: Summary of background subtraction methods and signal windows used in electron identification efficiency measurements.

To quantify this uncertainty, the efficiencies were measured using the four methods outlined in table 6.1. For methods A and B, the dielectron invariant mass spectrum was fit using a Breit-Wigner convoluted with a Gaussian (to account for the finite experimental mass resolution) and a linear background. This linear background fit is then used to estimate the number of signal electrons in the mass peak. The difference between methods A and B is the width of the mass window used to define the signal peak . Methods C and D use a sideband average technique to estimate the number of signal electrons in these same mass windows. The lower sideband encompasses the range $60 < M_{ee} < 70$ GeV, while the upper sideband is defined by $110 < M_{ee} < 120$ GeV. The resulting numbers of signal electrons are summarized in table 6.2 for each of the four methods.

Relative efficiencies can then be calculated from the ratios of these numbers

Cuts	S_A	S_B	S_C	S_D
Trigger · Kinematic	5395	5666	5307	5534
$\mathcal{I} \cdot \chi^2$	4959	5198	4877	5075
$\mathcal{I} \cdot \chi^2 \cdot s_{\rm trk}$	3972	4145	3916	4062
$\mathcal{I} \cdot \chi^2 \cdot (N_{\rm hit}$ or $s_{\rm trk})$	4827	5052	4752	4939

Table 6.2: Number of electrons in Z mass window for various offline cuts and background subtraction methods. Only central candidates reconstructed with DØRECO versions 12.15 and higher are shown.

using equation 6.1. For example, the efficiency of the track match requirement for central electrons using method A is given by

$$\epsilon_{\rm trk} = \frac{3972}{4959} = 0.8010 \pm 0.0057$$

where the (binomial) uncertainty is purely statistical at this point. To estimate the systematic uncertainties, efficiencies are calculated using all four methods and the central value is taken from the method nearest the mean. The systematic uncertainty due to the background shape is then assigned to be half the difference of the highest and lowest values. Finally, the overall systematic uncertainty is computed by adding the statistical uncertainty on the efficiency ratio and the background systematic uncertainty in quadrature. Table 6.3 contains the efficiencies obtained in this manner for both the forward and central regions. The quantities ϵ_t and ϵ_l in table 6.3 are the identification efficiencies for tight and loose electrons, respectively. The efficiency for the calorimeter-based cuts $(\mathcal{I}, \chi^2)$ is denoted $\epsilon_{\rm cal}$, the efficiency for track reconstruction is denoted $\epsilon_{\rm trk}$, and the efficiency for a track or hit requirement

Quantity	CC Value (%)	EC Value (%)
$\epsilon_{\rm cal}$	91.74 ± 0.38	91.96 ± 0.55
$\epsilon_{\rm trk}$	80.10 ± 0.63	73.49 ± 0.92
$\epsilon_{\rm hit}$	97.34 ± 0.36	96.47 ± 0.43
ϵ_l	89.47 ± 0.46	88.42 ± 0.71
ϵ_t	73.62 ± 0.68	67.61 ± 0.97

Table 6.3: Measured efficiencies for electron identification. See text for definitions.

is denoted $\epsilon_{\rm hit}$. With these definitions, $\epsilon_t \simeq \epsilon_{\rm cal}\epsilon_{\rm trk}$ and $\epsilon_l \simeq \epsilon_{\rm cal}\epsilon_{\rm hit}$.

Given these efficiencies, the gain achieved by relaxing the tracking requirement on one of the electrons can now be quantified. If both electrons happen to be in the same region, the detection efficiency for the e_te_t signature is simply ϵ_t^2, while the efficiency for the e_te_l signature is given by

$$\epsilon_{tl} = 2\epsilon_l\epsilon_t - \epsilon_t^2$$

where is has been assumed that the efficiencies for the individual electrons are uncorrelated. The expected signal gain G relative to the e_te_t requirement is

$$G \equiv \frac{\epsilon_{lt}}{\epsilon_{tt}} = 2\frac{\epsilon_l}{\epsilon_t} - 1$$

which implies that 143% more signal is expected for electron pairs in the central region if e_te_l cuts are used instead of e_te_t cuts.

It should be noted that the above efficiencies have been measured using data that are biased by trigger requirements; nothing has been said about events which are lost due to trigger inefficiencies. One method for estimating such losses is from

"mark-and-pass" data which are recorded regardless of the trigger decision. A similar method is used here to estimate the efficiency of the `em2_eis2_hi` filter. Data taken with the `em2_ele_esc` filter had the same L1 requirement, a relaxed E_T requirement (16 GeV), and no isolation or shape requirement on one of the electrons. To the extent that electrons satisfying 16 GeV requirement are unbiased with respect to the 20 GeV E_T, isolation, and shape requirements of `em2_eis2_hi`, the L2 efficiency can be measured using coincidences of the two filters in $Z \rightarrow ee$ events identified offline. This method yields a L2 efficiency of nearly 100% per high-p_T electron. In order to measure the efficiency in the vicinity of the E_T threshold, candidate electrons are selected using the identification criteria of table 4.1 which were collected with the `ele_1_mon` or `eletrk_1_mon` single electron filters. The fraction of events in each E_T bin which satisfied $E_T > 20$ GeV (as calculated by L2) is a measure of the E_T-dependence of the L2 requirement. Figure 6.2 shows the resulting efficiency curve.[1] It might be expected that this measurement is affected by background contamination since electron backgrounds tend to have a lower electromagnetic component than genuine electrons. The energy (and E_T) resolution might be degraded in the presence of background since hadronic energy resolution is generally worse than electromagnetic resolution. To investigate this possibility, the measurement was repeated with a requirement that the 95% of the shower be

[1]The efficiencies are not 50% at the threshold of 20 GeV due to differences in the offline and L2 energy scales.

contained in the EM calorimeter. The error bars in figure 6.2 reflect how the efficiency changes when this cut is imposed; a negligible effect is seen in the vicinity above the offline cut of 25 GeV.

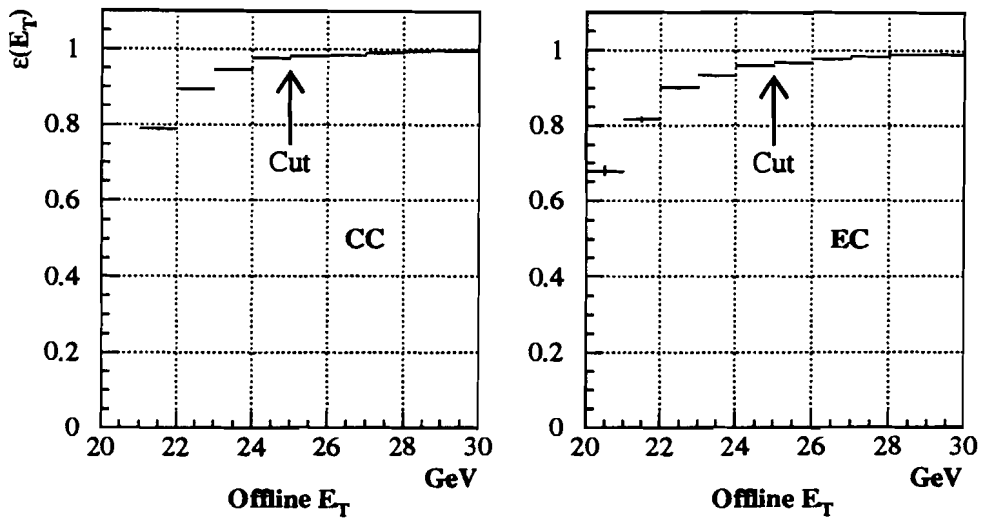

Figure 6.2: Efficiency of L2 $E_T > 20$ requirement for electron-like objects. Error bars indicate sensitivity to EM energy fraction requirement.

Additionally, there are small inefficiencies [73] due to the L1 and L1.5 hardware triggers. These can be safely neglected for the purposes of this study.

A possible area of concern regarding data-based efficiency measurements involves vertex misreconstruction. Since the μDST files on which the measurements were based contain only tracks found within the (rather wide) road between calorimeter clusters and vertices, events with poorly reconstructed vertices might

be excluded entirely from the sample used for efficiency measurements. (Recall that at least one electron is required to have matching track here in order to determine the vertex.) Such effects were studied using STA files corresponding to about 10% of the dielectron data sample selected with loose calorimeter-based criteria alone. These 1000 events were reconstructed with DØRECO version 12.20 with full tracking and the electron identification efficiencies were measured. The efficiencies measured with this sample were in close agreement to those measured with the full μDST sample. Furthermore, the efficiency measurements were unchanged when the data were converted to μDST format from STA format. Therefore, the effects of vertex misreconstruction and data truncation in the μDST format are negligible for the purposes of this analysis.

6.2 Photons

Since the photon calorimeter showers are expected to be very similar to those for electrons, the efficiencies for the isolation and shower shape requirements from the previous section can be applied to photons as well. However, corrections must be made for inefficiencies at low energy. (Recall that photons are accepted with $p_T > 10$ GeV/c.) For example, the underlying event can deposit energy (usually ~ 1 GeV) into the isolation cone surrounding the photon. This can cause photons of comparable energies to fail the isolation requirement. Due to the absence of a

clean source of photons in collider data, the measurement of this inefficiency must rely partially on Monte Carlo (MC) simulations.

To measure the p_T dependence of the calorimeter-based quality cuts, the calorimeter response to a sample of photons was simulated using DØGEANT. These events were then superimposed on non-zero-suppressed minimum bias collider events to simulate underlying event effects.[2] Figure 6.3 shows the resulting efficiency of the calorimeter-based quality requirements as a function of the photon transverse momentum. As expected, the efficiency drops at low-p_T and is more sensitive in the central region where photons have a lower energy for a given p_T. In both cases, the efficiency reaches a plateau around $p_T \approx 23$ GeV/c.

In order to maintain consistency with the previous data-based results, the plateau values are normalized to the $\epsilon_{\rm cal}$ values in table 6.3, and the p_T dependence is fit with a quadratic function below 23 GeV/c. This ensures that the p_T-dependent efficiency obtained with the MC only have the correct shape. Thus, the calorimeter-based selection efficiency is parameterized as

$$\epsilon_{\rm cal}(E_T) = \begin{cases} \epsilon^0_{\rm cal}(a_0 + a_1 E_T + a_2 E_T^2), & E_T \leq 23\text{GeV} \\ \epsilon^0_{\rm cal}, & E_T > 23\text{GeV} \end{cases} \tag{6.2}$$

where $\epsilon^0_{\rm cal}$ is from table 6.3 and the fitted values of a_0, a_1, and a_2 are given in table 6.4. A systematic uncertainty of 2% is assigned to the total $ee\gamma$ signal efficiency

[2]The minbias data were recorded at instantaneous luminosities of 5.4, 10.0, 13.9, and 19.2×10^{30} cm^{-2} s^{-1}. After overlaying the MC photons, the events were weighted to reflect the instantaneous luminosity distribution of the $Z \to ee$ sample. The event superposition code and minbias samples were kindly provided by Ian Adam.

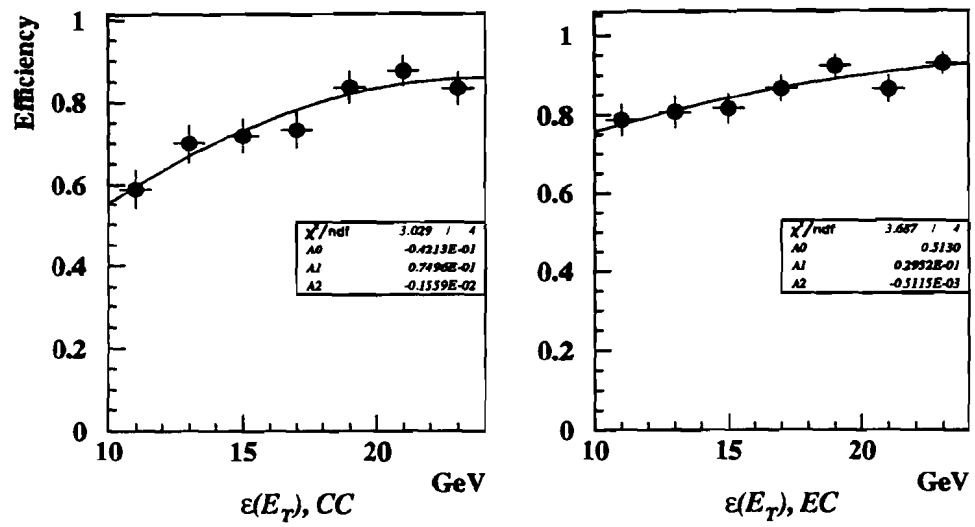

Figure 6.3: Efficiency of the isolation and shower shape requirements as a function of photon transverse momentum. The error bars are purely statistical.

Angular Region	a_0	a_1 (GeV^{-1})	a_2 (GeV^{-2})
$\lvert\eta_{\rm det}\rvert < 1.0$	-0.04915	0.08745	-1.819×10^{-3}
$1.5 < \lvert\eta_{\rm det}\rvert < 2.5$	0.5568	0.03204	-5.513×10^{-4}

Table 6.4: Parameters for low-p_T photon selection efficiency.

to account for the differences in the plateau efficiencies measured using data and these simulated photons.

Another ingredient in the photon selection efficiency is due to the track/hit veto requirements. This is measured from data using the emulated photon technique outlined previously in section 4.8.2. Approximately 10% of the inclusive $Z \rightarrow ee$

candidates with $81 < M_{ee} < 101$ GeV were selected from the total dataset and the STA files were obtained (since hit information outside electron roads is dropped from the μDST files). The hit counting analysis was performed in five roads offset from each of the two electrons in the event ($\Delta\phi = \pi/2, \pi/2 \pm 0.2, \pi/2 \pm 0.4$). Roads within $\Delta\mathcal{R} < 0.4$ of either electron were excluded from the study. Figure 6.4 shows the fraction of emulated photons which failed the track/hit veto criteria. In the central region, this random overlap rate is fairly constant at 18%. As expected, the inefficiency grows in the high-η region due to the increased multiplicity and wider roads relative to the central region. About 40% of the photons are lost for $|\eta| > 1.5$. However, $Z\gamma$ interactions are manifested mainly in the central region, so sensitivity to $Z\gamma$ interactions is maintained.

Finally, losses due to photon pair conversions ($\gamma \rightarrow e^+e^-$) in the presence of nuclei must be accounted for. This is done using the tracking and hit counting efficiencies in table 6.3 combined with an estimate of the amount of material between the interaction point and the innermost CDC wall and is further described in section 7.3.

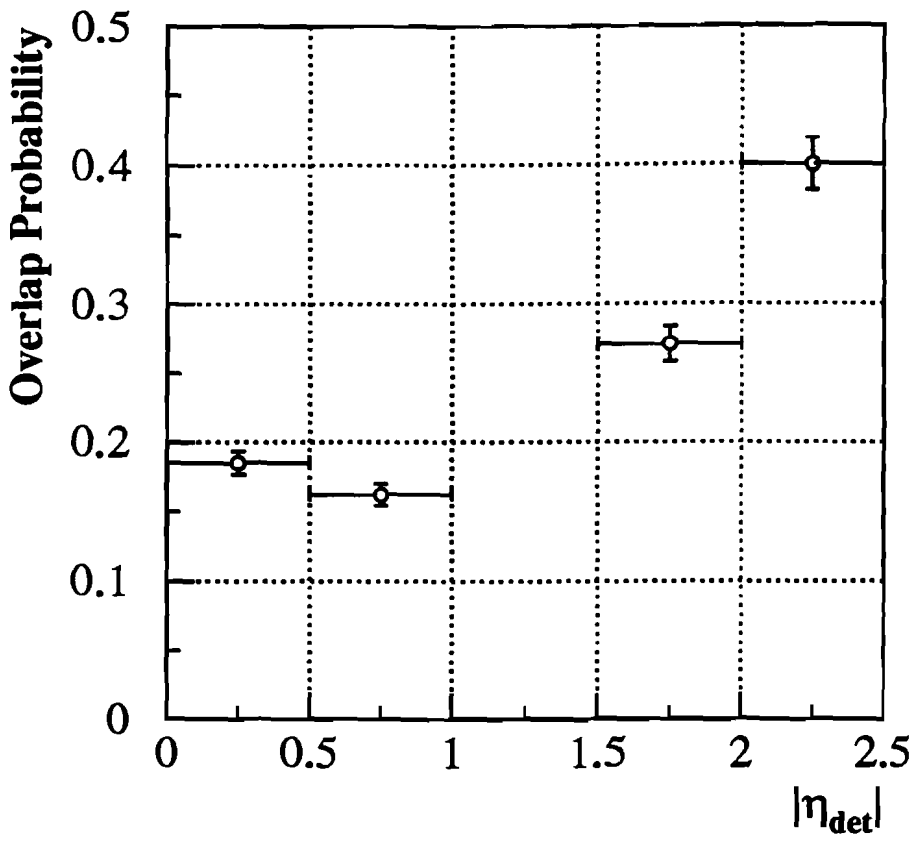

Figure 6.4: Inefficiency of the photon track/hit veto requirements as a function of angle as measured from $Z \rightarrow ee$ events. The error bars are purely statistical.

Chapter 7

Detector Simulation

The purpose of the previous efficiency measurements is to provide a basis for event yield predictions. To this end, a *parametric* simulation was developed which incorporates detector geometry, resolutions, and particle identification efficiencies. This approach differs from significantly from that used in "first principle" simulations, such as DØGEANT, which attempt to model low-level physical details of detector response, e.g., energy deposition in individual detector elements. Instead, emphasis is placed on modelling the detector response as simply and accurately as possible at the macroscopic level. One advantage of this technique, which will become more apparent later, is that it is much less computationally intensive than the detailed response approach. The remainder of this section details aspects of this parametric simulation which are directly applicable to this study. Further details are given in reference [74].

The input to the simulation consists of a list of final state particle four-vectors for each event. In this case, the source of these events is the LO Monte Carlo generator discussed in chapter 2 which was provided by the authors of reference [23]. A k-factor is used to approximate NLO corrections to the cross section. To simulate the kinematic effects of NLO contributions, the entire $e^+e^-\gamma$ system was given a transverse boost according to the theoretical predictions for single vector boson production given in reference [75]. Although this correction introduces additional theoretical uncertainties, the overall correction is small and mainly affects the lower end of the p_T^γ spectrum where sensitivity to $Z\gamma$ interactions is minimal.

7.1 Fiducial Acceptance

For each event, the vertex z position is selected from a Gaussian distribution centered at $z \approx 0$ with a width of approximately 30 cm to reflect the interaction position distribution observed in data. This position is then used to predict where the final state particles enter the calorimeter modules. Events are rejected in which one or more of the particles fail the fiducial criteria outlined in chapter 5.

7.2 Kinematic Resolution and Acceptance

The energy and momenta of the particles satisfying the fiducial criteria are smeared using Gaussian distributions with resolutions parameterized by

$$(\sigma_E/E)^2 = C^2 + S^2/E + N^2/E^2$$

where C, S, and N correspond to the constant term, sampling term, and noise term, respectively [64]. The sampling term is obtained from test beam results [65], and the constant and noise terms are tuned to match electron resolutions in $Z \rightarrow ee$ events simulated using DØGEANT. Table 7.1 lists these resolution parameters. After the

Quantity	CC Value	EC Value
C	0.017	0.0094
S	0.14 $\sqrt{\text{GeV}}$	0.157 $\sqrt{\text{GeV}}$
N	0.490 GeV	1.14 GeV

Table 7.1: Energy resolution parameters for electrons and photons.

particle momenta are smeared, events which fail the kinematic criteria of section 5 are rejected. Figure 7.1 shows a comparison between detector response to $p\bar{p} \rightarrow e^+e^-X$ for the parametric simulation and DØGEANT. In both cases, only fiducial and kinematic criteria were used to select candidate events. Kinematic distributions directly from the ISAJET Monte Carlo [18], which was used to generate the event

sample, are also shown. The electron E_T and η distributions of the two simulations simulations show good agreement both in terms of shape and normalization.

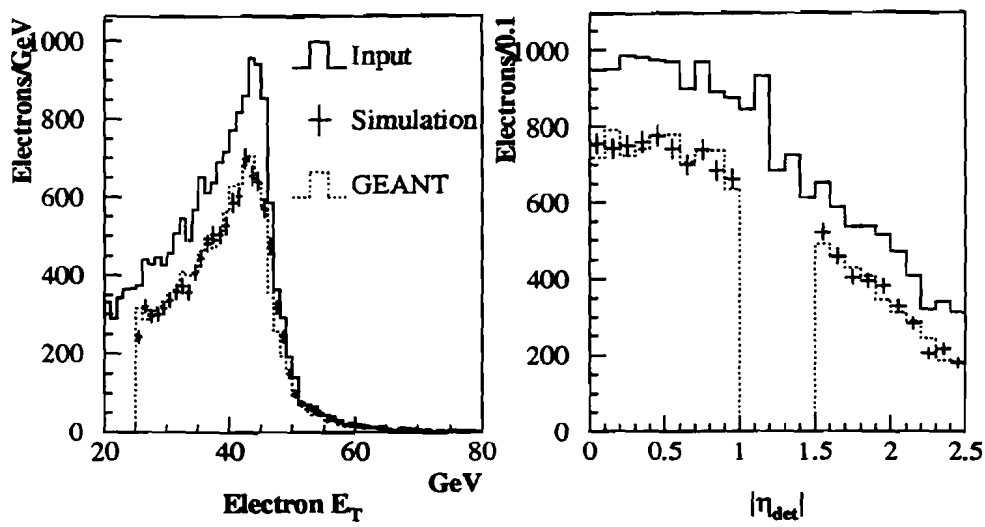

Figure 7.1: Comparison of detector response to $p\bar{p} \rightarrow e^+e^-X$ events subjected to kinematic and fiducial requirements on the electrons. Also shown are the E_T and η distributions of electrons directly from the ISAJET generator.

7.3 Selection Efficiency

The next step in the simulation procedure accounts for particle identification efficiencies. For each of the electrons in the event, a random number x is generated according to a uniform (flat) distribution in the range $[0, 1]$, and electrons are accepted as e_t if $x < \epsilon_t$ or e_l if $x < \epsilon_l$. For photons, the selection efficiency must

account for random track overlaps and conversions.

The probability that the photon in a given $e^+e^-\gamma$ event is rejected due to randomly overlapping tracks or hits, denoted $\epsilon_{\rm ol}$, is obtained directly from figure 6.4 using the rapidity of the photon. Photons will also be rejected if a $\gamma \rightarrow e^+e^-$ conversion occurs in the material between the interaction region and the drift chambers. The conversion probability, denoted here as $\epsilon_{\rm conv}$, is calculated from the interaction z position, the polar angle of the photon, and an estimate of the amount of material in the detector. This probability ranges from about 10% in the central region to 30% in the forward region. However, due to tracking inefficiencies, not all $\gamma \rightarrow e^+e^-$ conversions will be rejected. Therefore, the overall photon selection efficiency is given by

$$\epsilon_\gamma = \epsilon_{\rm cal}(1 - \epsilon_{\rm ol} - \epsilon_{\rm conv}\epsilon_{\rm trk})$$

where $\epsilon_{\rm cal}$ and $\epsilon_{\rm trk}$ are given in table 6.3.

Finally, corrections are made for the acceptance of events in which a misidentification of the type $e \leftrightarrow \gamma$ occurs. The fraction of such events is nearly negligible ($< 1\%$) due to tendency of photons to be produced with p_T below the electron requirement of 25 GeV and the relatively high efficiency of the drift chamber hit requirements for electrons.

7.4 Systematic Uncertainties

To make meaningful comparisons between observed data and theoretical predictions, it is necessary to evaluate the systematic uncertainties involved. In this case, the sources of these uncertainties can be roughly categorized as either theoretical or experimental. This distinction is sometimes ill-defined and is less important than the actual sizes of the uncertainties.

The theoretical uncertainties are the result of imperfect knowledge of parton densities, renormalization scale, the value of the k factor, and the p_T distribution of the $ee\gamma$ system. It is assumed that the k factor uncertainty is negligible (see section 2.5). The total $ee\gamma$ acceptance changes by about 1% if it assumed that the $ee\gamma$ system is produced at rest in the transverse plane, so this 1% represents a (crude) upper bound on the systematic uncertainty due to the p_T of the $ee\gamma$ system. By far, the largest source of theoretical uncertainty results from the choice of pdf. Figure 7.2 shows the how the predicted event yield varies relative to the MRSD'_ choice for a variety of pdf's. For each pdf choice, the central value corresponds to a renormalization scale of $\sqrt{\hat{s}}$, while the error bar indicates the variation resulting from the choices $\mu = \sqrt{\hat{s}}/2$ and $\mu = 2\sqrt{\hat{s}}$. In general, the pdf's extracted from data using leading order evolution approximations result in yields which are 10% lower than those using modern data and NLO evolution. A systematic uncertainty of 6% is ascribed to the combined choice of pdf set and renormalization scale. This

assignment was made to encompass the spread of predictions resulting from the use of contemporary pdf sets.

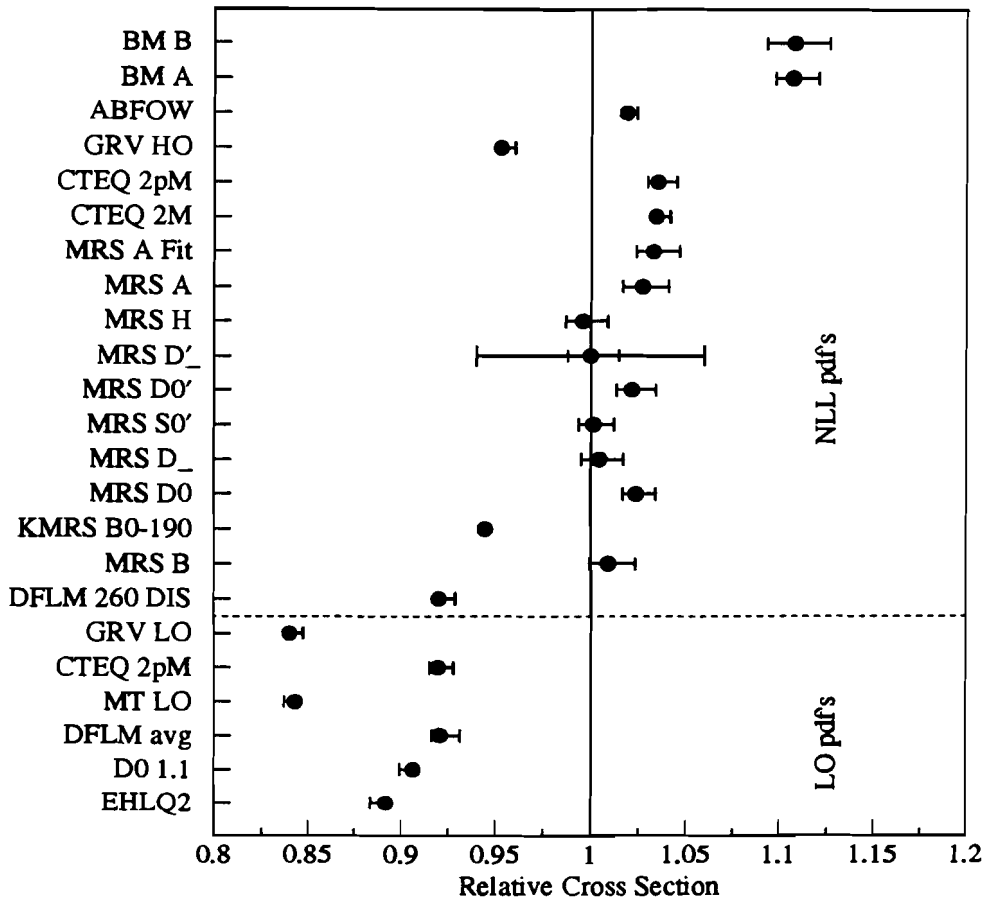

Figure 7.2: Comparison of predicted event yields for pdf choices. The individual error bars indicate sensitivity to the renormalization scale, and the large error bar on the MRSD'_ case indicates the systematic uncertainty assigned to the pdf choice.

Systematic uncertainties reflect the accuracy of the detector model, which

depends in part on the accuracy of detection efficiency are measurements. In chapter 6, the uncertainties on the electron and photon selection efficiency measurements were estimated to be about 0.7% per final state object. This introduces a systematic uncertainty of about $\sqrt{3} \times 0.7\% = 1.2\%$ on the overall detection efficiency. Another 2% must be included to account for the uncertainty in the estimate of low-p_T photon selection efficiency. Additionally, the statistical precision of photon random overlap measurement contributes about 3% to the overall efficiency uncertainty. Also, the amount of material in the detector is not known precisely, and an uncertainty of 5% is assigned to the conversion probability.

Finally, the predicted event yield depends on the integrated luminosity via the relation $N_{\text{pred}} = \mathcal{L}\epsilon\sigma$, where ϵ is the overall efficiency and σ is the cross section. As was discussed in section 3.2.4, the accuracy of the luminosity determination is limited by the theoretical uncertainty of the total cross section at forward angles. Therefore, a relative uncertainty contribution of 5.4% [76] is ascribed to the integrated luminosity.

All of the major sources of systematic uncertainty considered here are summarized in table 7.2. The total of these sources, when added in quadrature, is 10%. The estimated efficiency-corrected Standard Model $ee\gamma$ cross section from the simulation is $\epsilon\sigma_{ee\gamma} = 0.136$ pb. Therefore, the Standard Model prediction for the number of expected signal events observed in 89 pb^{-1} of data is 12.1 ± 1.2 events. This is close to the number of $e_t e_l \gamma$ candidates (14) observed in the data, so the existence

Source	Fractional Uncertainty
pdf choice	6 %
$p_T^{ee\gamma}$	1 %
Selection efficiency	1.2 %
Low-p_T^{γ} efficiency	2 %
Random overlap rate	3 %
Photon conversion rate	5 %
Luminosity	5.4 %
Total:	10 %

Table 7.2: Sources of systematic uncertainty for the predicted $ee\gamma$ signal yield.

of $Z\gamma$ couplings which are expected to result in large (> 50) events is unlikely. More quantitative statements must be deferred until possible background contributions have been accounted for.

Chapter 8

Backgrounds

In order to make meaningful comparisons between theoretical predictions and experimental observations, it is necessary to estimate the fraction of observed candidates which are not due to the $p\bar{p} \rightarrow e^+e^-\gamma X$ process. Generally, if background sources are known and cross sections can be reliably calculated, their contributions to the final sample can be estimated using the same simulation techniques employed to estimate the expected signal yield. Otherwise, the data-based techniques must be employed for background estimation. Both of these methods are used in this analysis.

8.1 Misidentified Jets

It is possible for a jet to hadronize such that it mimics the response expected from an electron or photon. For example, if a jet fragments into a leading π^0, the resulting $\gamma\gamma$ decay products will be nearly indistinguishable from a genuine photon in the detector. As is shown in figure 8.1, if isolated π^0/η are produced in conjunction with two electrons (possibly originating from a Z boson), the event might satisfy the $e^+e^-\gamma X$ selection criteria. Similarly, the presence of a charged hadron near the the leading π^0 would result in a drift chamber track, and the jet would resemble an electron. Events with such jets could also enter the final candidate sample.

In order to estimate the fraction of the $e_t e_l \gamma$ final state due to misidentified jets, it is necessary to know the frequency at which jets mimic photons (or electrons) as well as the inclusive cross sections for processes with jets in the final state. Although some of these cross sections are measured (such as $Z + j$ production) at the Tevatron, details of fragmentation processes are not. Therefore, a data-based technique is used to estimate the background due to misidentified jets. This method is independent of the physical origin of the background, and includes contributions from $Z(ee)j$ production as well as contributions from other processes such as jjj, and γjj production.

First, the misidentification frequency of jets as e_t, e_l, or γ are measured using data samples collected using triggers based on calorimeter towers. Such samples

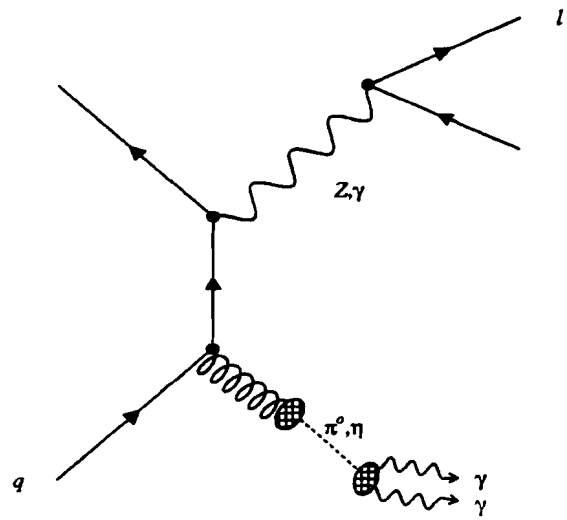

Figure 8.1: Diagram for background due to $Z + j$ production.

are overwhelmingly dominated by multijet production, so any electrons or photons identified in the samples are likely to be due to jet misidentification. (See figure 1.4 for a comparison of cross sections for various processes.) Details of the jet misidentification probability (or "fake rate") measurements are given in appendix B. These probabilities depend both on the jet transverse energy and the selection criteria applied to electron or photon candidates. The measured transverse energy dependences are approximately linear, so the fake rate $P(E_T)$ can be parameterized as

$$P = a_0 + a_1 E_T$$

where a_0 and a_1 are measured by fitting the data. Table 8.1 summarizes these measurements. The 30% systematic uncertainty for fake rates arises mainly from

Object Type	Central		Forward	
	$a_0 \times 10^3$	$a_1 \times 10^5$	$a_0 \times 10^3$	$a_1 \times 10^5$
e_t	-0.173 ± 0.20	1.43 ± 0.51	0.528 ± 0.86	5.09 ± 2.3
e_l	0.0754 ± 0.29	2.06 ± 0.70	1.32 ± 1.0	6.31 ± 0.27
γ	1.08 ± 0.17	-0.845 ± 0.352	0.64 ± 0.11	-

Table 8.1: Jet misidentification probabilities for electrons and photons. Errors quoted are statistical (fit) errors only. A systematic uncertainty of 30% is assigned to each fake probability. Uncertainties given in this table are statistical only.

uncertainties in the amount of genuine photon contribution to multijet-dominated sample.

Given these jet fragmentation probabilities, the background is estimated by appropriately weighting events which contain at least *two* of the objects in the desired $e_t e_l \gamma$ final state and a jet. (If more than one jet is present in the event, the appropriate background contribution is included.) These events have $e_t e_l j X$, $e_t j \gamma X$, or $e_l j \gamma X$ topologies. In the first case, the the same kinematic requirements ($E_T > 10$ GeV) are applied to the jet as would be applied to the photon in $e_t e_l \gamma$ events. In the latter two cases, the jet must satisfy kinematic requirements which would be applied to electrons. Trigger requirements introduce a complication since the `em2_eis2_hi` would reject $e_t j \gamma$ or $e_l j \gamma$ events with photons below $\simeq$ 25 GeV. Therefore, the

background contributions from $e_t j\gamma$ and $e_l j\gamma$ in the range $p_T^\gamma < 30$ GeV is estimated using data collected from single-electron filters.[1] Since these filters were prescaled relative to `em2_eis2_hi`, a normalization factor of 9.7 ± 0.5 was applied based on the number of $Z \rightarrow ee$ candidates collected under the two trigger types. Another complication arises from possible double-counting in the $e_t j\gamma$ and $e_l j\gamma$ cases since electrons which satisfy e_t criteria also satisfy e_l criteria. Such double-counting is avoided by introducing an additional type of object, denoted e_l^*, which satisfies the hit-count criteria of e_l but fails the track match requirements of e_t. This prohibits any possible intersection of the sets containing $e_t j\gamma$ and $e_l^* j\gamma$ events.[2]

Finally, this background estimate is based on data, so only events which were reconstructed with DØRECO versions 12.15 or higher (which had hit information) were used. Since this corresponds to 80% of the total dataset, the resulting estimate is scaled by $1/0.80 = 1.25$ to account for the missing data. After this correction, the total background estimate to $e_t e_l \gamma X$ is 1.81 ± 0.54 events, where the uncertainty is almost entirely due to the systematic uncertainties of the fake rates in table 8.1. About 75% of the estimated background is due to events in which $e_t e_l j$ events are misidentified as $e_t e_l \gamma$ events, which is consistent with the hypothesis that the background is dominated by $Z + j$ production. In terms of angular distributions,

[1]The events were required to satisfy one the following filters:
`em1_eletrk_mon`, `em1_eletrk_mon`, `em1_ele_mon`, `eletrk_1_mon`, or `ele_1_mon`.

[2]Since neither of the objects in $e_l^* j\gamma$ events have a matching track, the vertex cannot be determined from the track-cluster projection technique. Therefore the standard DØRECO vertex position is used for these events.

the bulk of the background (70%) is due to misidentified jets in the central region.

Background Source	Central Contribution	Forward Contribution	Central+Forward Contributions
$e_t e_l j$	1.000 ± 0.033	0.321 ± 0.016	1.321 ± 0.037
$e_t j \gamma$	0.210 ± 0.030	0.129 ± 0.035	0.339 ± 0.046
$e_l^* j \gamma$	0.057 ± 0.018	0.097 ± 0.043	0.154 ± 0.047
Totals:	1.267 ± 0.048	0.547 ± 0.058	1.814 ± 0.075

Table 8.2: Backgrounds to $e_t e_l \gamma$ due to jet misidentification. Errors are purely statistical.

The kinematic distributions of the background are shown in figure 8.2. In terms of the photon transverse momentum, the background can be parameterized by an exponential function with a linear tail:

$$\frac{dN}{dp_T} = \exp(a_0 + a_1 p_T) + b_0 + b_1 p_T.$$

The best fit values are $a_0 = 0.684$, $a_1 = -9.46 \times 10^{-2}$, $b_0 = 2.72 \times 10^{-3}$, and $b_1 = -1.71 \times 10^{-5}$, where the background is measured in units of events per 5 GeV p_T bin. Statistical (fit) uncertainties are negligible compared to the systematic normalization uncertainties in this case. The majority (about 65%) of the background falls near M_Z with respect to dielectron mass, which supports the hypothesis that the background is mainly due to $Z + j$ production.

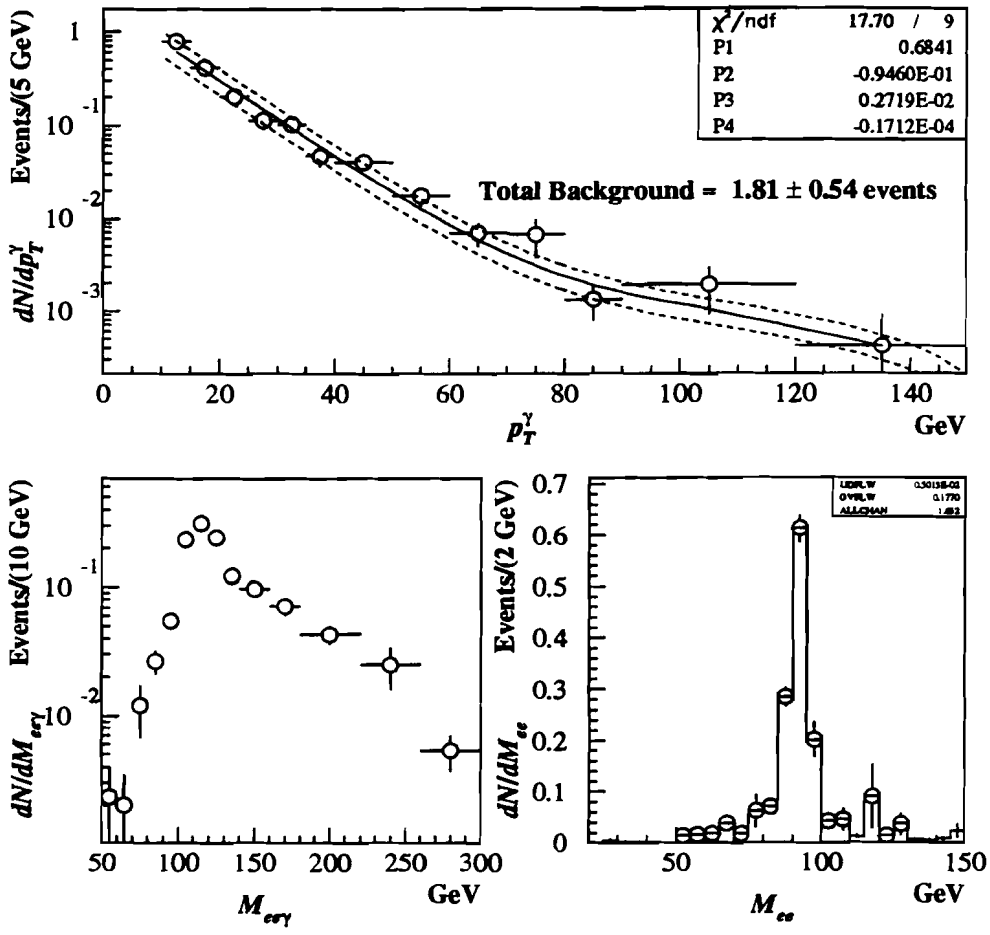

Figure 8.2: Background distributions in terms of photon transverse momentum, three body ($ee\gamma$) invariant mass, and dielectron invariant mass. The solid line indicates the best fit and the dotted lines indicate the 1σ combined systematic and statistical errors on the background.

8.2 Other Sources of $ee\gamma X$

The processes shown in figures 2.2 and 2.3 can result in the $\tau^+\tau^-\gamma$ final state as well as the $e^+e^-\gamma$ final state. Subsequent decays of the tau leptons into

electrons can result in a final state which would satisfy the inclusive $e_t e_l \gamma$ selection requirements. In other words, the reaction

$$p\bar{p} \rightarrow \tau^+\tau^-\gamma \rightarrow e^-e^+\gamma\nu_e\nu_\tau\bar{\nu}_e\bar{\nu}_\tau$$

is an irreducible background to the direct production process $p\bar{p} \rightarrow e^+e^-\gamma$ (assuming such contributions are not included in the definition of the signal). There are additional contributions from diagrams in which the final state photon originates from one of the final state cascade electrons, i.e.,

$$p\bar{p} \rightarrow \tau^+\tau^- \rightarrow e^-e^+\gamma\nu_\tau\nu_e\bar{\nu}_e\bar{\nu}_\tau.$$

Since the branching ratio for $\tau \rightarrow e\nu\bar{\nu}$ decay is about 17% [43], the $\tau\tau\gamma$ contribution to the $ee\gamma$ signal is bounded by $0.17^2 \approx 3\%$. However, electrons from tau lepton decay tend to have less momentum those produced directly (since the neutrinos must acquire some of the parent tau energy), so events with indirectly produced electrons are less likely to satisfy kinematic selection requirements than events with directly produced electrons.

Although cross section calculations which account for all possible diagrams for contributions to $ee\gamma$ from tau lepton decay have not yet been completed, existing partial calculations can be used to place an upper bound on such contributions. To this end, the PYTHIA Monte Carlo generator [77] was used to generate Z/γ^* and SM $Z\gamma$ production events. In each case, the Z bosons were allowed to decay to electrons both directly and indirectly through τ cascade decays. Figure 8.3a shows

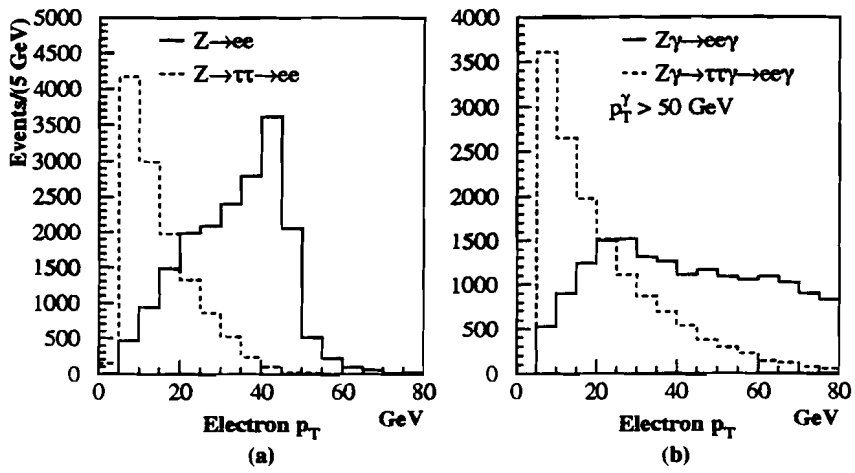

Figure 8.3: (a) Transverse momentum distribution of both prompt and decay electrons in $p\bar{p} \to Z \to \ell^+\ell^l$. (b) The same distributions for $Z\gamma$ production with the restriction that $p_T^\gamma > 50$ Gev/c.

the resulting electron transverse momentum distributions for Z production. The prompt electrons exhibit the familiar Jacobian peak, while the cascade electrons have a much softer distribution concentrated below 25 GeV. Using the parametric simulation described in chapter 7, the relative kinematic/geometric acceptance for the two samples is estimated to be about 2%. As might be expected, the relative acceptance does not differ appreciably for SM $Z\gamma$ production in the range $10 < p_T^\gamma < 20$ GeV. In practice, the relative acceptance for $\tau\tau\gamma \to ee\gamma$ (and $\tau\tau \to ee\gamma$) in the low-p_T^γ range will be much lower due to the large radiative decay contribution in this range. (Recall that the leptons from radiative decays tend to be softer than for $Z\gamma$ production.) In contrast to the low-p_T^γ range, the $Z\gamma$ production contributions

dominate at high-p_T^γ. In this case, the relative acceptance is expected to rise since the leptons originate from a high-p_T Z boson and have correspondingly higher transverse momenta than in the low-p_T^γ range. As can be seen in figure 8.3b, the cascade electron spectrum is still restricted mainly to the region below 25 GeV, even for $p_T^\gamma > 50$ GeV, so the kinematic acceptance for such processes is quite low. Detailed simulations yield

$$\frac{\mathcal{A}_{\tau\tau\gamma\to ee\gamma}}{\mathcal{A}_{ee\gamma}} \approx 6\% \tag{8.1}$$

for $p_T^\gamma > 50$ GeV, assuming SM $Z\gamma$ production. Although this is three times higher than in the low-p_T^γ range, the overall contribution to the $ee\gamma$ signal is quite small when branching ratios are included. The fractional background is thus bounded by $3\% \times 6\% = 0.2\%$ and is negligible compared to the $(15 \pm 5)\%$ background due to misidentified jets.

If electrons are misidentified as photons, processes such as

$$p\bar{p} \to W^\pm ZX \to e^\pm \nu e^+ e^- X$$

and

$$p\bar{p} \to ZZ(\gamma^*\gamma^*)X \to e^+e^-e^+e^-X$$

can contribute to the inclusive $ee\gamma$ signal. Although the cross sections for such processes are relatively small, these backgrounds are concentrated at higher p_T than the jet backgrounds and therefore might be expected to better mimic signals of $Z\gamma$ interactions. Since the hit counting requirement is about 95% efficient for electrons,

the fraction of eee events in which at least one electron is misidentified as a photon is about $(1 - 0.95^3) = 0.14$, and the fraction of $eeee$ events in which one or more electrons are misidentified as a photon is about 0.19.

The backgrounds due to associated WZ/ZZ production were estimated using the PYTHIA [77] event generator and the parametric detector simulation described previously. For WZ production, the estimated background is 0.011 ± 0.001 events. The p_T spectrum of the misidentified electron is shown in figure 8.4 along with the background due to misidentified jets. The jet background is seen to dominate the WZ background by more than a factor of 50 over the whole p_T^γ range. Given the size of the jet background, the $ee\gamma$ background from WZ production is insignificant and is ignored. The estimated background due to $ZZ \rightarrow eeee$ is less than half of the WZ background, so it is negligible as well.

Finally, backgrounds from multi-boson production, such as $W\gamma\gamma$ $Z\gamma\gamma$, and $WZ\gamma$ are negligible due to the small cross sections for such processes. The total background is therefore approximately equal to the background due to misidentified jets:

$$\boxed{B_{ee\gamma} = 1.81 \pm 0.54 \text{ events}} \tag{8.2}$$

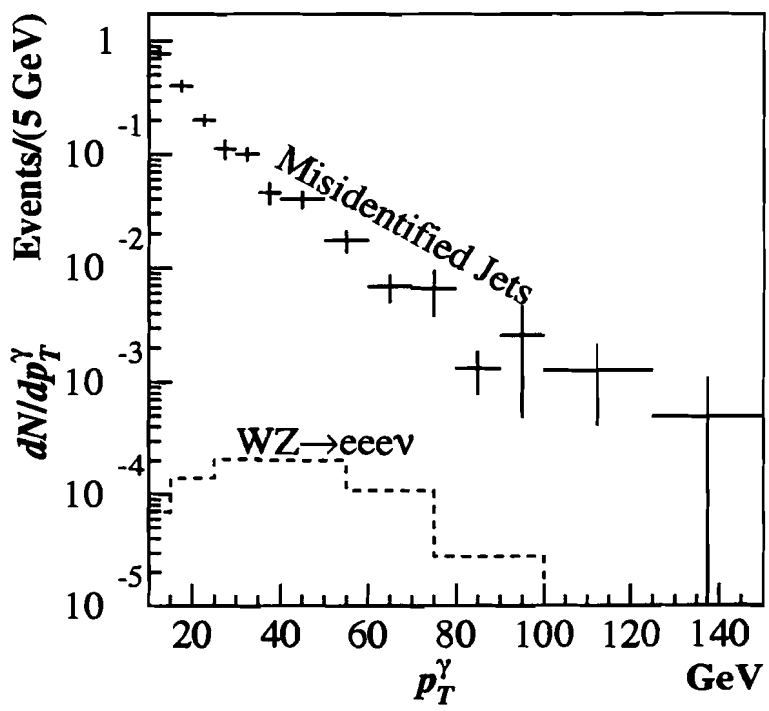

Figure 8.4: Background distributions in terms of photon transverse momentum for $WZ \rightarrow eee\nu$ and jets.

Chapter 9

Results

The efficiency and background estimates from the previous chapters allow for quantitative comparisons between theoretical predictions and the data. In the sections that follow, the observed event yields and candidate kinematics are compared with Standard Model predictions, and limits are placed on both $ZZ\gamma$ and $Z\gamma\gamma$ couplings using both the overall number of observed events and the photon transverse momentum distribution of the candidates.

9.1 Comparisons with Standard Model Predictions

Before attempting to place limits on the $ZZ\gamma$ and $Z\gamma\gamma$ couplings, it is instructive to compared the observed events to predictions of the Standard Model

(which corresponds to $h_i \equiv 0$). If the estimated background is subtracted from the number of observed candidates, the resulting "measured signal" is $12.2^{+4.8}_{-3.7} \pm 0.5$ events. The first (asymmetric) error corresponds to the 68% confidence level interval for 14 events using Poisson statistics, and the second error represents the uncertainty arising from background subtraction. The measured signal is in excellent agreement with the Standard Model prediction of 12.1 ± 1.2 events. Table 9.1 summarizes the theoretically predicted event yield, the expected number of background events, and the observed number of events.

Number of observed $ee\gamma$ events, $N_{\rm obs}$	14
Estimated number of background events, $B_{ee\gamma}$	1.81 ± 0.54
Number of observed signal events, $S_{ee\gamma}$	$12.2^{+4.8}_{-3.7} \pm 0.5$
Number of predicted signal events, $S^{\rm SM}_{\rm pred}$	12.1 ± 1.2

Table 9.1: Summary of the $ee\gamma$ counting experiment.

The same information can be expressed in terms of cross sections. If one assumes that the cross section not included in the phase space defined by table 2.2 is negligible, the predicted SM total $ee\gamma$ cross section is 2.78 ± 0.17 pb, where the uncertainty is due to pdf choice. The overall SM detection efficiency obtained from simulation is $(4.93 \pm 0.32)\%$,[1] where the uncertainty of 6.4% is obtained from table 7.2 without the pdf choice or luminosity contributions. Therefore, the measured

[1]The SM geometric/kinematic acceptance $\mathcal{A}$ was estimated to be 14.9%, and the identification efficiency $\epsilon_{\rm ID}$ was estimated to be 33.0%.

cross section is

$$\boxed{\sigma_{ee\gamma} = \frac{S_{ee\gamma}}{\epsilon\mathcal{L}} = 2.78^{+1.10}_{-0.84} \pm 0.36 \text{ pb}} \tag{9.1}$$

where the luminosity error has been included in the total systematic uncertainty. Specifically, the systematic uncertainty is given by

$$(\delta\sigma)^2 = \frac{[\delta(B_{ee\gamma})]^2}{(\epsilon\mathcal{L})^2} + \frac{S^2_{ee\gamma}}{(\epsilon\mathcal{L})^2}\frac{[\delta(\epsilon\mathcal{L})]^2}{(\epsilon\mathcal{L})^2}$$

with $\delta(B_{ee\gamma}) = 0.54$ events and $\delta(\epsilon\mathcal{L})/\epsilon\mathcal{L} = 8.3\%$. The measured cross section is in excellent agreement with the Standard Model prediction. It should also be noted that the uncertainty of the cross section measurement is dominated by the statistical uncertainty; about ten times more data are needed before the statistical and systematic uncertainties are expected to be of comparable size.

Figure 9.1 shows the photon transverse momentum distribution for the candidate events along with the background estimate and SM predictions. Two candidates are observed with $p_T^\gamma \approx 75$ GeV and a dielectron mass near the Z boson mass. (c.f. table A.1) These events are quite remarkable and have been scrutinized in detail [78]. Assuming SM $ee\gamma$ production, 0.331 ± 0.038 events are expected for $p_T^\gamma > 60$ GeV (including background), so the probability of observing 2 or more such events is

$$P(N \geq 2) = 1 - e^{-0.331}(1 + 0.331) = (4 \pm 1)\%$$

where the 1% uncertainty reflects the sensitivity of $P(N \geq 2)$ to the uncertainty in the event yield prediction. Although this probability is small, it is large enough to

allow these events to be reasonably interpreted as a statistical fluctuation of either SM $Z\gamma$ production or background.

In contrast to the photon spectrum, the dielectron invariant mass distribution of the $ee\gamma$ candidates matches the SM prediction very closely. This is shown in figure 9.2. The ratio of production events ($m_{ee} \approx M_Z$) to radiative decay events ($m_{ee} < M_Z$) is also consistent with the Standard Model prediction. In particular, 5 candidates satisfy the kinematic criteria of table 9.2 which are meant to select events with on-shell Z bosons in the final state. The Standard Model signal prediction is 4.5 ± 0.5 events, and the background estimate is 1.1 ± 0.3 events, so a total of 5.5 ± 0.6 production events are expected. It should also be noted that the signal-to-background ratio is *lower* for the production events alone than for the entire $ee\gamma$ sample since the major background source to $ee\gamma$ is $Z + j$ production, which is kinematically similar to $Z\gamma$ production.

Dielectron invariant mass:	$83 < m_{ee} < 98$ GeV
Dielectron-photon invariant mass:	$m_{ee\gamma} > 105$ GeV

Table 9.2: Kinematic criteria used to select $Z\gamma$ production events.

As is shown in, figure 9.3, the dielectron-photon invariant mass distribution of the candidates closely matches the SM prediction except for the two events at $m_{ee\gamma} \approx 200$ GeV. These are the same two events with $p_T^\gamma \approx 75$ GeV.

The correlations between the photon transverse momentum, dielectron invariant mass, and dielectron-photon invariant mass for the candidates is shown in figure 9.4. A cluster of events is observed with $p_T^\gamma < 30$ GeV, $m_{ee} < 85$ GeV, and $m_{ee\gamma} \approx 91$ GeV which is consistent with radiative decay. The kinematic regions bounded by the dielectron mass requirement of 9.2 are indicated with dotted lines.

Finally, the photon transverse momentum distribution of the 5 $Z\gamma$ production candidates is shown in figure 9.5 along with the Standard Model predictions and background estimate. The two events with $p_T^\gamma \approx 75$ GeV survive the additional cuts of table 9.2 and are included. However, as was noted previously, the total number of production events is in excellent agreement with the SM prediction of 5.5 ± 0.6 events.

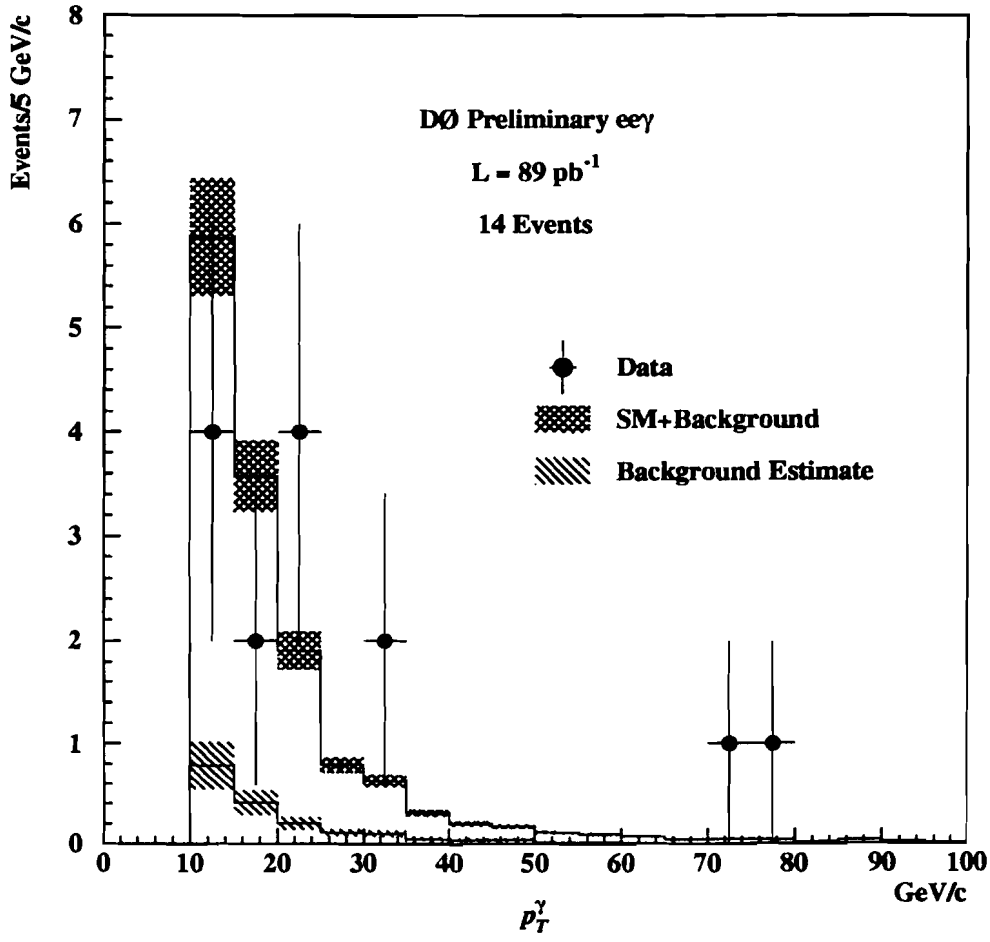

Figure 9.1: Distribution of photon transverse momenta for $ee\gamma$ candidates.

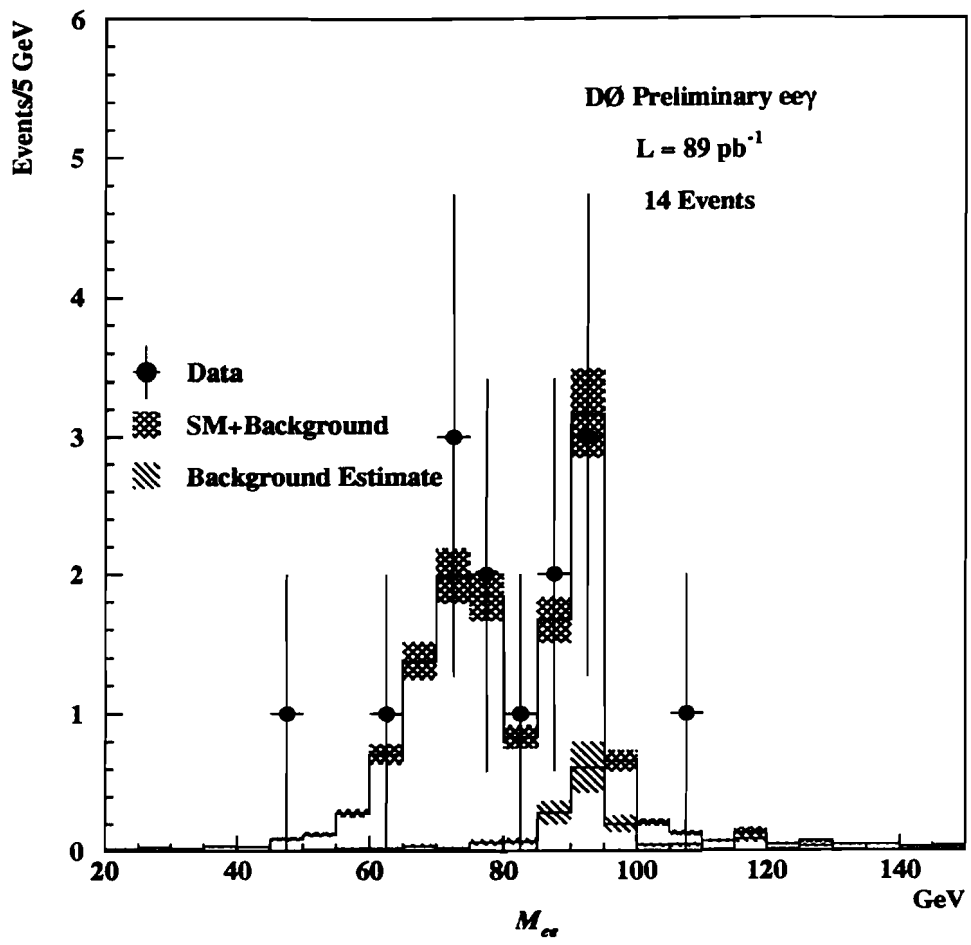

Figure 9.2: Dielectron invariant mass distribution for $ee\gamma$ candidates.

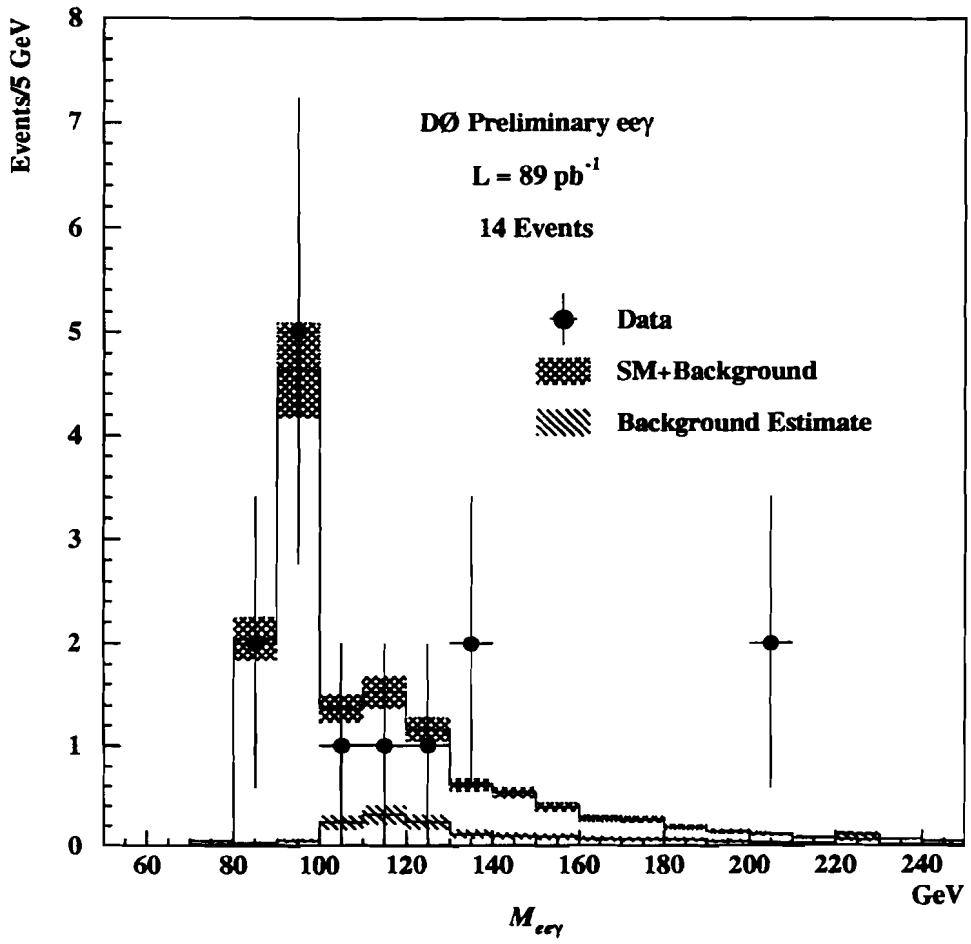

Figure 9.3: Dielectron-photon invariant mass distribution for $ee\gamma$ candidates.

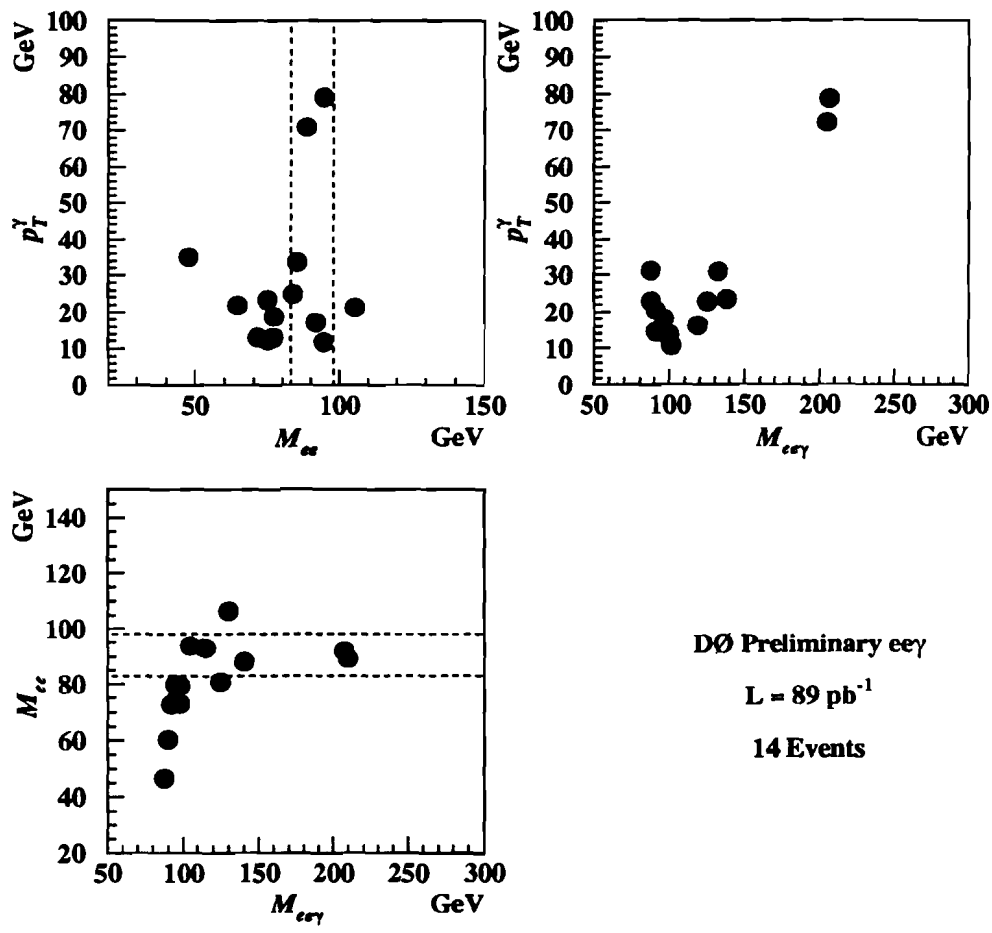

Figure 9.4: Correlations of p_T^γ, m_{ee}, and $m_{ee\gamma}$ for the $ee\gamma$ candidates. The dotted lines indicate regions where $m_{ee} \approx M_Z$, which is characteristic of $Z\gamma$ production.

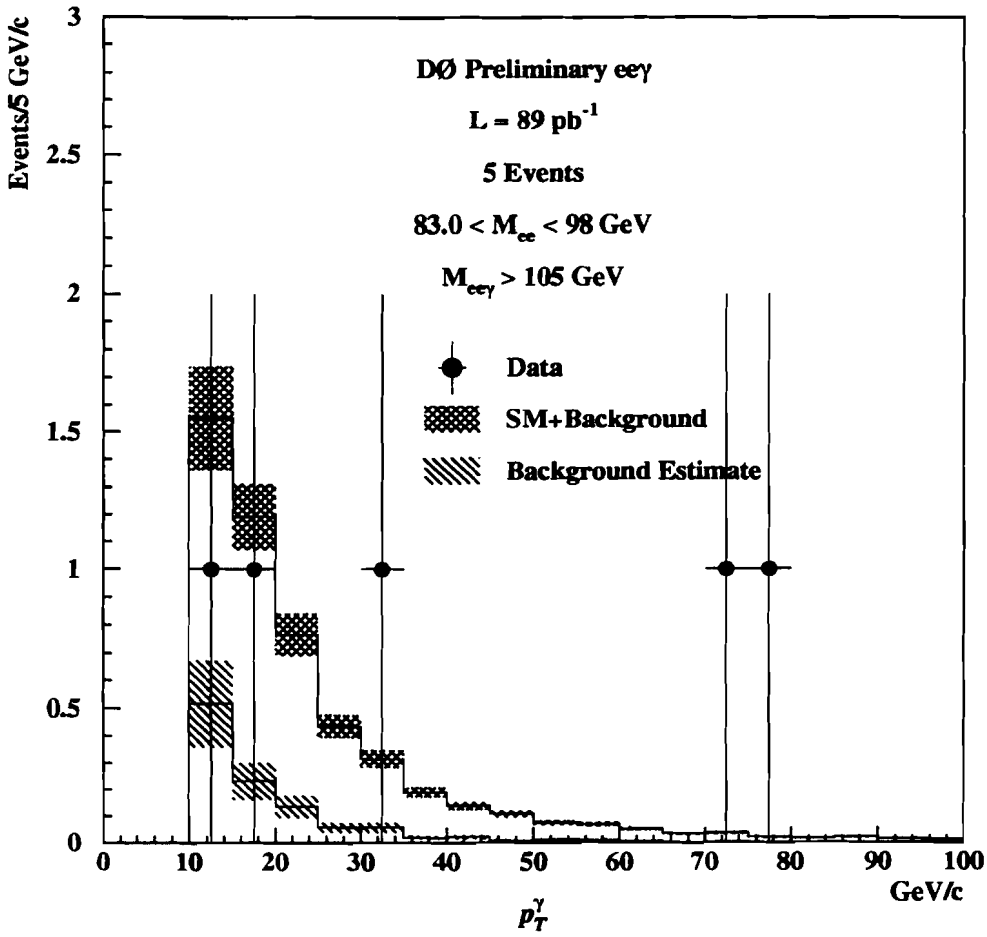

Figure 9.5: Distribution of photon transverse momenta for $Z\gamma \rightarrow ee\gamma$ candidates.

9.2 Coupling Limits from the Counting Experiment

As was discussed in section 2.4, the presence of $Z\gamma$ interactions is expected to result in an excess of $ee\gamma$ events above the Standard Model prediction. Therefore, the absence of such an excess can be used to place limits on $ZZ\gamma$ and $Z\gamma\gamma$ couplings.

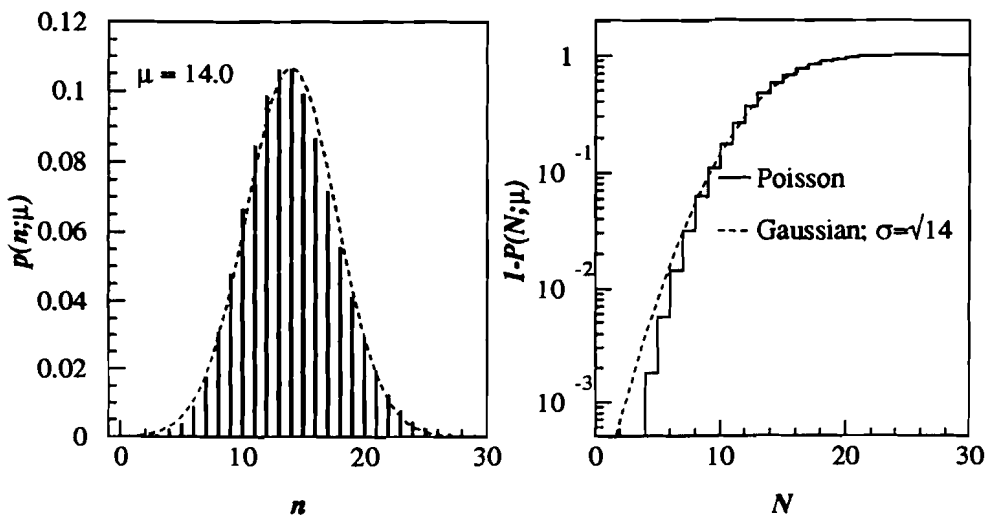

Figure 9.6: Comparison of Poisson and Gaussian probability densities in which the average number of expected events is 14.0. Also shown are the cumulative probabilities for observing greater than N events. candidates.

The total number of expected (and observed) $ee\gamma$ events is sufficiently large (14), that the Poisson distribution which describes the expected number of events can be approximated by a Gaussian distribution. Figure 9.6 shows Poisson and

Gaussian probability densities for a mean of $\mu = 14.0$ events. The agreement observed between the two distributions can be expressed as the approximation

$$\frac{e^{-\mu}\mu^n}{n!} \approx \frac{1}{\sigma\sqrt{2\pi}} e^{-(n-\mu)^2/2\sigma^2}$$

where $\sigma \equiv \sqrt{\mu}$. For the purposes of setting limits on $Z\gamma$ couplings, the quantity of interest is the probability integral, denoted $P(N;\mu)$, which is the cumulative probability of observing N or fewer events for a given μ. This probability is also shown in figure 9.6 for the case of Poisson and Gaussian probability densities. The Gaussian approximation is accurate in the region of interest in which $N > \mu$ and

$$P(N;\mu) \equiv \sum_{n=0}^{N} \frac{e^{-\mu}\mu^n}{n!} \approx \frac{1}{\sigma\sqrt{2\pi}} \int_{n=0}^{N} e^{-(n-\mu)^2/2\sigma^2} dn$$

This can be written more compactly by expressing the integral in terms of the complementary error function, which is defined by

$$\mathrm{erfc}(x) \equiv \frac{2}{\sqrt{\pi}} \int_x^{\infty} e^{-t^2} dt$$

and is easily evaluated using standard numerical library routines. Thus, the probability of observing N or fewer events for a given mean number of events μ is

$$P(N;\mu) = 1 - \frac{1}{2}\mathrm{erfc}\left(\frac{N-\mu}{\sigma\sqrt{2}}\right) \tag{9.2}$$

The approximation $\sigma = \sqrt{\mu}$ accounts for statistical fluctuations only, and the width of the Gaussian probability density must be adjusted to account for systematic

uncertainties associated with the mean number of expected events μ.[2] The predicted mean number of events is given by

$$\mu = \mu_s + \mu_b \tag{9.3}$$

where $\mu_s = \mathcal{L}\epsilon\sigma_{ee\gamma}$ is the expected number of signal events and $\mu_b = B_{ee\gamma}$ is the expected number of background events. Thus, the appropriate Gaussian variance which accounts for the systematic uncertainties in μ_s and μ_b is

$$\sigma^2 = \underbrace{\mu}_{\text{stat}} + \underbrace{\sigma_s^2 + \sigma_b^2}_{\text{sys}} \tag{9.4}$$

where σ_s and σ_b represent the systematic normalization uncertainties associated with the predicted number of signal and background events, respectively. As was discussed in section 7.4 and chapter 8, these uncertainties are estimated to be

$$\sigma_s/s = 10\% \tag{9.5}$$

and

$$\sigma_b = 0.54 \text{ events.} \tag{9.6}$$

Thus, the Gaussian describing the Standard Model prediction (including background) has $\mu = 13.9$ events and $\sigma = 3.5$ events.

Equations 9.2–9.6 provide a means of calculating the probability of observing fewer than N events for given values of $ZZ\gamma$ or $Z\gamma\gamma$ coupling strengths. In order

[2]The fact that the probability density $p(n;\mu)$ remains Gaussian is a consequence of the fact that the convolution of two (or more) Gaussians is itself a Gaussian. If the systematic uncertainties are not assumed to be Gaussian, this is not the case, and more complicated methods must be used.

to sufficiently determine $P(N; h_{30}^Z, h_{40}^Z)$, knowledge of μ_s is required for many values of h_{30}^Z and h_{40}^Z. The computational burden is reduced by constructing a 3×3 grid of μ_s values which are obtained from the parametric simulation for $h_{30}^Z = \{0, \pm 3.0\}$ and $h_{30}^Z = \{0, \pm 1.0\}$. Biquadratic interpolation [79, 80] is then used to evaluate μ_s for given values of h_{30}^Z and h_{40}^Z. (The accuracy of this technique was verified by comparing interpolated values with those obtained directly from the simulation at various points in the h_{30}^Z-h_{40}^Z plane.) The resulting function $P(N = 14; h_{30}^Z, h_{40}^Z)$ is shown in figure 9.7. Since the number of events observed (14) is very near the predicted SM mean (13.9), $P(14; h_{30}^Z, h_{40}^Z) \approx 0.5$ for $h_{30}^Z = h_{40}^Z = 0$, which implies that fewer than 14 events would be expected in about half of a large ensemble of similar experiments. The probability of observing 14 or fewer events decreases for non-zero values of h_{30}^Z and h_{40}^Z due to the increased cross section relative to the SM case.

Limits on the couplings h_{30}^Z and h_{40}^Z at confidence level α are obtained from the locus of points described by $1 - \alpha = P(14; h_{30}^Z, h_{40}^Z)$. For example, the 95% CL limits are obtained from the contour of figure 9.7 at which $P(14; h_{30}^Z, h_{40}^Z) = 0.05$. Such contours are shown in figure 9.8 for $\alpha = 0.68$ and $\alpha = 0.95$. The 95% CL limit contour results in tighter limits than are obtained from unitarity (consistency) considerations alone; this is the motivation for the choice of $\Lambda = 500$ GeV.

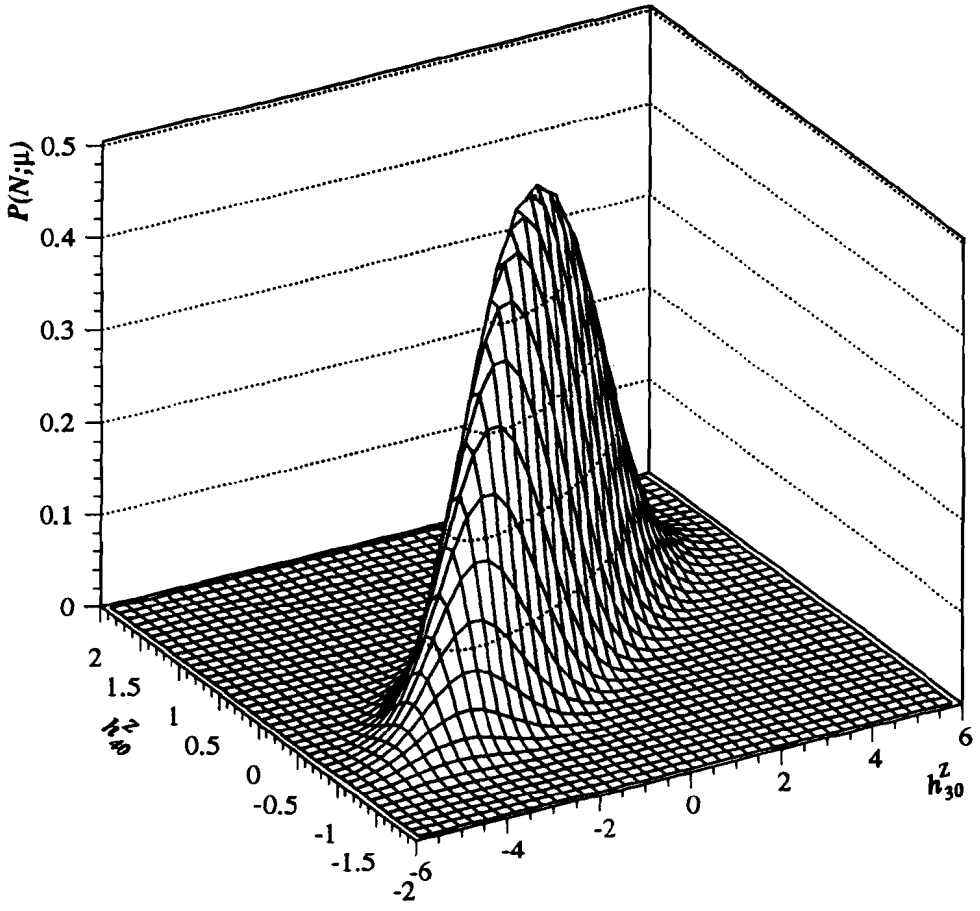

Figure 9.7: Probability of observing 14 or fewer events as a function of h_{30}^Z and h_{40}^Z for $\Lambda = 500$ GeV.

The maximum excursions of the confidence region yield the 95% CL correlated limits (which account for interference effects):

$$|h_{30}^Z| < 4.0$$

$$|h_{40}^Z| < 1.05$$

for $h^{\gamma}_{1...4} \equiv 0$ and $h^{Z}_{1,2} \equiv 0$. Also of interest are the uncorrelated limits in which interference effects are negated by restricting one of the couplings to its SM value of zero. (This situation is somewhat contrived since undiscovered phenomena are expected to result in more than one non-zero coupling.) For these cases, the limits are:

$$\boxed{\begin{array}{c} |h^{Z}_{30}| < 2.3;\ h^{Z}_{40} \equiv 0 \\ |h^{Z}_{40}| < 0.60;\ h^{Z}_{30} \equiv 0 \end{array}}$$

The same approach can be used to set limits on the $Z\gamma\gamma$ couplings with the assumption that the $ZZ\gamma$ couplings are zero. Figure 9.9 shows the resulting 68% and 95% CL limit contours for h^{γ}_{30} and h^{γ}_{40}. The correlated limits are

$$\boxed{\begin{array}{c} |h^{\gamma}_{30}| < 4.3 \\ |h^{\gamma}_{40}| < 1.10 \end{array}}$$

and the uncorrelated limits are

$$\boxed{\begin{array}{c} |h^{\gamma}_{30}| < 2.4;\ h^{\gamma}_{40} \equiv 0 \\ |h^{\gamma}_{40}| < 0.62;\ h^{\gamma}_{30} \equiv 0 \end{array}}$$

for $h^{Z}_{1...4} \equiv 0$ and $h^{\gamma}_{1,2} \equiv 0$.

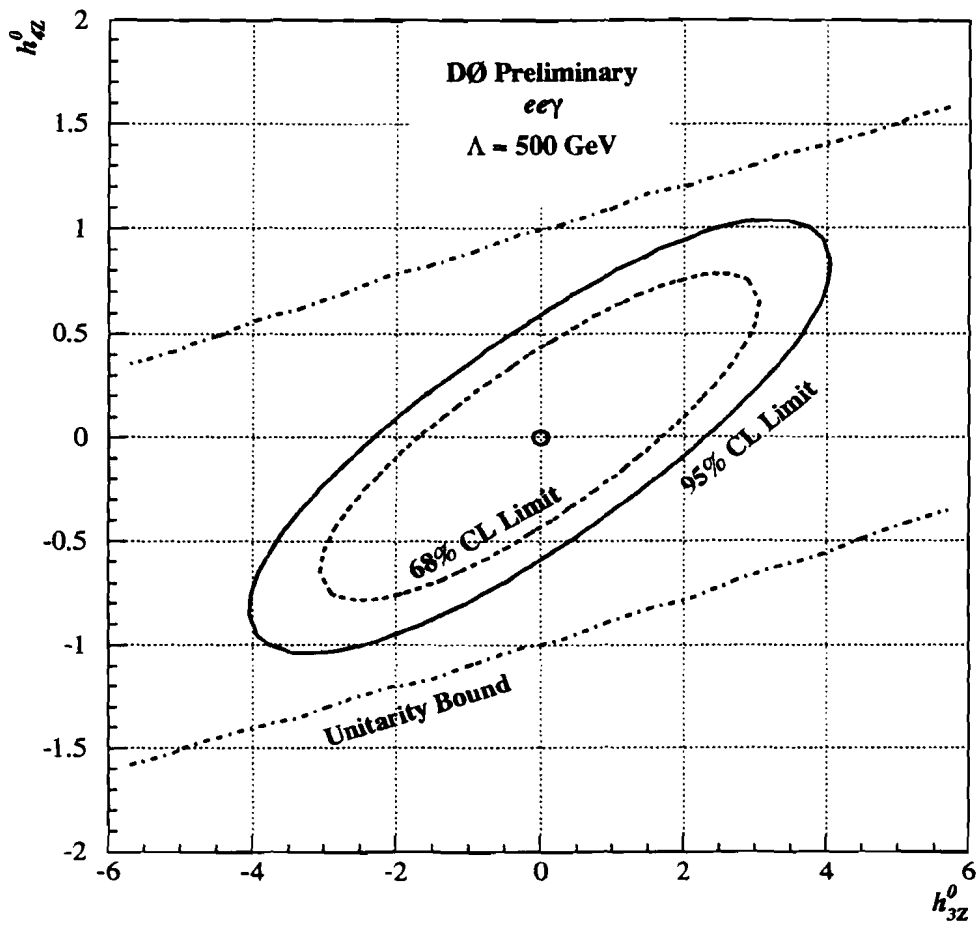

Figure 9.8: Correlated limits on h^Z_{30} and h^Z_{40} for $\Lambda = 500$ GeV from the event counting technique.

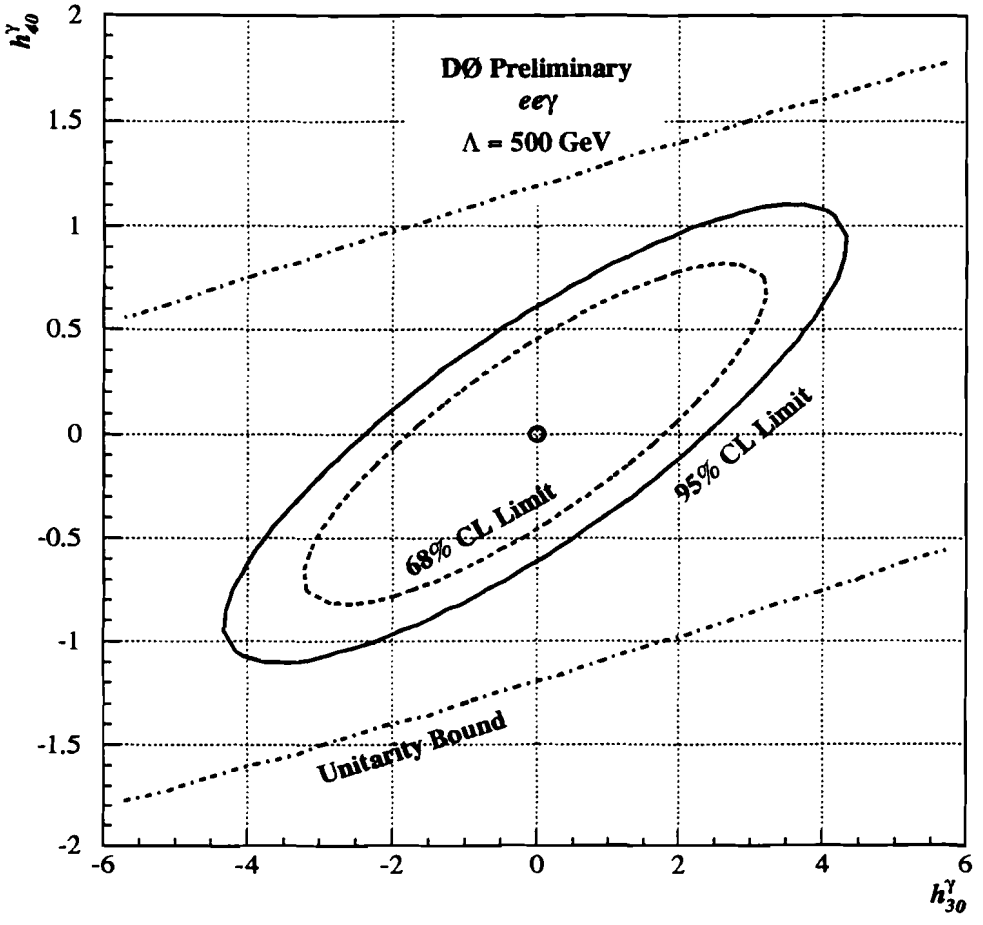

Figure 9.9: Correlated limits on h^{γ}_{30} and h^{γ}_{40} for $\Lambda = 500$ GeV from the event counting technique.

9.3 Coupling Limits from the Photon Spectrum

As was discussed previously, the cross section enhancement due to $Z\gamma$ interactions is confined to regions of phase space which are only minimally accessible through Standard Model processes. This fact can be exploited to place limits on the $ZZ\gamma$ and $Z\gamma\gamma$ couplings which are expected to be more stringent than those obtained from the counting technique of the previous section. In this study, this is accomplished by a maximum likelihood fit to the photon transverse momentum distribution. Since the overall number of events is rather small, an unbinned likelihood fit is used. Otherwise, the final results are somewhat dependent on the choice of bin boundaries. It should also be noted that the limited number of events observed in this experiment precludes a fit using two or more kinematic variables simultaneously, but future experiments will likely collect enough data to warrant multivariate kinematic fitting.

Within a given ensemble of events, the probability of observing an event with a photon of transverse momentum p_T^0 is

$$p(p_T^0) = \frac{1}{\sigma}\frac{d\sigma}{dp_T}|_{p_T^0}$$

where $d\sigma/dp_T$ is the differential cross section describing the ensemble. In practice, it is convenient to work with predicted event yields, in terms of which the probability

of obtaining an individual event is

$$p(p_T^0) = \frac{1}{\mu}\frac{d\mu}{dp_T}|_{p_T^0}$$

where μ is the sum of predicted signal and background given by equation 9.3. The likelihood of observing a given ensemble of n events is then

$$L = \frac{e^{-\mu}\mu^n}{n!} \times \prod_{i=1}^{n} \frac{1}{\mu}\frac{d\mu}{dp_T}|_{p_T^i}$$

where the first (Poisson) term accounts for the observed sample size and the second term accounts for the shape of the p_T^γ distribution. However, μ (and $d\mu/dp_T$) are not known precisely, so the appropriate likelihood is constructed by summing over all allowed values of μ and weighting each term by the probability that it deviates from its central value.[3] With this modification, the likelihood function becomes

$$L = \frac{\int_0^\infty d\mu_s \int_0^\infty d\mu_b \mathcal{G}(\mu_s,\sigma_s)\mathcal{G}(\mu_b,\sigma_b)\frac{e^{-(\mu_s+\mu_b)}}{n!}\prod_{i=1}^{n}\frac{d(\mu_s+\mu_b)}{dp_T}|_{p_T^i}}{\int_0^\infty \mathcal{G}(\mu_s,\sigma_s)d\mu_s \int_0^\infty \mathcal{G}(\mu_b,\sigma_b)d\mu_b} \tag{9.7}$$

where the μ^n normalization term has been explicitly cancelled by the $\prod_n 1/\mu$ shape term. The functions $\mathcal{G}(\mu_s,\sigma_s)$ and $\mathcal{G}(\mu_b,\sigma_b)$ are the Gaussian probability densities describing the predicted signal and estimated background, i.e.,

$$\mathcal{G}(\mu_i,\sigma_i) = \frac{1}{\sigma\sqrt{2\pi}}\exp\left[\frac{-(\mu_i-\hat{\mu}_i)^2}{2\sigma^2}\right] \tag{9.8}$$

where $\hat{\mu}_i$ is the estimated value of μ_i and σ_i is the uncertainty associated with the estimate. As was discussed previously, the normalization uncertainties for the signal

[3] Equation 9.7 can also be derived from Bayes' Theorem assuming Gaussian prior probabilities for the signal and background.

and background were estimated to be 10% and 30%, respectively. The lower limits of integration in equation 9.7 exclude the physically unacceptable region in which the estimated signal or background is negative. In this study, it turns out that the possible unphysical contributions to the integrals are minimal, and the denominator of (9.7) is very nearly unity. It should be noted that the likelihood function becomes more complicated if more than one channel is used due to correlated uncertainties. Appendix C contains the likelihood function which is extended to include the $\mu\mu\gamma$ case.

The likelihood function can be computed using the cross section interpolation method described previously along with Monte Carlo integration techniques.[4] Figure 9.10 shows the result of this calculation for various values of the couplings h_{30}^Z and h_{40}^Z. The presence of the two high-p_T^γ events causes the maxima not to coincide with the Standard Model case of $h_{30}^Z = h_{40}^Z = 0$; non-SM values are preferred by the fit. The fact that there are two (roughly equal) maxima is a consequence of the fact that this experiment is insensitive to the sign of the product $h_{30}^Z h_{40}^Z = 0$. Although non-zero coupling values are preferred by the fit, the question of statistical significance still remains to be answered.

In the limit of large statistics, it is expected that the likelihood function is described by a multidimensional Gaussian[43, 81, 82]. For example, if the fit contains

[4] As is discussed in appendix C, the number of integrals increases if, for example, the $\mu\mu\gamma$ results are included. In such cases, Monte Carlo integration is the preferred method for numerical evaluation of the likelihood function due to its characteristic $1\sqrt{N}$ convergence. This approach also eliminates the cumbersome multiply-nested loops characteristic of other methods.

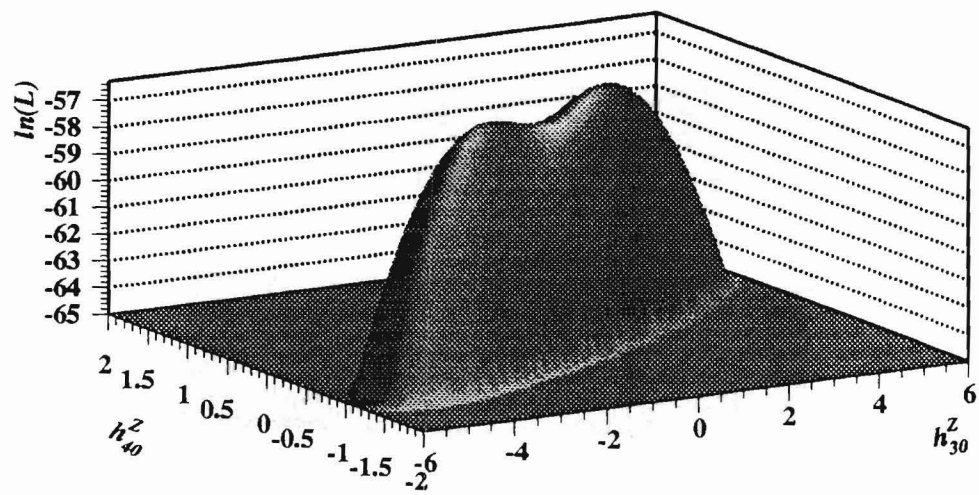

Figure 9.10: Plot of $\ln(L)$ as computed from equation 9.7 over the h^Z_{30}-h^Z_{40} plane for $\Lambda = 500$ GeV.

two free parameters, the likelihood function should approximate a two-dimensional Gaussian for large numbers of events.

The limits corresponding to confidence level α are correspond to the boundaries delimiting the region in which the upper integral of the likelihood function is equal to α. The integral of a multidimensional Gaussian is related to the χ^2 probability density integral for n degrees of freedom:

$$\alpha = \int_0^{2\delta} e^{-t/2}\, t^{n/2-1}\, dt$$

where the number of degrees of freedom n is equal to the number of free parameters in the fit. The parameter δ describes, in units of $\ln(L)$, the level of the surface below

the likelihood maximum which forms the boundary of the region with volume α. In other words, the confidence region corresponds to the intersection of the likelihood function and the surface of constant likelihood described by $\ln(L)_{\max} - \delta$. The dimensionality of these surfaces is governed by the number of free parameters in the fit. Some generally useful values of δ are given in table 9.3 [81, 82].

δ	No. Free Parameters	Confidence Level
1.00	1	0.683
1.00	2	0.392
2.30	2	0.683
1.92	2	0.853
1.92	1	0.950
3.00	2	0.950

Table 9.3: Values of δ for confidence regions with one or two parameter fits.

Therefore, the 95% CL limits on the couplings h_{30}^Z and h_{40}^Z are given by the contour defined by $\ln(L) = \ln(L)_{\max} - 3.00$. The resulting confidence region is shown in figure 9.11 along with the preferred values of the fit. The limits are not significantly improved over the event counting technique — this is due to the two high-p_T^γ events. Figure 9.12 shows the analogous 95% CL limits for the *CP*-even $Z\gamma\gamma$ couplings using the maximum likelihood technique. The correlated coupling limits for both pairs of $ZZ\gamma$ and $Z\gamma\gamma$ couplings obtained from this method are:

$\lvert h_{30}^{Z}\rvert < 4.1$
$\lvert h_{40}^{Z}\rvert < 0.90$
$\lvert h_{30}^{\gamma}\rvert < 4.5$
$\lvert h_{40}^{\gamma}\rvert < 1.00$

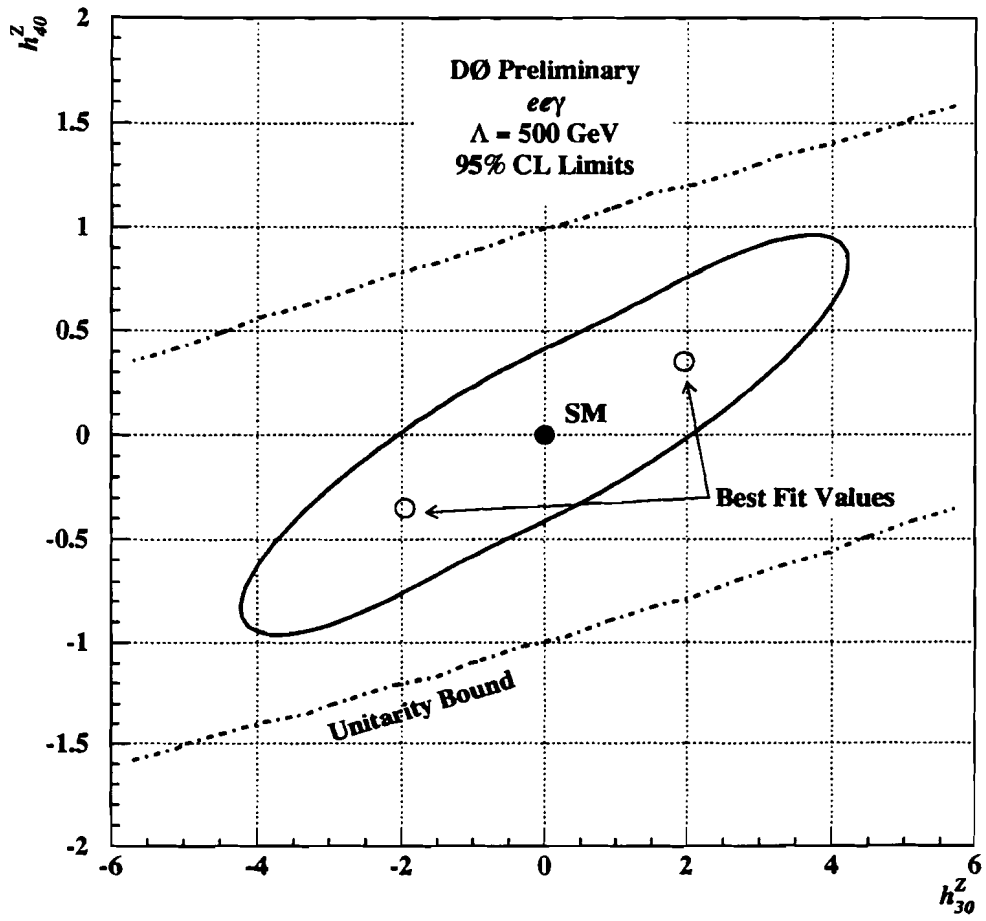

Figure 9.11: Correlated limits on h_{30}^{Z} and h_{40}^{Z} for $\Lambda = 500$ GeV from the fit to the photon transverse momentum spectrum.

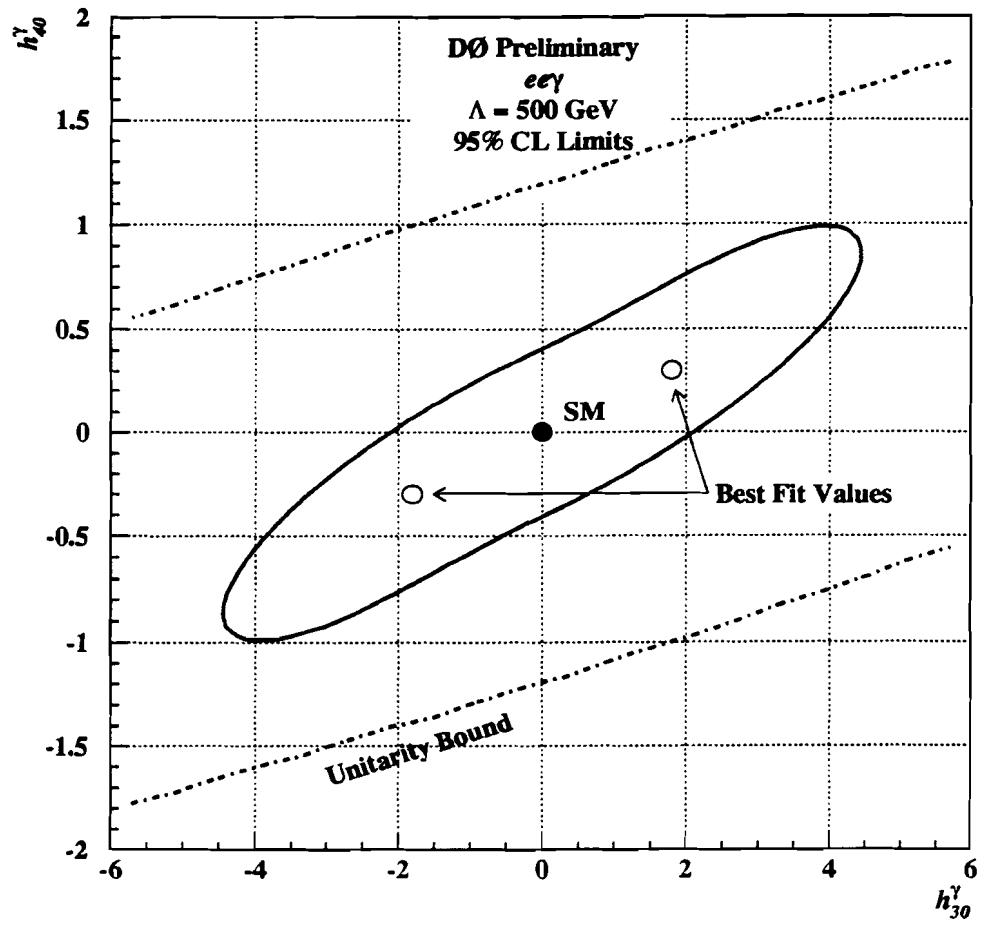

Figure 9.12: Correlated limits on h^{γ}_{30} and h^{γ}_{40} for $\Lambda = 500$ GeV from the fit to the photon transverse momentum spectrum.

The uncorrelated coupling limits are obtained from the one-dimensional likelihood functions in which only one coupling is allowed to vary from its SM value, i.e., all other couplings are constraint to zero. Figure 9.13 shows the constrained likelihood functions for the four individual couplings considered previously. The 95%

limits are found from the intersection of the intersection of the likelihood functions and the line of constant likelihood described by $\ln(L)_{\max} - 2.30$ (See table 9.3). The resulting constrained limits are:

$\lvert h_{30}^{Z}\rvert < 1.90$
$\lvert h_{40}^{Z}\rvert < 0.38$
$\lvert h_{30}^{\gamma}\rvert < 1.95$
$\lvert h_{40}^{\gamma}\rvert < 0.38$

Finally, it is interesting to extract coupling limits from the p_T^{γ} distribution of the five $Z\gamma$ production candidates alone. (c.f. table 9.2 and figure 9.5.) In this case, the small number of events causes the normalization term of (9.7) to dominate the likelihood. The 95% confidence region is shown in figure 9.14 for the h_{30}^{Z} and h_{40}^{Z} couplings. Although the coupling limits obtained with the production events are more stringent than those from partial wave unitarity, they are less stringent than those obtained from the entire $ee\gamma$ sample due to the smaller number of events.

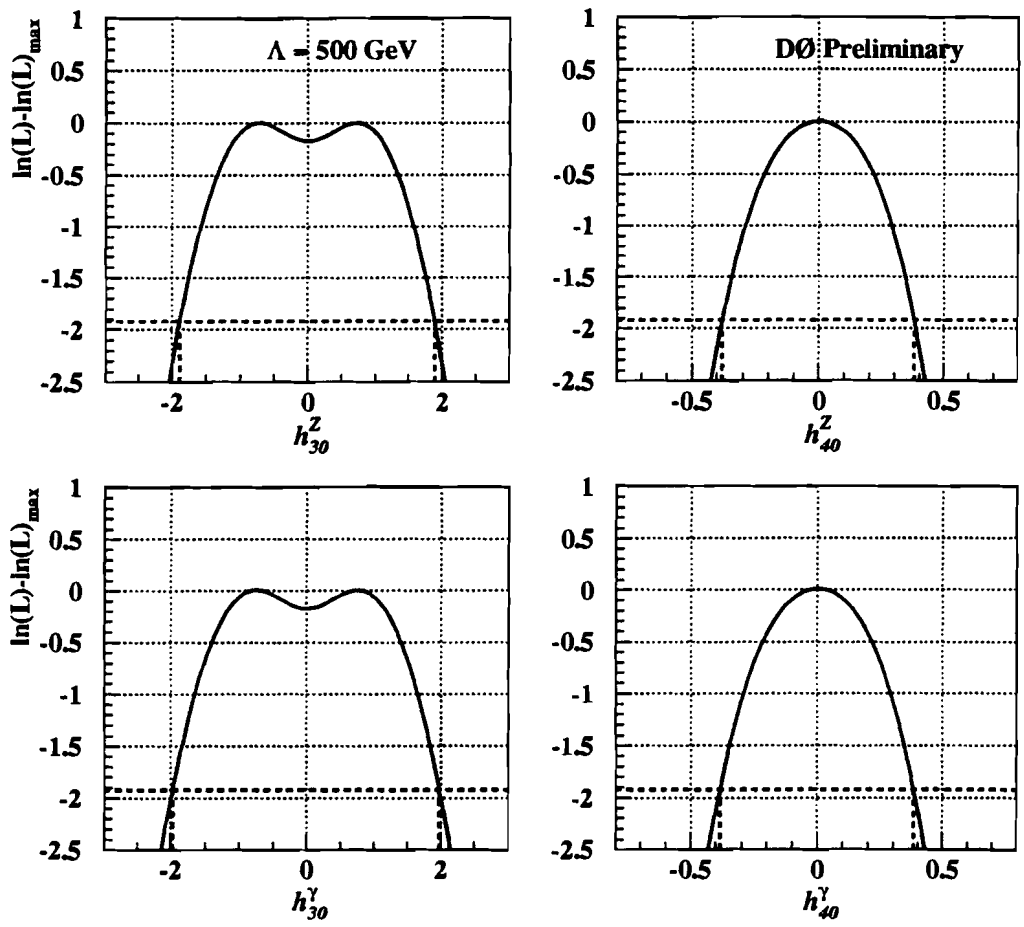

Figure 9.13: Likelihood functions in which only one variable is allowed to deviate from its SM value for $\Lambda = 500$ GeV. The resulting uncorrelated 95% CL limits on h^Z_{30}, h^Z_{40}, h^γ_{30}, and h^γ_{40} are indicated by the dotted lines.

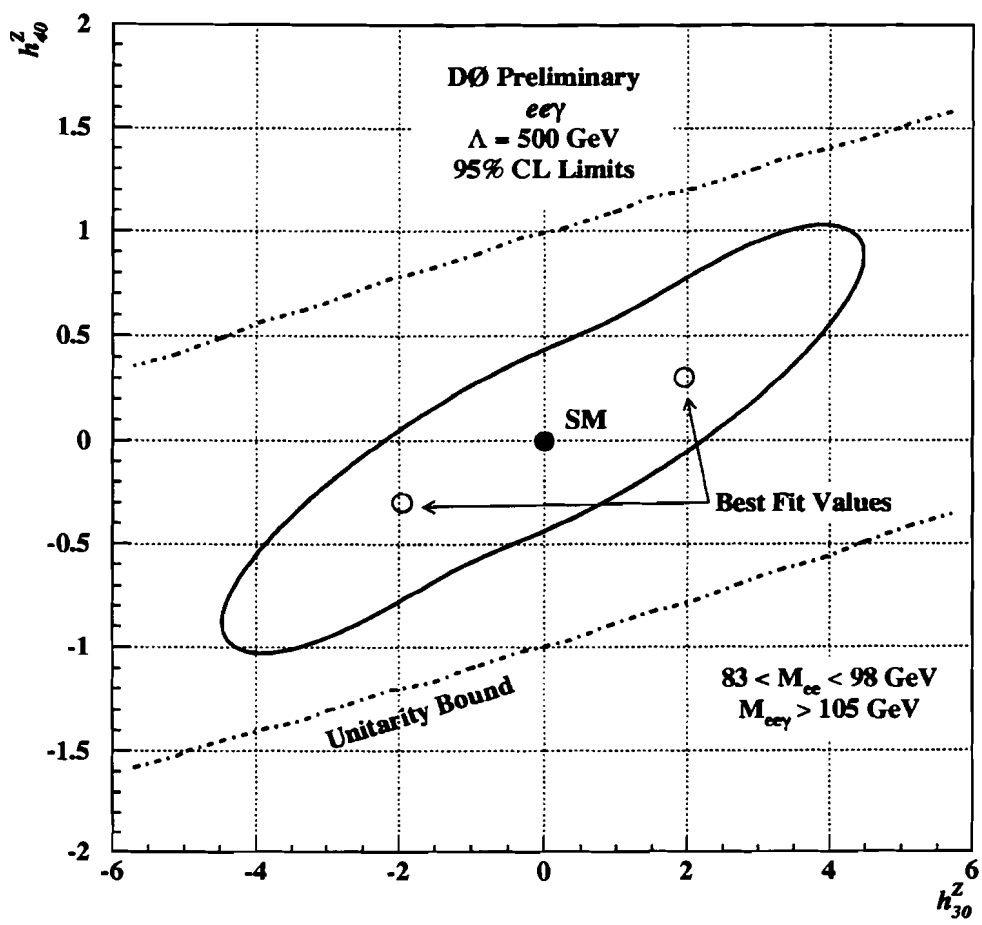

Figure 9.14: Correlated limits on h_{30}^Z and h_{40}^Z for $\Lambda = 500$ GeV from the fit to the photon transverse momentum spectrum using the five $Z\gamma$ production candidate events only.

Chapter 10

Conclusions

This study concludes with a summary of the results and a comparison with previous measurements. Prospects for probing the $ZZ\gamma$ and $Z\gamma\gamma$ vertices in future experiments are also discussed.

10.1 Summary

A search for interactions between the neutral Z and γ gauge bosons has been performed by studying the reaction $p\bar{p} \rightarrow ee\gamma X$ at $\sqrt{s} = 1.8$ TeV. The results of this search are presented in the context of a general framework in which the assumption of form-factor behavior of $Z\gamma$ interactions is necessary to maintain self-consistency. In this study, attention has been focused primarily on CP-even $ZZ\gamma$ and $Z\gamma\gamma$ couplings which are described by the parameters h_{30}^{Z}, h_{40}^{Z}, h_{30}^{γ}, and h_{40}^{γ}.

A form factor scale of 500 GeV is assumed. Form factor powers of $n = 3$ for h_{30}^Z and h_{30}^γ, and $n = 4$ for h_{40}^Z and h_{40}^γ are assumed as well. With these assumptions, limits on the h_{i0} are extracted from the data using a fit to the photon transverse momentum distribution of the observed candidates. These limits are summarized in table 10.1 below.

Limit	Constraints
$\lvert h_{30}^Z\rvert < 4.1$ $\lvert h_{40}^Z\rvert < 0.90$	$h_{30}^\gamma = h_{40}^\gamma = 0$
$\lvert h_{30}^\gamma\rvert < 4.5$ $\lvert h_{40}^\gamma\rvert < 1.00$	$h_{30}^Z = h_{40}^Z = 0$
$\lvert h_{30}^Z\rvert < 1.90$ $\lvert h_{40}^Z\rvert < 0.38$	$h_{30}^\gamma = h_{40}^\gamma = h_{40}^Z = 0$ $h_{30}^\gamma = h_{40}^\gamma = h_{30}^Z = 0$
$\lvert h_{30}^\gamma\rvert < 1.95$ $\lvert h_{40}^\gamma\rvert < 0.38$	$h_{30}^Z = h_{40}^Z = h_{40}^\gamma = 0$ $h_{30}^Z = h_{40}^Z = h_{30}^\gamma = 0$

Table 10.1: Summary of coupling limits obtained from a fits to the photon p_T spectrum assuming $n_3 = 3$, $n_3 = 4$, and $\Lambda = 500$ GeV.

A total of 14 $ee\gamma$ were observed in a data set corresponding to an integrated luminosity of 89 pb^{-1}. This is in excellent agreement with the SM predicted signal of 12.1 ± 1.2 events and an estimated background of 1.81 ± 0.54 events. The background is dominated by $Z +$ jets production with subsequent misidentification of the jet as a photon. Five of the candidates are kinematically consistent with $Z\gamma$ production, which is also in excellent agreement with the SM prediction of 4.5 ± 0.5 events and an estimated background of 1.1 ± 0.3 events. Of these five events, two are observed with

photon transverse momenta of approximately 75 GeV/c. Given the SM prediction and background estimate, the probability of observing two or more such events is $(4 \pm 1)\%$, which is sufficiently large to allow for a these events to be reasonably interpreted as a statistical fluctuation of SM $Z\gamma$ production or background.

10.2 Comparison with Previous Results

It is interesting to compare the measurements performed in this study to those obtained previously by the DØ experiment. Unfortunately, the comparison is complicated somewhat by the different conventions used to define the confidence regions. The run 1A coupling limits published previously correspond to $\delta = 1.92$, which imply a confidence level of 85%. (c.f. table 9.3) These limits are shown in figure 10.1 for the correlated pair of *CP*-even $ZZ\gamma$ couplings along with those obtained here for $\delta = 1.92$. As has been discussed previously, the coupling limits obtained from the present measurement are affected by the observation of two events with $p_T^\gamma \approx 75$ GeV, and the confidence regions for the two measurements do not scale as might be expected from luminosity considerations. In fact, the two confidence regions cover nearly the same area in the (h_{30}^Z, h_{40}^Z) parameter space. Also visible in figure 10.1 is the distortion of the run 1B confidence region from the ideal elliptical shape; this is caused by the high-p_T^γ events in the data sample.

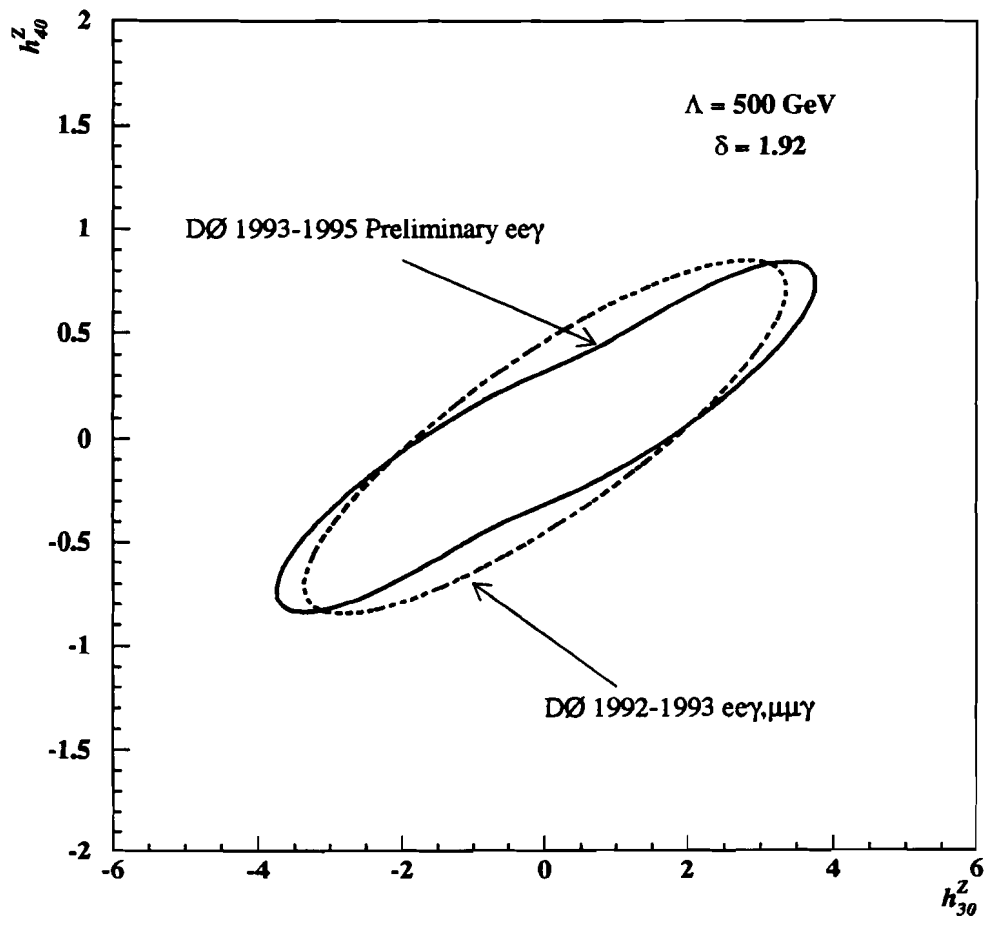

Figure 10.1: Correlated limits on the coupling pairs (h^Z_{30}, h^Z_{40}) and $(h^\gamma_{30}, h^\gamma_{40})$ for $\Lambda = 500$ GeV from the fit to the photon transverse momentum distribution. The confidence region corresponds to $\delta = 1.92$ (85% CL).

10.3 Future Prospects

Since the results of this analysis are greatly influenced by the available amount of data, it is interesting to examine how they might be improved if more data were collected. In the future, increased luminosities are expected to make feasible the exclusive study of $Z\gamma$ production (c.f. table 9.2). Assuming the two high-p_T^γ events are statistical fluctuations of SM $Z\gamma$ production, the data are expected to be described by the SM and background shape shown in figure 9.5. About 60 such events are expected for an integrated luminosity of 1000 pb^{-1} (= 1 fb^{-1}). The projected coupling limits can be obtained by randomly generating 55 "events" from the double-hatched distribution in figure 9.5 and adding them to the five candidates observed in this analysis. As is shown in figure 10.2a, the resulting ensemble contains the original two high-p_T^γ events and an additional event with $p_T^\gamma = 111$ GeV. The background estimate can be obtained simply by scaling the estimate of this analysis by the luminosity ratio of 1000/89. The systematic errors are assumed to be the same as those used in this analysis.

The resulting coupling limits are shown in figure 10.2b. As might be expected, the influence of the events on the high-p_T^γ tail is diminished, and the confidence region is consequently reduced dramatically relative to that obtained in this study. The fact that the confidence region is well within the unitarity bounds indicates higher values of Λ can be probed as well. Additionally, the limits obtained in the

future are likely to be more stringent than those obtained by this exercise since the systematic uncertainties should decrease as more data become available. For example, with sufficient data, the photon conversion probability could be accurately measured using a large sample of radiative Z decay events. The data sample will also be increased through the addition of the $\mu^+\mu^-\gamma$ and possibly the $\nu\nu\gamma$ channels. Furthermore, detector upgrades are likely to improve efficiencies, so future event samples are likely to be larger than would be expected from luminosity increases alone.

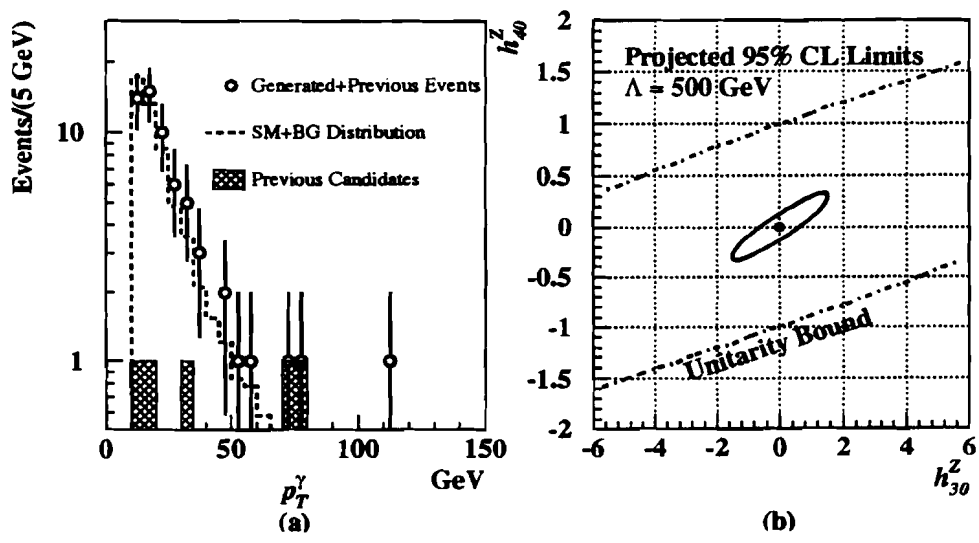

Figure 10.2: (a) Photon transverse momentum distribution for ensemble of $55+5 = 60$ events expected for an integrated luminosity of 1 fb^{-1}. (b) Correlated limits on the coupling pair (h_{30}^Z, h_{40}^Z) obtained from this sample.

As more data become available, it will be feasible to further constrain $Z\gamma$ couplings by multivariate kinematic fitting. For example, the $\cos\theta_\gamma^*$ or $\cos\theta_\ell^*$ distributions can be used to discriminate between s and t channel $Z\gamma$ production [23]. This is useful since SM $Z\gamma$ production takes place only in the t channel.

10.4 Final Remarks

The sensitivity of this analysis depends crucially on the rather small size of the event sample. Despite the observation of two $ee\gamma$ events which are relatively unlikely to result from Standard Model $Z\gamma$ production or background, this study finds no statistically significant evidence for new physical phenomena. As is the case with many statistically-limited measurements, more data are needed to unambiguously determine whether or not these events represent statistical fluctuations or physics beyond the Standard Model. Nevertheless, the work described here rules out gross deviations from the SM. In the future, increased amounts of data should make more sophisticated analysis methods feasible and provide a more sensitive means of probing the nature of gauge boson self-interactions.

Appendix A

Candidate Summaries

Table A.1 below lists the kinematic properties of all 14 $ee\gamma$ events. All energies are in units of GeV. The "type" denotes whether or not each electron had a matching track ("t") or hits only ("l"). Detailed properties of each event are given in the pages following table A.1.

Run	Event	p_T^γ	M_{ee}	$M_{ee\gamma}$	$\Delta\mathcal{R}_{e\gamma}^{\mathrm{Min}}$	Type
77306	4662	16.9	92.9	114.6	1.47	t, t
79096	15782	73.3	89.4	200.3	1.21	t, t
79218	980	75.2	91.7	202.5	2.78	t, l
82691	2862	22.5	106.0	134.4	0.94	t, l
85247	6893	31.1	47.5	87.9	2.02	t, t
87300	3011	20.3	62.2	89.5	1.18	t, t
87328	3190	23.1	70.8	94.8	1.75	t, t
88205	18408	10.9	70.8	94.2	1.22	t, t
88466	28114	12.9	74.1	91.7	0.84	t, t
89554	15108	14.1	76.6	92.8	0.89	t, t
90809	10313	19.6	77.3	93.0	1.39	t, l
91805	11407	34.7	89.6	139.6	2.25	t, l
92114	16551	20.4	82.8	120.1	1.42	t, t
92239	12054	13.8	90.1	105.8	1.64	t, l

Table A.1: Summary of candidate $ee\gamma$ event kinematics.

Run 77306 , Event 4662
DØRECO Vertices: z = 25.2 cm

Object	E_T	η	$\eta_{\rm det}$	ϕ	$E_{\rm EM}/E$	χ^2	$\mathcal{I}$	$s_{\rm trk}$	z_v	$N_{\rm hit}$
e_1	41.3	0.38	0.64	4.48	1.003	17.6	0.017	0.9	26.6	27
e_2	32.2	1.92	2.07	1.94	0.991	16.5	0.051	1.7	25.3	57
γ	16.9	1.60	1.75	0.51	0.994	33.2	0.044	-	-	16

Run 79096 , Event 15782
DØRECO Vertices: z = -28.2 cm

Object	E_T	η	$\eta_{\rm det}$	ϕ	$E_{\rm EM}/E$	χ^2	$\mathcal{I}$	$s_{\rm trk}$	z_v	$N_{\rm hit}$
e_1	29.6	-0.12	-0.45	5.24	0.998	11.8	0.008	1.2	-31.4	32
e_2	91.8	-0.45	-0.74	0.96	0.996	20.4	0.019	1.1	-31.1	31
γ	73.3	0.14	-0.20	4.06	0.956	75.9	0.086	-	-	0
j	13.1	1.92	1.78	2.30	0.407					
j	11.7	1.08	0.88	3.12	0.540					

Run 79218 , Event 980
DØRECO Vertices: z = -27.8 cm

Object	E_T	η	$\eta_{\rm det}$	ϕ	$E_{\rm EM}/E$	χ^2	$\mathcal{I}$	$s_{\rm trk}$	z_v	$N_{\rm hit}$
e_1	59.5	0.28	0.00	0.27	0.989	10.4	0.035	1.0	-26.2	28
e_2	37.8	1.76	1.64	1.38	0.990	149.9	0.033	-	-	48
γ	75.2	0.18	-0.10	3.77	0.961	49.5	0.053	-	-	2

Run 82691 , Event 2862
DØRECO Vertices: z = -2.3 cm

Object	E_T	η	$\eta_{\rm det}$	ϕ	$E_{\rm EM}/E$	χ^2	$\mathcal{I}$	$s_{\rm trk}$	z_v	$N_{\rm hit}$
e_1	40.8	-0.82	-0.86	5.55	0.965	54.5	0.074	2.5	-5.4	31
e_2	66.3	-0.27	-0.33	2.80	0.998	15.2	0.015	-	-	27
γ	22.5	0.03	-0.03	5.95	0.976	15.4	0.047	-	-	0

Run 85247 , Event 6893
DØRECO Vertices: z = 38.9, 11.4 cm

Object	E_T	η	$\eta_{\rm det}$	ϕ	$E_{\rm EM}/E$	χ^2	$\mathcal{I}$	$s_{\rm trk}$	z_v	$N_{\rm hit}$
e_1	29.6	-0.67	-0.29	4.10	1.000	20.2	0.063	1.5	39.6	34
e_2	25.1	-0.93	-0.60	2.03	1.011	34.6	-0.054	1.9	41.8	30
γ	31.1	-0.38	0.05	6.10	0.994	12.3	0.035	-	-	10

Run 87300 , Event 3011
DØRECO Vertices: z = -20.0 cm

Object	E_T	η	$\eta_{\rm det}$	ϕ	$E_{\rm EM}/E$	χ^2	$\mathcal{I}$	$s_{\rm trk}$	z_v	$N_{\rm hit}$
e_1	26.3	-1.97	-2.07	1.61	0.996	12.5	0.016	3.2	-18.4	75
e_2	39.2	-2.24	-2.35	4.18	0.992	10.7	0.034	1.6	-17.4	75
γ	20.3	-1.48	-1.58	0.53	0.985	19.5	0.018	-	-	6

Run 87328 , Event 3190
DØRECO Vertices: z = 50.9, 5.8 cm

Object	E_T	η	$\eta_{\rm det}$	ϕ	$E_{\rm EM}/E$	χ^2	$\mathcal{I}$	$s_{\rm trk}$	z_v	$N_{\rm hit}$
e_1	32.5	-0.51	-0.02	0.95	0.972	29.5	0.070	2.6	46.9	3
e_2	38.6	-0.28	0.23	4.34	0.988	13.7	0.035	1.6	51.5	30
γ	23.1	-0.94	-0.55	2.65	1.009	84.9	0.005	-	-	3
j	12.9	-1.79	-1.55	5.90	0.593					

Run 88205 , Event 18408
DØRECO Vertices: z = -0.8 cm

Object	E_T	η	$\eta_{\rm det}$	ϕ	$E_{\rm EM}/E$	χ^2	$\mathcal{I}$	$s_{\rm trk}$	z_v	$N_{\rm hit}$
e_1	32.4	-0.83	-0.87	5.32	0.991	22.3	0.035	1.4	-5.2	29
e_2	34.2	-1.59	-1.61	1.91	0.992	25.7	0.017	5.2	-12.8	40
γ	10.9	0.31	0.25	4.88	0.996	53.7	0.009	-	-	0

Run 88466 , Event 28114
DØRECO Vertices: z = -35.6, 27.6 cm

Object	E_T	η	$\eta_{\rm det}$	ϕ	$E_{\rm EM}/E$	χ^2	$\mathcal{I}$	$s_{\rm trk}$	z_v	$N_{\rm hit}$
e_1	32.7	-0.35	-0.07	5.75	0.991	12.7	0.072	1.0	26.4	30
e_2	35.2	0.50	0.74	2.68	0.981	38.4	0.046	1.4	28.6	31
γ	12.9	-0.89	-0.67	0.11	1.000	30.6	0.037	-	-	1

Run 89554 , Event 15108
DØRECO Vertices: z = 14.3 cm

Object	E_T	η	$\eta_{\rm det}$	ϕ	$E_{\rm EM}/E$	χ^2	$\mathcal{I}$	$s_{\rm trk}$	z_v	$N_{\rm hit}$
e_1	44.9	0.20	0.33	4.81	1.000	27.8	0.015	2.4	12.3	30
e_2	33.6	0.31	0.44	2.01	0.965	26.7	0.052	1.1	14.3	28
γ	14.1	0.42	0.54	1.13	0.983	9.5	0.051	-	-	6

Run 90809 , Event 10313
DØRECO Vertices: z = -5.3, 57.9 cm

Object	E_T	η	$\eta_{\rm det}$	ϕ	$E_{\rm EM}/E$	χ^2	$\mathcal{I}$	$s_{\rm trk}$	z_v	$N_{\rm hit}$
e_1	43.6	-0.45	-0.53	2.67	0.954	59.8	0.084	1.5	-8.3	31
e_2	30.2	0.34	0.26	6.15	0.990	22.6	0.070	-	-	45
γ	19.6	-0.12	-0.20	1.33	0.991	20.9	0.019	-	-	4
j	31.7	-0.10	-0.16	4.11	0.789					
j	24.1	-1.26	-1.29	0.03	0.433					

Run 91805 , Event 11407
DØRECO Vertices: z = 38.0, -2.5 cm

Object	E_T	η	$\eta_{\rm det}$	ϕ	$E_{\rm EM}/E$	χ^2	$\mathcal{I}$	$s_{\rm trk}$	z_v	$N_{\rm hit}$
e_1	38.9	-0.47	-0.03	1.82	0.982	17.3	0.028	0.5	41.2	28
e_2	30.2	1.29	1.52	6.07	0.996	13.8	0.022	-	-	66
γ	34.7	-0.50	-0.07	4.07	0.980	13.7	0.071	-	-	3

Run 92114 , Event 16551
DØRECO Vertices: z = -11.9, 33.0 cm

Object	E_T	η	$\eta_{\rm det}$	ϕ	$E_{\rm EM}/E$	χ^2	$\mathcal{I}$	$s_{\rm trk}$	z_v	$N_{\rm hit}$
e_1	33.3	-0.50	-0.57	2.57	0.988	10.7	0.057	2.0	-7.3	23
e_2	52.2	-0.54	-0.61	5.95	0.963	47.0	0.096	1.4	-11.8	33
γ	20.4	-1.83	-1.87	3.06	0.996	33.7	0.021	16.7	-	18

Run 92239 , Event 12054
DØRECO Vertices: z = 45.4 cm

Object	E_T	η	$\eta_{\rm det}$	ϕ	$E_{\rm EM}/E$	χ^2	$\mathcal{I}$	$s_{\rm trk}$	z_v	$N_{\rm hit}$
e_1	30.0	-1.85	-1.64	3.96	0.990	17.0	0.018	0.9	43.0	40
e_2	41.4	-0.31	0.15	1.41	0.990	22.3	0.086	-	-	25
γ	13.8	-1.02	-0.68	5.38	0.974	83.9	0.095	14.4	-	12

Appendix B

Measurement of $P_{j\to\gamma}$ and $P_{j\to e}$

B.1 Introduction

Background estimates to diboson production usually involve counting the jets in inclusive W or Z samples and weighting by the probabilities that a jet is misidentified as a photon or electron to get the estimated number of fake signal events. Previous studies [83, 84, 85, 86] with earlier DØ data indicate that the probability for a jet to fake an electron or photon is approximately 10^{-3}, and that the probabilities measured from data roughly agree with the predictions of the ISAJET Monte Carlo [2]. The purpose of this section is to detail the measurement of the jet misidentification rates for the selection criteria used in this analysis.

At momenta greater than 10 GeV/c, the granularity of the DØ electromagnetic calorimeter is not sufficient to distinguish between isolated $\pi^0/\eta \to \gamma\gamma$ and

single photons on the basis of shower shape [1] (H-Matrix) or isolation requirements. Therefore, when a jet fragments principally into an isolated π^0 or η, it will be misidentified as an electron or photon. Since the DØ detector has a non-magnetic tracking system, fake electrons will be produced when one or both of the photons convert to an e^+e^- pair via pair production. Similarly, a soft charged hadron from the jet associated with the leading meson or underlying event near the photon pair will also result in the misidentification of a jet as an electron. (The overlapping hadron must be of low energy for the jet to fake an electron. Otherwise, the prospective fake electron or photon would fail the isolation requirement.)

In this study, fake probabilities are measured from data collected by the single jet filters `jet_20_noL0`, `jet_30`, `jet_50`, `jet_80`, and `jet_max`. To first order, the fake probability is given by the ratio of the jet population to the electron or photon population:

$$P_{j\to\gamma} \approx N_\gamma / N_j \tag{B.1}$$

and

$$P_{j\to e} \approx N_e / N_j \tag{B.2}$$

where N_γ, N_e, and N_j are the numbers of photons, electrons, and jets, respectively. The jets, electrons, and photons are all restricted to the same region of phase space. Generally, these ratios are E_T-dependent, so they must be calculated by bins in E_T.

[1] The H-Matrix χ^2 is dominated by the *transverse* shower shape. Direct photon analyses generally discriminate between single photons and overlapping $\gamma\gamma$ by the *longitudinal* shower shape.

Any angular dependence is assumed to be accounted for by calculating the ratios for the CC and EC separately. It should be noted that the E_T dependences of these ratios are also affected by trigger requirements and the presence of real photons in the data due to direct photon production. Sections 3 and 4 describe how these effects are removed.

B.2 Data Sample and Event Selection

To quantify the frequency at which jets are misidentified as electrons or photons, it is necessary to obtain a data sample which is free of genuine electrons or photons. Since QCD jet cross sections greatly exceed the cross sections for processes which yield authentic electrons or photons, data collected with jet (calorimeter tower) triggers have almost no real[2] e/γ components and are appropriate for this measurement. Therefore, the data used for this study are collected from the `jet_20`, `jet_30`, `jet_50`, `jet_85`, and `jet_max` filters from runs 87804 through 93115. These runs correspond to trigger list versions 10.2 through 10.6. All data were reconstructed with RECO versions 12.15 through 12.20. Jets are reconstructed with a cone size of $\mathcal{R} = 0.5$ and are subject to the following additional requirements:

- $E_T > 10$ GeV
- $|\eta_{\rm det}| < 1.0$ or $1.5 < |\eta_{\rm det}| < 2.5$

[2]Electrons from charm or bottom semileptonic decays are eliminated by the isolation requirement. However, direct photon production is expected to contaminate the sample.

- $\phi < 1.1$ or $\phi > 1.2$
- Coarse Hadronic (CH) energy $< 40\%$ of total energy
- $E_1/E_2 < 10.0$, where E_1 and E_2 are the two highest energy cells in the cluster.

The first two cuts restrict the jets to the same kinematic phase space as electrons and photons. The ϕ cut eliminates objects caused by Main Ring activity, and the last two cuts remove contributions due to "hot cells" in the calorimeter. Finally, the missing transverse energy is required to be less than 20 GeV to eliminate $W \rightarrow e\nu$ as a possible source of contamination.

Electrons and photons are identified using the criteria for e_t, e_l, and γ in table 4.1. The kinematic requirements are the same as those used for jets.

B.3 Trigger Bias

Since energy resolutions and corrections differ for hadronic and electromagnetic showers, it is necessary to impose kinematic requirements on the reconstructed objects to minimize trigger threshold bias on the ratios $P_{j\rightarrow\gamma}$ and $P_{j\rightarrow e}$. As shown schematically in figure B.1, an event will tend to trigger more often near the trigger threshold E_T^0 when the leading object is isolated from hadronic activity and contained primarily in the electromagnetic calorimeter. Consequently, the e/γ populations are inflated relative to jets near the trigger threshold, and the ratios $P_{j\rightarrow e}$

and $P_{j\to\gamma}$ exhibit trigger-induced bumps.

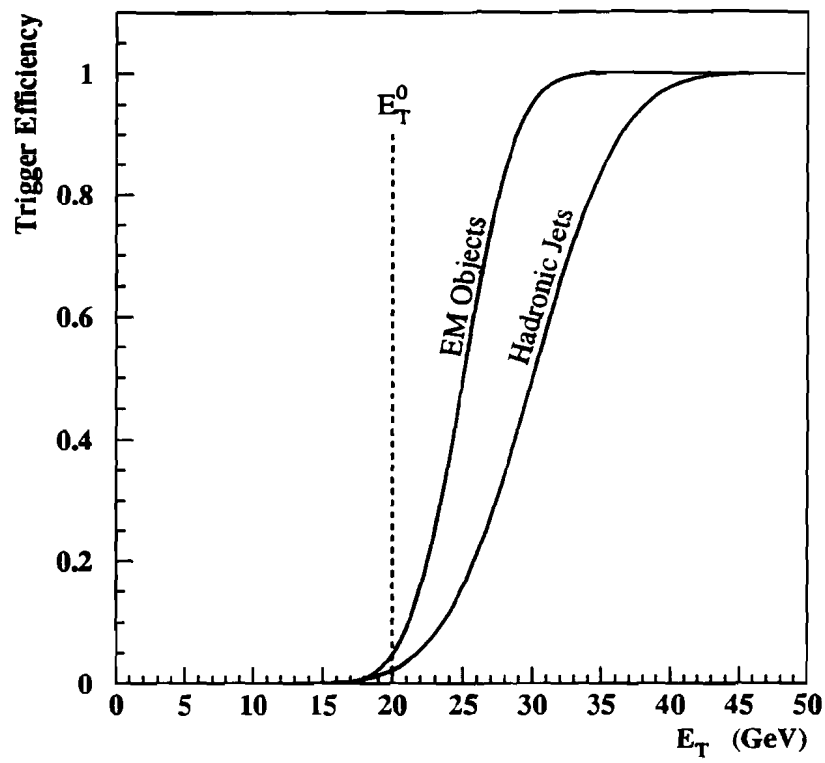

Figure B.1: Typical trigger efficiencies for electromagnetic and hadronic objects as a function of transverse energy. The efficiency at the trigger threshold E_T^0 is not 50% due to offline energy corrections.

To avoid these biases, events are rejected if the leading object has transverse energy less than a threshold $E_T^{\rm Min}$ associated with the L2 filter which the event satisfied. This threshold is chosen such that the trigger is fully efficient for both

electromagnetic and hadronic showers. Table B.1 summarizes the leading object transverse energy thresholds used in this measurement.

L2 filter	L1 E_T	L2 E_T	E_T^{Min}
jet_20	10	20	30
jet_30	15	30	50
jet_50	15	50	90
jet_85	35	85	150
jet_max	45	115	200

Table B.1: Summary of E_T thresholds used in measuring fake rates. Units are GeV.

Figures B.2 and B.3 show the jet and $e+\gamma$ spectra, respectively, after all cuts in this section have been imposed. The relative population differences as a function of E_T are due kinematic requirements as well as relative trigger prescales.

B.4 Direct Photon Subtraction

Since multijet cross sections are much larger than W/Z cross sections, it is expected that the sample mentioned previously would be composed nearly entirely of QCD jets, and that any electrons or photons identified in the sample would arise from misidentified jets. However, the cross section for direct photon production is relatively large, and it increases relative to the multijet cross section at high p_T. (This is due in part to the fact that the electroweak coupling strength, α, increases

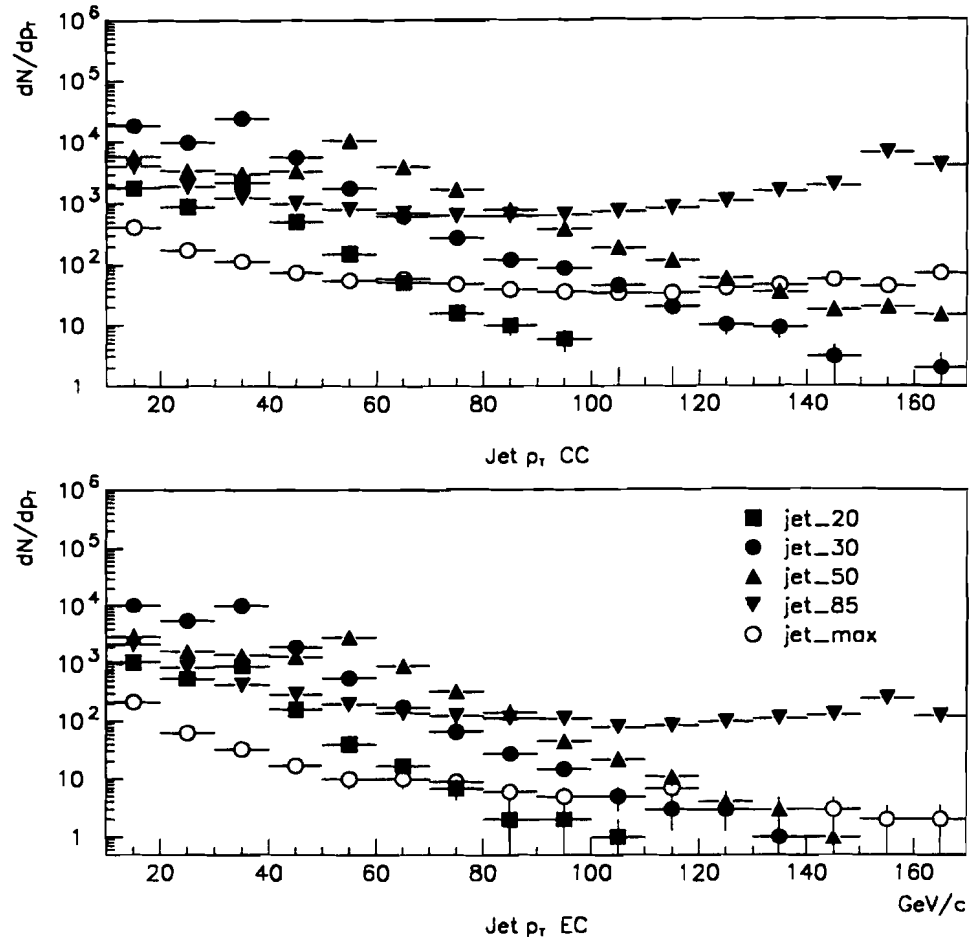

Figure B.2: Transverse energy distribution of jets in the multijet sample for the central (CC) region and forward (EC) regions for the various filters used in this study.

as q^2 increases, while the strong coupling strength, α_s, decreases.) Therefore, it is important to subtract the direct photon component out of the sample before forming the ratio $P_{j\to\gamma}$.

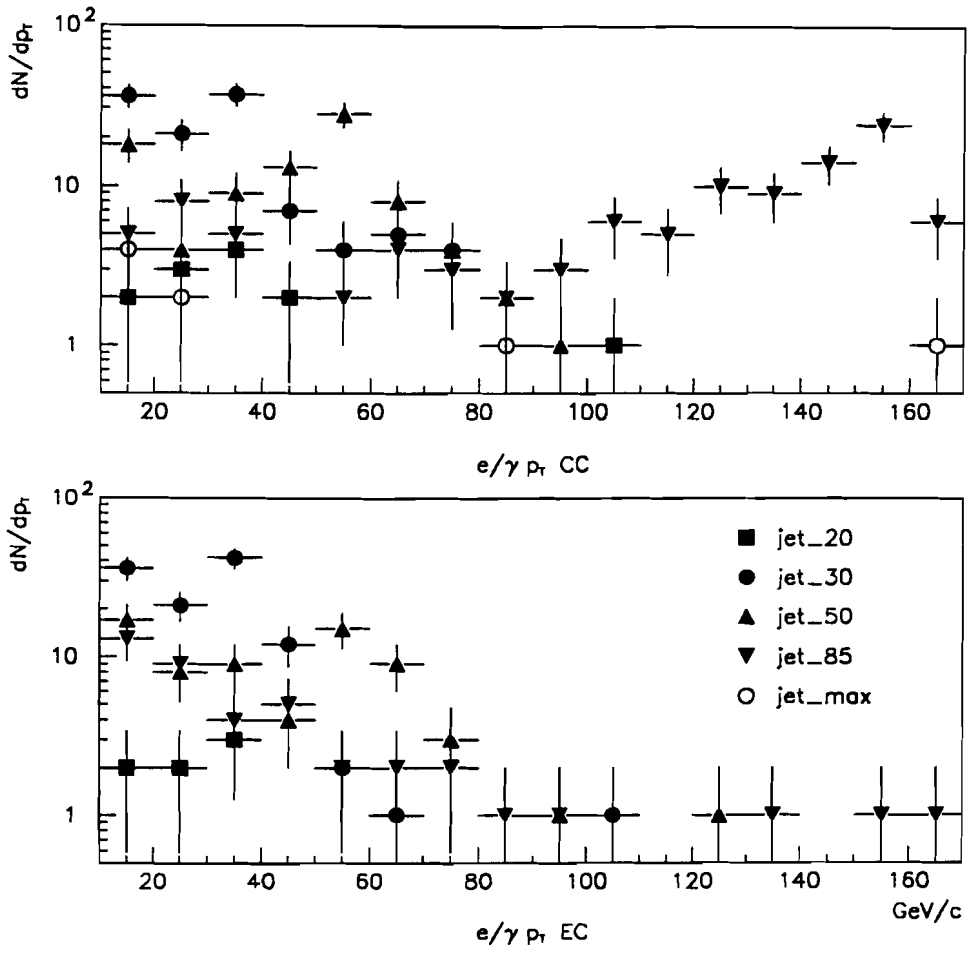

Figure B.3: Transverse energy distribution of electrons and photons in the multijet sample for the central (CC) region and forward (EC) regions for the various filters used in this study.

In run 1A, it was determined [87] that the fraction of an inclusive isolated photon sample due to π^0 or η meson production could be parameterized by the

function

$$f_{\pi\gamma} = a \times e^{-b \times E_T}$$

where a and b are constants. The meson fraction was measured by comparing the longitudinal shower profile of photon candidates to predictions from the DØGEANT detector simulation. (Single photons are less likely to deposit energy in the first layer than two photons.) The results of the analysis were:

$$a = 1.14 \pm 0.05$$

and

$$b = 0.0177 \pm 0.0021 \text{ GeV}^{-1}$$

for photons in the CC subject to slightly different cuts than are employed here. The main difference is that the direct photon candidate selection requires the transverse energy in the isolation cone to be less than 2 GeV, while the isolation requirement in this study requires that the energy in the isolation cone be less than 10% of the energy in the core cone. (The two requirements are equivalent for a 20 GeV cluster at $\eta = 0$.) It is assumed here that the above measurement of the meson fraction is a close approximation to that which would be obtained for the analysis used here. Also, since the latest DØ results [88] indicate that the meson fraction in the forward region is similar to the central region, it is assumed that the above measurement is approximately valid for EC photons as well. Finally, since the meson fraction measurement had a systematic uncertainty of 20% at $E_T = 20$ GeV [5], a

systematic uncertainty of 30% is assigned to the meson fraction for this study to include any possible extrapolation errors to the electron/photon identification cuts used in this analysis.

Jets can be misidentified as electrons if one or both of the photons from meson decay convert to an e^+e^- pair or if a soft charged hadron (from the jet or underlying event) overlaps the photon pair. As can be seen from figure B.4, the number of electrons and photons in the multijet sample is approximately equal for $E_T > 30$ GeV. Since the conversion probability in the central region is about 10% for (single) photons, it can be concluded that there are many more electrons than would be expected from γ or $\gamma\gamma$ conversions alone. Therefore, a substantial contribution to the fake electron rate must be due to charged hadron overlaps. This effect is reproduced by the ISAJET Monte Carlo [84]. Since the numbers of fake electrons and photons in the high E_T region are roughly equal, the direct photon contribution to fake electrons can be at most 10%, if all photons in the sample were due to direct photon production. This is a relatively small correction considering the size of the systematic uncertainty on the direct photon contribution itself. Therefore, no direct photon subtraction is performed on the fake electrons[3]. In any case, a conservative systematic uncertainty of 30% is assigned to the fake electron probability to account for any possible electron contamination in the multijet sample.

[3]Since loose electrons (e_l) are not subject to tracking requirements, the candidates in the multijet sample have a contribution from direct photons, and the appropriate subtraction is performed in this case.

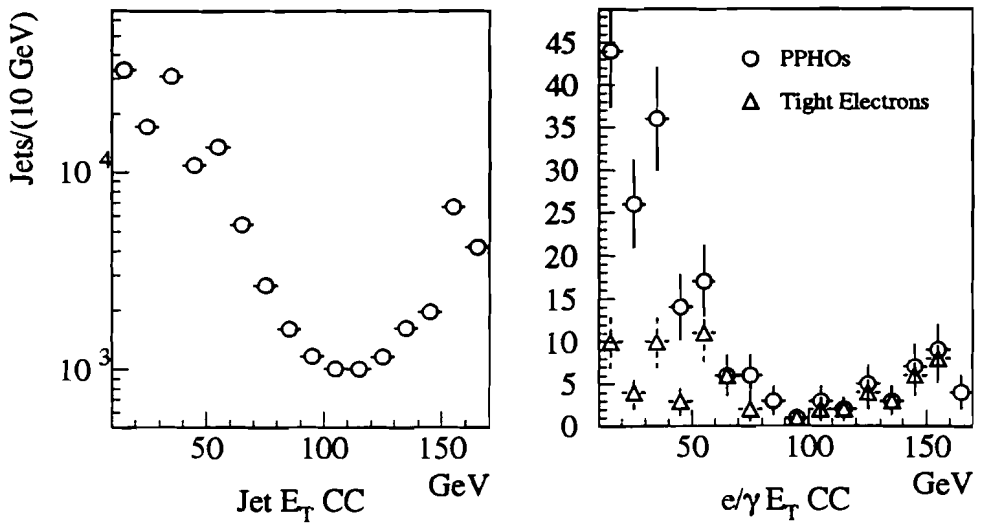

Figure B.4: Jet, electron, and photon CC candidates identified in the multijet sample.

B.5 Fake Probabilities

After the corrections of the previous section have been applied to the photon populations, equations (B.1) and (B.2) are used to calculate the fake probabilities. These are shown in figure B.5 as a function of transverse energy. The error bars displayed are Gaussian (symmetric) approximations to binomial uncertainties on the population ratios. It is evident that the probability for a jet to be misidentified as an electron increases at high E_T. A possible interpretation of this effect is that soft charged hadrons are more likely to be produced in the fragmentation process near leading π^0/η as the parent parton energy E_T increases. Conversely, the fake photon

probabilities decrease at high E_T, since the the isolated leading neutral mesons are more likely to be misidentified as electrons than at low E_T.

For each of the objects listed in table 4.1 and each corresponding plot in figure B.5, the E_T-dependent fake probability is parameterized by the linear function

$$P = a_0 + a_1 E_T$$

where a_0 and a_1 are constants determined by a fit to the data and E_T is measured in units of GeV. Table B.2 lists the fitted values of a_0 and a_1.

Object Type	CC		EC	
	$a_0 \times 10^3$	$a_1 \times 10^5$	$a_0 \times 10^3$	$a_1 \times 10^5$
e_t	-0.173 ± 0.20	1.43 ± 0.51	0.528 ± 0.86	5.09 ± 2.3
e_l	0.0754 ± 0.29	2.06 ± 0.70	1.32 ± 1.0	6.31 ± 0.27
γ	1.08 ± 0.17	-0.845 ± 0.352	0.64 ± 0.11	-

Table B.2: Jet misidentification probabilities for electrons and photons. Errors quoted are statistical (fit) errors only. A systematic uncertainty of 30% is assigned to each fake probability. Uncertainties given in this table are statistical only.

The following conclusions can be drawn regarding the jet misidentification probabilities:

- The requirement of a track or hits reduces the fake rate by about a factor of 5 for central electrons. The track requirement results in about 1/3 fewer

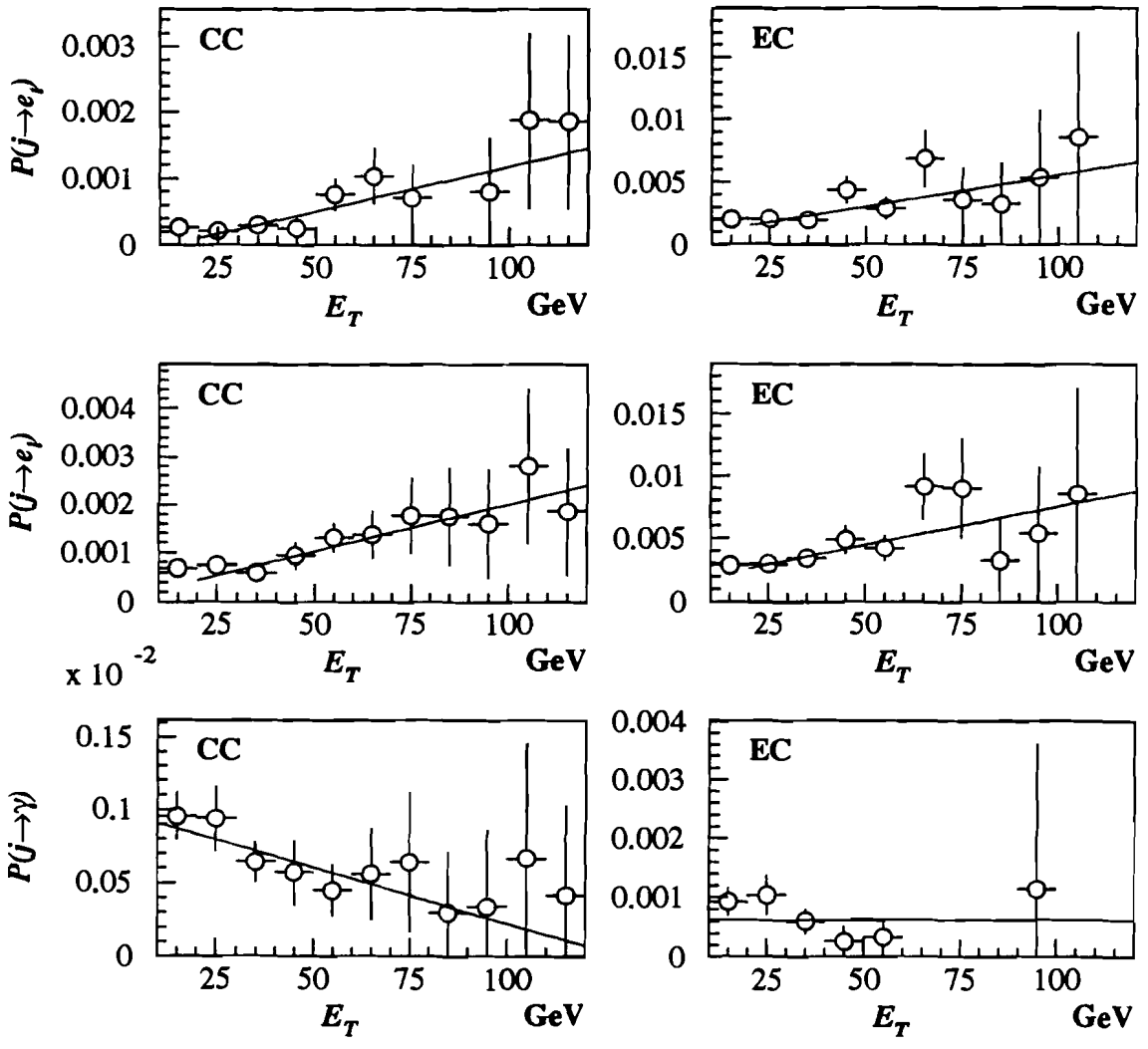

Figure B.5: Jet misidentification probabilities as a function of transverse energy for objects in the central and forward regions.

fake central electrons relative to electrons subject only to drift chamber hit requirements.

- Due to the high track density in the forward region, the electron fake rate is 5-10 times higher in the EC than in the CC. The photon fake rate for the EC is similar to that for the CC.

B.6 Background Prediction for $Z \rightarrow ee$

To investigate the validity of the above procedures, the fake electron probabilities in table B.2 can be applied to a multijet sample and compared to dielectron data. The predicted fake $e_t e_l$ spectrum from the `jet_20` data should match the background observed in $Z \rightarrow ee$ candidates collected from the `em2_eis2_hi` filter.

To make the comparison as legitimate as possible, the kinematic requirements on jets are the same as those imposed on electrons:

- $E_T > 25$ GeV
- $|\eta_{\rm det}| < 1.0$ or $1.5 < |\eta_{\rm det}| < 2.5$

It should also be noted that although `jet_20` and `em2_eis2_hi` require objects with $E_T > 20$ GeV, `em2_eis2_hi` is slightly more efficient near threshold for electrons relative to `jet_20` for jets due to the difference in electron and jet energy resolutions. Figure B.6 shows the jet E_T spectrum and the jet distribution after selection criteria have been applied. The apparent depletion of jets near $E_T = 25$ GeV is due to trigger resolution.

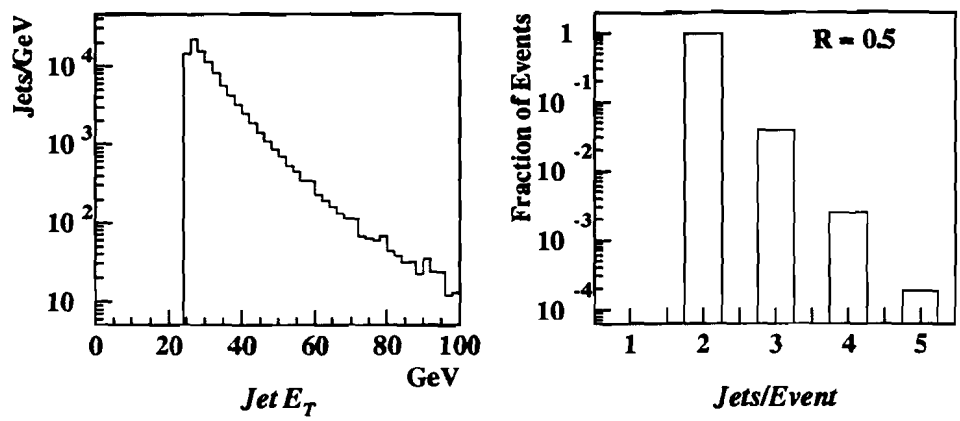

Figure B.6: Left: transverse energy distribution of jets in multijet candidate events. Right: distribution of the number of jets per event. See text for selection criteria.

The probability for a dijet pair to be misidentified as a dielectron pair is given by

$$P_{jj\to ee} = P_1 P_2$$

where P_1 and P_2 are the individual fake probabilities for each of the two jets. In events with more than two jets, the number of possible dijet combinations, N_{jj}, is given by

$$N_{jj} = \frac{N_j!}{2!(N_j - 2)!}$$

where N_j is the number of jets in the event satisfying the desired kinematic requirements. Assuming only one dijet pair per event can result in a dielectron fake at a time, the probability for a *given pair* to result in a dielectron fake is P_{jj} multiplied

by the probability that no other pairs in the event result in a fake pair. In other words, the probability that jets i and j fake the ee signal is given by

$$P_{ij} = P_i P_j \prod_{n,m \neq i,j} (1 - P_n P_m) \tag{B.3}$$

and the probability that *any one pair* fluctuates is given by

$$P = \sum_{i,j} P_i P_j \prod_{n,m \neq i,j} (1 - P_n P_m).$$

In practice, the correction in equation (B.3) is small, as less than 5% of the multijet events contain more than two jets which satisfy the kinematic requirements outlined previously. See figure B.6 for details.

The final factor to consider is the relative luminosities of the dielectron and multijet samples. The dielectron sample[4] corresponds to 72 pb^{-1}, and the multijet sample corresponds to 6.0^{-1} nb, so the predicted number of fake dielectrons must be multiplied by 1.20×10^4 before comparing them to those in the dielectron candidate sample.

Using the fake probabilities for e_t and e_l from table B.2, the dielectron fake probability from equation B.3, and summing over all possible dijet combinations per event, the fake dielectron spectrum shown in figure B.7 is obtained. The predicted background matches the observed dielectron mass spectrum quite well. In the sidebands on either side of the $Z \rightarrow ee$ peak, the predicted background spectrum is

[4]Since drift chamber hit information is available only from μDST's reconstructed with RECO 12.15 and higher, data which was reconstructed with previous versions were not used.

lower than the observed ee spectrum, but the ee spectrum is expected to contain Drell-Yan pairs and $Z \to \tau\tau \to eeX$ in addition to misidentified jets. These signals were estimated using 4-vectors from the PYTHIA generator [77] and the parametric detector simulation of chapter 7. These predictions are shown in figure B.7 for the sideband regions. The predicted number of total signal plus background events is greater than the observed data in the lower sideband, but both agree to within the $\sqrt{2} \times 30\%$ systematic uncertainty assigned to the dielectron fake rate. Similar behavior is observed in the 130-150 GeV bin, and the data exceed the prediction slightly in the 110-120 GeV bin.

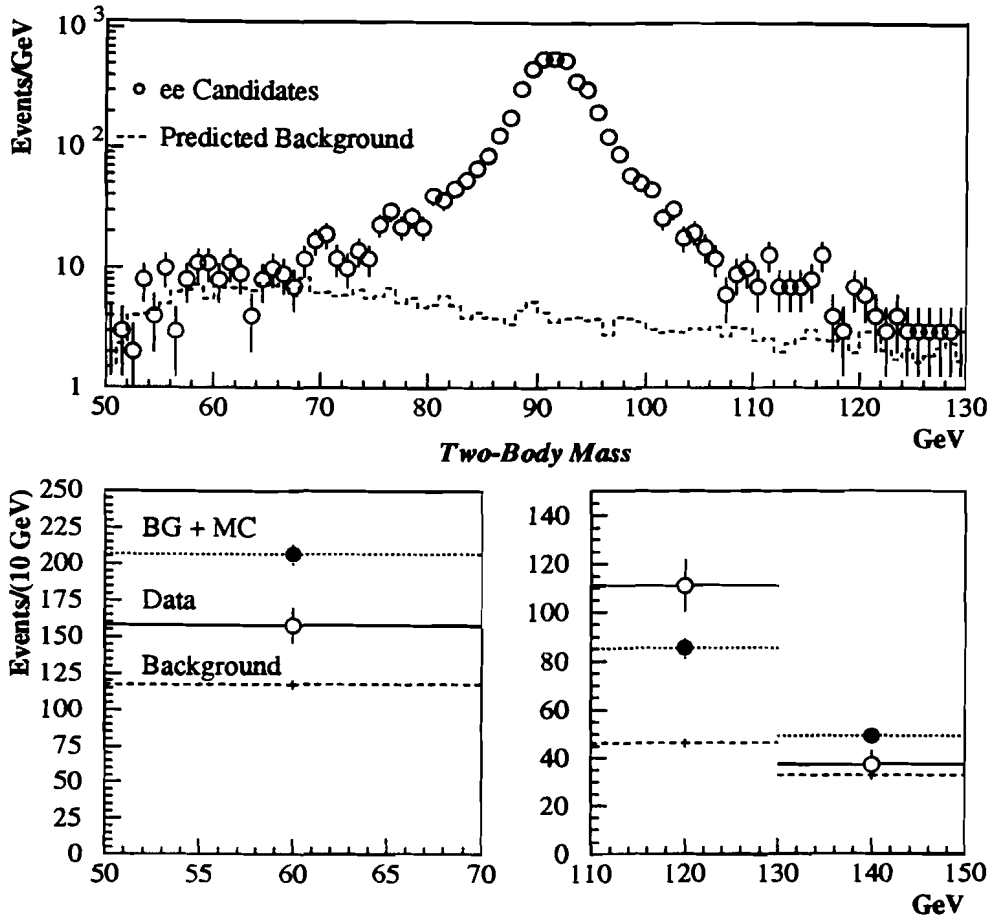

Figure B.7: Top: Invariant mass of dielectron candidates and predicted multijet background. Bottom: Invariant mass spectrum of dielectron candidates and predicted multijet background for the sidebands on either side of the $Z \rightarrow ee$ peak. Also indicated are the number of expected events based on the PYTHIA Monte Carlo generator. Error bars are statistical only.

Appendix C

Combined Likelihood Functions

When combining results from more than one channel, it is important to account for correlations in the uncertainties between the channels. For the case of the $ee\gamma$ and $\mu\mu\gamma$ measurements, there are both common and channel-specific normalization uncertainties for both background and signal predictions. Construction of the appropriate likelihood function is facilitated by the introduction of a set of normalization parameters $\{x_i\}$. The probability density describing each of the $\{x_i\}$ is assumed to be described by a normalized Gaussian $g_i(x_i, \sigma_i)$ centered at unity:

$$g_i(x_i, \sigma_i) = \frac{\exp[(x_i - 1)^2/2\sigma_i^2]}{\int_0^\infty \exp[(x_i - 1)^2/2\sigma_i^2] dx_i} \tag{C.1}$$

where the unphysical region $x_i < 0$ has been excluded. The mean number of expected events in the $ee\gamma$ channel is

$$\mu_{ee\gamma} = x_{s,c} x_{s,ee\gamma} \mathcal{L} \epsilon \sigma_{ee\gamma} + x_{b,c} x_{b,ee\gamma} B_{ee\gamma} \tag{C.2}$$

where $x_{s,c}$ represents the common signal prediction normalization, $x_{s,ee\gamma}$ is the channel-specific signal prediction normalization, $x_{b,c}$ is the common background normalization, and $x_{b,ee\gamma}$ is the channel-specific background normalization. (By construction, the central value of all $\{x_i\}$ is one.) The mean expected number of $\mu\mu\gamma$ events is given by

$$\mu_{\mu\mu\gamma} = x_{s,c} x_{s,\mu\mu\gamma} \mathcal{L} \epsilon \sigma_{\mu\mu\gamma} + x_{b,c} x_{b,\mu\mu\gamma} B_{\mu\mu\gamma} \tag{C.3}$$

where the notation is similar to that used in equation C.2. Thus, the likelihood function for the ensemble of candidate events is given by

$$\begin{aligned} L \;=\; & \int g_{s,c}\, g_{b,c}\, g_{s,ee\gamma}\, g_{b,ee\gamma}\, g_{s,\mu\mu\gamma}\, g_{b,\mu\mu\gamma} \\ & \times \left(\frac{e^{-\mu_{ee\gamma}} \mu_{ee\gamma}^{n_{ee\gamma}}}{n_{ee\gamma}!} \right) \left(\frac{e^{-\mu_{\mu\mu\gamma}} \mu_{\mu\mu\gamma}^{n_{\mu\mu\gamma}}}{n_{\mu\mu\gamma}!} \right) \\ & \times \prod_{i=1}^{n_{ee\gamma}} \frac{1}{\mu_{ee\gamma}} \frac{d\mu_{ee\gamma}}{dp_T}\Big|_{p_T^i} \times \prod_{i=1}^{n_{\mu\mu\gamma}} \frac{1}{\mu_{\mu\mu\gamma}} \frac{d\mu_{\mu\mu\gamma}}{dp_T}\Big|_{p_T^i} \\ & \times dx_{s,c}\, dx_{b,c}\, dx_{s,ee\gamma}\, dx_{b,ee\gamma}\, dx_{s,\mu\mu\gamma}\, dx_{b,\mu\mu\gamma} \end{aligned} \tag{C.4}$$

where $n_{ee\gamma}$ is the number of $ee\gamma$ candidates, $n_{\mu\mu\gamma}$ is the number of $\mu\mu\gamma$ candidates, and $\mu_{ee\gamma}$ and $\mu_{\mu\mu\gamma}$ are given by equations C.2 and C.3, respectively.

The sources of common predicted signal normalization uncertainty are those listed in table 7.2 except for the 1.2% $ee\gamma$ selection efficiency uncertainty. Thus, the common signal uncertainty $\sigma_{s,c}$ approximately 10%. The $ee\gamma$-specific signal normalization uncertainty $\sigma_{s,ee\gamma}$ is given approximately by the selection efficiency uncertainty of 1.2%.

Both the $ee\gamma$ and $\mu\mu\gamma$ background estimates are based on the jet misidentification probabilities for photons, which has a 30% normalization uncertainty. Therefore $\sigma_{c,b} = 0.30$. Generally, the background estimates are based on data taken with triggers which are different from those used for the signal, so there are (relative) trigger normalization uncertainties which must be included as $\sigma_{ee\gamma}$ and $\sigma_{\mu\mu\gamma}$. In the case of $ee\gamma$, the relative normalization of the background obtained from single electron filters to that obtained from `em2_eis2_hi` had an uncertainty of about 5%, but only about one third of the total background was from the $e_t j\gamma$ and $e_l^* j\gamma$ sources (which required use of this normalization), so $\sigma_{ee\gamma} \approx 1.7\%$. These uncertainties are summarized in table C.1 for convenience.

Once the muon-specific normalization uncertainties $\sigma_{s,\mu\mu\gamma}$ and $\sigma_{b,\mu\mu\gamma}$ have been estimated and the candidates identified, equation C.4 can be used to calculate the likelihood as a function of couplings. Confidence regions for the couplings can then be obtained from the likelihood by the methods of section 9.3.

$\sigma_{s,c} = 0.10$
$\sigma_{b,c} = 0.30$
$\sigma_{s,ee\gamma} = 0.012$
$\sigma_{b,ee\gamma} = 0.017$
$\sigma_{s,\mu\mu\gamma} = ?$
$\sigma_{b,\mu\mu\gamma} = ?$

Table C.1: Summary of uncertainties for combined likelihood construction.

Bibliography

[1] E. Commins and P. Bucksbaum, *Weak Interactions of Leptons and Quarks.* Cambridge University Press, (1983).

[2] C.N. Yang and R.L. Mills, "Conservation of Isotopic Spin and Isotopic Gauge Invariance." *Physical Review* **96**, 191, (1954).

[3] Glashow, S.L., "Partial Symmetries of Weak Interactions." *Nuclear Physics* **22**, 579, (1961).

[4] Weinberg, S., "A Theory of Leptons." *Physical Review Letters* **19**, 1264, (1967).

[5] Salam, A., *Proceedings of the Eighth Nobel Symposium,* ed. by N. Svartholm, Almqvist & Wiskell, Stockholm, (1968).

[6] Higgs, P. W., "Broken Symmetries, Massless Particles, and Gauge Theories." *Physics Letters* **12**, 132, (1964).

[7] 't Hooft, G. "Renormalization of Massless Yang Mills Fields." *Nuclear Physics* **B33**, 173, (1971).

[8] UA1 Collaboration, "Experimental Observation of Isolated Large Transverse Energy Electrons with Associated Missing Energy at $\sqrt{s} = 540$ GeV." *Physics Letters* **122B**, 103, (1983).

[9] UA2 Collaboration, "Observation of Single Isolated Electrons of High Transverse Momentum in Events with Missing Transverse Energy at the CERN $\bar{p}p$ Collider." *Physics Letters* **122B**, 476, (1983).

[10] UA1 Collaboration, "Experimental Observation of Lepton Pairs of Invariant Mass around 95 GeV/c^2." *Physics Letters* **126B**, 398, (1983).

[11] UA2 Collaboration, "Evidence for $Z^0 \rightarrow e^+e^-$ at the CERN $\bar{p}p$ Collider." *Physics Letters* **129B**, 130, (1983).

[12] V. Barger and R. Phillips, *Collider Physics*. Frontiers In Physics Lecture Note Series, Addison-Wesley, (1987).

[13] S. Abachi, *et al.* (DØ Collaboration), "Observation of the Top Quark.", *Physical Review Letters* **74**, 2632, (1995).

[14] F. Abe, *et al.* (CDF Collaboration), "Observation of the Top Quark in $p\bar{p}$ Collisions.", *Physical Review Letters* **74**, 2626, (1995).

[15] Schaile, D., "Precision Data from LEP." *Proceedings of the International Conference on Vector Boson Self-Interactions*, ed. by U. Baur, *et al.*, American Institute of Physics, (1995).

[16] A. Martin, W. Stirling, and R. Roberts, "New Information on Parton Distributions." *Physical Review* **D47**, 867, (1993).

[17] A. Martin, W. Stirling, and R. Roberts, "Parton Distributions Updated." *Physics Letters* **B306**, 145, (1993).

[18] F. Paige and S. Protopopescu, *ISAJET: A Monte Carlo Event Generator for pp and $p\bar{p}$ Reactions.* Fermilab program library.

[19] Yang, C.N., "Selection Rules for Dematerialization of a Particle into Two Photons." *Physical Review* **77**, 242, (1950).

[20] Perl, M., *High Energy Hadron Physics.* Wiley and Sons, (1974).

[21] Renard, F., "Tests of Neutral Gauge Boson Self-Couplings with $e^+e^- \to \gamma Z$." *Nuclear Physics* **B196**, 93, (1982).

[22] K. Hagiwara, R. Peccei, and D. Zeppenfeld, "Probing the Weak Boson Sector in $e^+e^- \to W^+W^-$." *Nuclear Physics* **B282**, 253, (1987).

[23] U. Baur and E. Berger, "Probing the Weak-Boson Sector in $Z\gamma$ Production at Hadron Colliders." *Physical Review* **D47**, 4889, (1993).

[24] U. Baur and D. Zeppenfeld, "Unitarity Constraints on the Electroweak Three Vector Boson Vertices." *Physics Letters* **B201**, 383, (1988).

[25] Ohnemus, J., "Hadronic $Z\gamma$ Production with QCD Corrections and Leptonic Decays." *Physical Review* **D51**, 1068, (1995).

[26] H. Harari and N. Seiberg, "A Dynamical Theory for the Rishon Model.", *Physics Letters* **B98**, 269, (1981).

[27] H. Harari and N. Seiberg, "The Rishon Model." *Nuclear Physics* **B204**, 141, (1982).

[28] O. Greenberg and J. Sucher, "A Quantum Structuredynamic Model of Quarks, Leptons, Weak Vector Bosons, and Higgs Mesons." *Physics Letters* **B99**, 339, (1981).

[29] H. Fritzsch and G. Mandelbaum, "Weak Interactions as Manifestations of the Substructure of Leptons and Quarks." *Physics Letters* **B102**, 319, (1981).

[30] H. Fritzsch and G. Mandelbaum, "The Substructure of the Weak Bosons and the Weak Mixing Angle." *Physics Letters* **B109**, 224, (1982).

[31] D. Grosser, P. Falkensteiner, and F. Schoberl, "Exited States of the Weak Z boson in a Non-Relativistic Preon Model." *Physics Letters* **B153**, 179, (1985).

[32] D. Chang, W.Y. Keung, and P. Pal, "*CP* Violation in the Cubic Couplings of Neutral Gauge Bosons" *Physical Review* **D51**, 1326, (1995).

[33] G. Gounaris, R. Kogerler, and S. Schildknecht, "On $Z^0 \rightarrow e^+e^-\gamma$ Decays." *Physics Letters* **B137**, 261, (1984).

[34] Renard, F. M., "Interpretations of $Z \rightarrow ee\gamma$ Events and Additional Tests." *Physics Letters* **B139**, 449, (1984).

[35] Tomozawa, Y. "Anomalous Radiative Z^0 Decay." *Physics Letters* **B139**, 449, (1984).

[36] N. Cabbibo, L. Maiani, and Y. Srivastava, "Anomalous Z Decays: Exited Leptons?" *Physics Letters* **B139**, 459, (1984).

[37] V. Barger, H. Baer, and K. Hagiwara, "Testing Models for Anomalous Radiative Decays of the Z Boson." *Physical Review* **D30**, 1513, (1984).

[38] P. Abreu, *et al.* (DELPHI Collaboration), "Study of Radiative Leptonic Events with Hard Photons and Search for Exited Charged Leptons at $\sqrt{s} = 130$ GeV - 136 GeV." CERN-PPE-96-060, Submitted to *Phys. Lett. B*, (1996).

[39] P. Abreu, *et al.* (DELPHI Collaboration), "Search for Anomalous Production of Single Photons at $\sqrt{s} = 130$ GeV - 136 GeV." CERN-PPE-96-061, Submitted to *Phys. Lett. B*, (1996).

[40] Ryder, L., *Quantum Field Theory.* Cambridge Press, (1985).

[41] Ulrich Baur, private communication, (1996).

[42] A. Barroso *et al.*, "Electromagnetic Properties of the Z Boson." *Z. Phys.* **C28**, 149, (1985).

[43] Particle Data Group "Review of Particle Properties." *Physical Review* **D54**, (1996).

[44] C. Burgess and D. London, "Anomalous Gauge Boson Couplings and Loop Calculations." *Physical Review Letters* **D69**, 3428, (1992)

[45] C. Burgess and D. London, "Uses and Abuses of Effective Lagrangians." *Physical Review* **D48**, 4337, (1993)

[46] C. Burgess *et al.*, "Bounding Anomalous Gauge Boson Couplings." *Physical Review* **D50**, 7011, (1994)

[47] F. Boudjema *et al.*, "Anomalous Moments of Quarks and Leptons from Non-standard $WW\gamma$ Couplings." *Physical Review* **D43**, 2223, (1991)

[48] W. Marciano and A. Queijeiro, "Bound on the W-boson Electric Dipole Moment." *Physical Review* **D33**, 3449, (1986)

[49] J. Bailey *et al.*, "Final Report on the CERN Muon Storage Ring Including the Anomalous Magnetic Moment and the Electric Dipole Moment of the Muon, and a Direct Test of Relativistic Time Dilation." *Nuclear Physics* **B150**, 1, (1979)

[50] P. Méry *et al.*, "Constraints on Non-Standard Effects from Present and Future $g_\mu - 2$ Measurements." *Zeitschrift für Physik* **C46**, 229, (1990).

[51] K. F. Smith *et al.*, "A Search for the Electric Dipole Moment of the Neutron." *Physics Letters* **B234**, 191, (1990)

[52] P. Acciarri, *et al.* (L3 Collaboration), "Measurement of Energetic Single-Photon Production at LEP." *Physics Letters*, **B346**, (1995).

[53] S. Abachi, *et al.* (DØ Collaboration), "Limits on the Anomalous $ZZ\gamma$ and $Z\gamma\gamma$ Couplings in $p\bar{p}$ Collisions at $\sqrt{s} = 1.8$ TeV.", *Physical Review Letters* **75**, 1028, (1995).

[54] Landsberg, G., "Test of the Standard Model of Electroweak Interactions by Measuring the Anomalous $ZZ\gamma$ and $Z\gamma\gamma$ Couplings." Ph.D. thesis, (unpublished), 1995

[55] F. Abe, *et al.* (CDF Collaboration), "Limits on Z-photon Couplings from $p - \bar{p}$ Interactions at $\sqrt{s} = 1.8$ TeV.", *Physical Review Letters* **74**, 1941, (1995).

[56] Thompson, J., "Introduction to Colliding Beams at Fermilab." DØ Note 2367, FERMILAB-TM-1909, (1994).

[57] R. Avery, *et al.*, "Performance of the Forward Drift Chambers for the DØ Detector." DØ Note 1567 (Unpublished).

[58] J. Bantly, *et al.*, "The Level Ø Trigger for the DØ Detector." DØ Note 1996, Submitted tIEEE Trans. Nuclear Science, (1993).

[59] J. Bantly, *et al.*, "Improvement to the DØ Luminosity Constant." DØ Note 2544 (Unpublished).

[60] M. Abolins, *et al.*, "The Fast Trigger for the DØ Experiment." *Nuclear Instruments and Methods* **A289**, 543, (1990).

[61] J. Bantly, *et al.*, "The DØ Level 1.5 Calorimeter Trigger." DØ Note 2147 (Unpublished).

[62] Fatyga, M. "Tuning Electron Id Parameters for the Level 2 Trigger Using Testbeam Data." DØ Note 1768 (Unpublished).

[63] Snyder, S. "The DØ Detector." DØ Note 2500 (Unpublished).

[64] Fernow, R., *Introduction to Experimental Particle Physics.* Cambrige Press, (1986).

[65] S. Abachi, *et al.* (DØ Collaboration), "The DØ Detector." *Nuclear Instruments and Methods* **A388**, 185, (1993).

[66] Astur, R., "A Study of Fake Jets in the D0 Detector." DØ Note 1662 (Unpublished).

[67] S. Glenn and A. Goldschmidt, "Corrections to Biases in Cluster-Track Matching." DØ Note 2419 (Unpublished).

[68] Narain, M., "Electron Identification in the DØ Detector." In the proceeedings of DPF92, ed. by C. Albright *et al.*, 1678, World Scientific (1992).

[69] T. Yasuda, *et al.*, "Muon Chamber Alignment" DØ Note 2279 (Unpublished).

[70] Landsberg, G., Private Communication, (1996).

[71] M. Narain and U. Heinz, "A Study of Electron ID Efficiencies using $Z \rightarrow ee$ Decays." DØ Note 1814 (Unpublished).

[72] Grudberg, P., "Cross Section Measurements of W and Z Bosons to Electrons at D0: Event Selection and Efficiency Studies." DØ Note 2316 (Unpublished).

[73] Tartaglia, M., "Electroweak Trigger Studies." DØ Note 1333 (Unpublished).

[74] Glenn, S., "A Parametric Detector Simulation for Dibosons." DØ Note 2846 (Unpublished).

[75] Ladinsky, G. and Yuan, C.P., "The Nonperturbative Regime in QCD Resummation for Gauge Boson Production at Hadron Colliders." *Physical Review* **D50**, 4239, (1994)

[76] J. Bantly *et al.*, "Improvement to the DØ Luminosity Constant." DØ Note 2544 (Unpublished).

[77] Sjostrand, T., "PYTHIA 5.7 and JETSET 7.4: Physics and Manual." *Comput. Phys. Commun* **82**, 74, (1994).

[78] B. Choudhary, S. Glenn, and S. Mani, "Anomalous Events in $Z\gamma$ Production at DØ." DØ Note 2339 (Unpublished).

[79] W. Press *et al.*, *Numerical Recipes in C.* Cambrige Press, (1992).

[80] Glenn, S., "Limits on Anomalous $Z\gamma$ Couplings." DØ Note 2898 (Unpublished).

[81] Barlow, R., *Statistics: A Guide to the Use of Statistical Methods in the Physical Sciences.* Wiley & Sons, 1989.

[82] James, F., *MINUIT Reference Manual.* CERN program Library Long Writeup D506, Version 92.1, 1992.

[83] D. Chakrobarty and M. Fatyga. "QCD Backgrounds to Electroweak Signals: A Study of Electron and Fake Photon Probability" DØ Note 1753, (unpublished)

[84] M. Fatyga, "A Comparison of Fake Electron Rates in Data and the ISAJET Monte Carlo. A Comparison of Multi-Jet Triggers with ISAJET Monte Carlo". DØ Note 1850, (unpublished)

[85] M. Kelly, "Jet Faking Photon/Electron Study". DØ Note 1659, (unpublished)

[86] M. Kelly, "The Doomsday Study of QCD Flakes for $W\gamma$ in RECO 11". DØ Note 2215, (unpublished)

[87] S. Fahey, "Direct Photon Production at $\sqrt{s} = 1.8$ TeV". Ph.D. thesis, (unpublished), 1995

[88] S. Abachi *et al.*, "The Isolated Photon Cross Section in the Central and Forward Rapidity Regions in $p\bar{p}$ Collisions at $\sqrt{s} = 1.8$ TeV", FERMILAB-PUB-96-072-E, 1996